
FORSCHUNGSCAMPUS MITTELHESSEN

Finding the Comfort Zone: Bacteria-Surface Interaction in Microbial Fuel Cells

Dissertation

Zur

Erlangung des akademischen Grades der Doktorin der
Ingenieurwissenschaften (Dr.-Ing.)

Dem Promotionszentrum für Ingenieurwissenschaften
am Forschungscampus Mittelhessen

vorgelegt von
Hanna Marianne Frühauf-Wyllie
M.Sc.

Aus Darmstadt

Gießen, 24. September 2022

Begutachtung durch:

Prof. Dr. Kai Thormann und Prof. Dr. Dirk Holtmann

Declaration of Authorship

I declare that I have completed this dissertation single-handedly without the unauthorized help of a second party and only with the assistance acknowledged therein. I have appropriately acknowledged and cited all text passages that are derived verbatim from or are based on the content of published work of others, and all information relating to verbal communications. I consent to the use of an anti-plagiarism software to check my thesis. I have abided by the principles of good scientific conduct laid down in the regulations of the leading University which were delivered to me in carrying out the investigations described in the dissertation.

Signed:

Date:

“Do not pity the dead, Harry. Pity the living, and, above all, those who live without love.”

Albus Dumbledore

JUSTUS-LIEBIG UNIVERSITÄT GIESSEN

Abstract

Promotionszentrum für Ingenieurwissenschaften
Forschungscampus Mittelhessen

Dr. Ing.

Finding the Comfort Zone: Bacteria-Surface Interaction in Microbial Fuel Cells

by Hanna Marianne FRÜHAUF-WYLLIE

In microbial fuel cells (MFC) (biological) waste can be converted to electrical power and thus contribute to the development of a sustainable circular economy. The core of any MFC are exoelectric bacteria that oxidise organic substrates and transfer resulting electrons to an electrode as terminal electron acceptor. Exoelectric bacteria that rely on direct electron transfer require immediate contact with the electrode, which gives the physico-chemical properties of the electrode surface particular importance. This is the case for the MFC model organism *Geobacter sulfurreducens* that was used in this work. The aim was to improve bacteria-surface interaction by adapting the electrode surface characteristics in order to increase MFC efficiency. The bacterial adhesion to a surface depends on a variety of physico-chemical factors; the one in focus for this work was surface charge. Layer-by-layer coating with differently charged polyelectrolytes was used to modify the surface charge of MFC anodes. Subsequently, the effect on selected MFC performance indicators was assessed. MFC with indium tin oxide (ITO) anodes (polarisation +0.1 V vs. Standard Hydrogen Electrode) were used to define reference values against which the results on coated anodes could be compared. Anode surface charge influenced all analysed performance indicators and the results were subject to a general correlation: The thicker and more viable the biofilm, the higher were current density and coulombic efficiency, and the shorter was the start-up phase. However, none of the coatings significantly improved the performance compared to the non-coated electrodes (maximum current density on ITO: $399 \mu\text{A cm}^{-2} \pm 24\%$ ($n = 3$), maximum current density with negatively charged polystyrene sulfonate as terminating layer: 456 and $377 \mu\text{A cm}^{-2}$, respectively). The other coatings resulted in poorer performance. This contradicted the hypothesis accepted in literature that a positive surface charge is generally beneficial for bacterial adhesion. To gain a better understanding of the initial phase of biofilm formation, an electrochemical flow cell that can be operated under a confocal laser scanning microscope was used. The initially desired application of the flow cell (*in vivo* biofilm analysis) failed due to a fluorescent *G. sulfurreducens* strain that a) did not form a *G. sulfurreducens*-typical biofilm and b) did not develop sufficient fluorescence for microscopic analysis under anaerobic conditions. However, the results emphasised that the optimisation of MFC is difficult due to the high number of factors that influence the performance. The interaction between electrode surface coating, pH and salinity of the medium and any surface-active macromolecules released by bacteria will add on to the sole effect of the surface modification and complicates the isolated analysis of influencing factors. Also, the comparison to existing MFC improvements through surface modification is made difficult by the multivariate system the MFC is. Nevertheless, monitoring of the initial bacteria-surface interaction *in vivo* and recording the corresponding current response is a promising strategy when aiming to improve MFC anode material and can hopefully push this promising technology another step ahead.

Deutsche Zusammenfassung

Finding the Comfort Zone: Bacteria-Surface Interaction in Microbial Fuel Cells

by Hanna Marianne FRÜHAUF-WYLLIE

In mikrobiellen Brennstoffzellen (MFC) können (biologische) Reststoffe in elektrische Energie umgewandelt werden, wodurch diese Technologie einen Beitrag zur Transformation hin zu einer nachhaltigen Kreislaufwirtschaft leisten kann. Das Kernstück sind elektroaktive Bakterien, die organische Verbindungen aus biologischen Reststoffen oxidieren und die resultierenden Elektronen auf eine Elektrode übertragen. Für Bakterien, die dabei auf direkten Kontakt mit der Elektrode angewiesen sind, spielen die physikalisch-chemischen Eigenschaften der Elektrodenoberfläche eine besondere Rolle. So z.B. für den in dieser Arbeit verwendeten MFC-Modellorganismus *Geobacter sulfurreducens*. Ein Ziel der Arbeit war es die Interaktion zwischen Bakterien und Elektrode durch eine angepasste Elektrodenoberfläche zu verbessern und damit die Effizienz der MFC zu steigern. Die Oberflächen-Adhäsion hängt dabei von zahlreichen Faktoren ab; im Vordergrund dieser Arbeit stand die Oberflächenladung als Einflussfaktor. Diese wurde mittels Layer-by-Layer Beschichtung modifiziert, und anschließend der Effekt auf ausgewählte Leistungs-Indikatoren der MFC analysiert. Referenzwerte wurden mit Indiumzinnoxid (ITO) Anoden gemessen und im Folgenden mit Layer-by-Layer-beschichteten ITO-Anoden verglichen. MFCs mit unterschiedlich geladenen Anodenoberflächen zeigten Unterschiede in allen untersuchten Leistungsindikatoren, mit folgendem generellen Zusammenhang: Je dicker und intakter der auf der Anode gebildete Biofilm war, desto höher war die produzierte maximale Stromdichte und die Coulomb-Effizienz und umso kürzer war die Startphase der Stromproduktion. Keine der Beschichtungen verbesserte allerdings die Leistung der MFC signifikant. Die maximale Stromdichte auf ITO-Elektroden war $399 \mu\text{A cm}^{-2} \pm 24\%$ ($n = 3$) und mit negativ geladenem Polystyren-Sulfonat als Abschlusschicht 456 bzw. $377 \mu\text{A cm}^{-2}$. Die weiteren Beschichtungen führten zu geringen Leistungsdaten. Dieses Ergebnis steht der grundsätzlichen Annahme in der Literatur gegenüber, dass positiv geladene Oberflächen einen positiven Einfluss auf die Adhäsion negativ geladener Bakterien haben. Um die initiale Phase der Biofilmbildung besser zu verstehen, wurde der MFC Reaktor gegen eine elektrochemische Durchflusszelle ausgetauscht. Diese ermöglicht *in vivo* Biofilm-Analytik, da sie unter einem konfokalen Laserscanning Mikroskop betrieben werden kann. Diesem Ziel standen jedoch zwei Herausforderungen gegenüber: Zum Einen bildete der eingesetzte fluoreszente *G. sulfurreducens* Stamm keinen regelmäßigen und *G. sulfurreducens*-typischen Biofilm und zum Anderen war die unter anaeroben Bedingungen entwickelte Fluoreszenz nicht ausreichend für die Bildgebung. Zusammenfassend kann festgestellt werden, dass eine zentrale Herausforderung bei der Optimierung der Leistungsdaten von MFC die hohe Anzahl an Einflussfaktoren ist. Die Interaktion der Oberflächenbeschichtung mit pH und Ionenstärke des Mediums, sowie mit sekretierten oberflächenaktiven Molekülen wird sich immer zu der eigentlich veränderten Oberflächeneigenschaft (der Ladung) addieren und erschwert die isolierte Auswertung der Einflussfaktoren. Dazu kommt, dass der Vergleich mit schon bestehenden Modifikationen, die die MFC-Leistung verbessern, durch das Fehlen eines standardisierten Reaktorsystems erschwert wird. Die Analyse der initialen Adhäsion unter *in vivo* Bedingungen (im Gegensatz zur Endpunktbestimmung) ist ein Schritt in die richtige Richtung und leistet einen Beitrag dazu MFCs als Baustein einer nachhaltigen Kreislaufwirtschaft weiterzuentwickeln.

Acknowledgements

This work is the extract of an eventful journey and would not have been possible without collaborators and great company.

Financial resources for this project were provided by the German Federal Ministry of Education and Research (under nos. 031A226) and the Arbeitsgemeinschaft industrieller Forschungsvereinigungen (AiF).

The investigation of bacteria-surface interaction requires in-depth knowledge of both the microorganisms and the surface. For the latter I had great help from other departments and benefited from the interdisciplinary collaborations at the DECHEMA Research Institute. Special thanks go to the DECHEMA workshop for constructing, repairing, re-building and brainstorming for me and with me, to Sigrid Benfer for assisting me with the HR-SKP analysis and to Mathias Röhrig for giving a helping hand with all kinds of problems.

For three years of my PhD the IBT group was my working home, and the lovely people in this group just made everything significantly more pleasant. We spent so many days with a good laugh, with helping each other, cheering each other up and rolling problems over. Thank you group for all that, thank you Sofia for being the wisest office partner and an excellent problem solver, thank you Felix for being the most empathetic office partner, for always listening, no matter how odd the stories were that I was telling you, and most importantly for being a dear friend.

This work would not have been possible without Dirk Holtmann and Markus Stöckl. I highly appreciate the free rein they gave me, the valuable advice they provided when help was needed, the fruitful discussions on paper writing and planning and their overall trust in me. Thank you Markus for your superb handling when experiments were not going their way, when electrochemistry counselling was very much needed or all different kinds of things in the lab were falling part. Thank you Dirk for your openness, your pragmatism, your positivity and above all your trust in me. I have always felt in good hands. As said, this would not have been possible without the both of you. Also, I am very thankful for the encouraging feedback on my thesis and here I also want to thank Kai Thormann for agreeing to review this work, as well as Sylvia Schnell and Harald Weigand for agreeing to be part of the examination board.

What a journey these past years have been. The devastating loss of a best friend rocked our little boat heavily and too many funerals in the past time delivered their message: life is precious and can be incredibly short. But so many marvellous things happened along the way too: We got married, we got to travel, we got to spend so many hours with our wonderful families, we see our beloved ones thriving and I feel so lucky to live this life I have. I am proud of myself, I am proud to see myself grow and there are no words to adequately say thank you for being on this journey with me: Alex, Sophi, Luisi, Mam, Paps - you mean the universe to me and I honestly think, together we are doing pretty well with this life. And to Alex - I love the love you give, the support you provide is unique and I feel incredibly blessed that the universe, fate or whatever greater force there may be, accompanies us on the path we walk.

Contents

Declaration of Authorship	iii
Abstract	vii
Deutsche Zusammenfassung	ix
Acknowledgements	xi
1 Introduction	1
1.1 Microbial fuel cells	3
1.2 Electroactive organisms	5
1.2.1 <i>G. sulfurreducens</i> electron transfer	5
1.2.2 <i>G. sulfurreducens</i> metabolism	7
1.3 Surface interaction and biofilm formation	9
1.4 Electrode materials	10
1.4.1 GAC in fluidised bed reactors	11
1.5 Electrode modifications	12
1.5.1 Layer-by-Layer coating	13
1.6 Biofilm analysis	15
1.6.1 CLSM	15
1.6.2 EIS	15
2 Objective	17
3 Material and Methods	19
3.1 Chemicals	19
3.2 Bacterial strains and conditions	19
3.3 Sampling procedure for growth experiments	20
3.4 HPLC analysis	20
3.5 The electrochemical H-cell	21
3.5.1 Reactor construction	21
3.5.2 Electrode preparation	22
3.5.3 Electrochemical cultivation of <i>G. sulfurreducens</i> in H-cells	22
3.5.4 Calculating Coulombic Efficiency	23
3.6 Biofilm analysis	23
3.6.1 Live/Dead staining	24
3.6.2 Imaging using CLSM	24
3.6.3 Measuring biofilm thickness	24
3.7 Layer-by-layer coating	30
3.7.1 Coating solutions	31
3.7.2 Coating of GAC _{mag}	31
3.7.3 Zeta sizer	31
3.7.4 Coating of planar electrodes	31

Coating with fluorescent polyelectrolytes	33
3.7.5 Height-regulated scanning Kelvin probe	34
3.8 Adhesion of bacteria to coated particles	34
3.9 The electrochemical flow cell	35
3.9.1 Reactor construction	35
3.9.2 Sterilisation procedure	37
3.9.3 MFC in flow cell setup	39
3.9.4 Flow cell characterisation with EIS	39
3.9.5 Biofilm characterisation with EIS	39
3.9.6 EIS of LbL-coated electrodes	39
3.10 Data analysis	40
4 Results and Discussion	41
4.1 Lbl-coated GAC _{mag}	41
4.2 Lbl-coated planar electrodes	43
4.2.1 Graphite electrodes	43
Buffer incubation of coated graphite electrodes	43
4.2.2 Coated ITO-electrodes	46
ITO electrodes with fluorescent polymers	48
4.2.3 EIS of coated electrodes	49
4.3 Adhesion of <i>G. sulfurreducens</i> to GAC _{mag}	52
4.4 MFC in H-cells on graphite electrodes as a benchmark	53
4.5 Optimum potential for MFC on ITO-electrodes	56
4.6 MFC with LbL-coated electrodes	63
4.7 Implementation of the electrochemical flow cell for continuous biofilm monitoring	69
4.7.1 Establishing the fluorescent strain <i>G. sulfurreducens</i> mCh	69
4.7.2 Electrochemical flow cell characterisation	72
4.7.3 MFC in flow cell with <i>G. sulfurreducens</i> mCh	74
4.8 <i>G. sulfurreducens</i> metabolite analysis	80
4.8.1 Donor/acceptor ratio 1:2.5	80
4.8.2 Donor/acceptor ratio 1:5 and acetate feed	80
4.8.3 Fumarate conversion by stationary cells	82
5 Conclusion and Outlook	85
5.1 Analytical method development	85
5.2 MFC reactor system	86
5.3 MFC performance depending on chemical surface properties	86
5.4 The bioelectrochemical flow cell and <i>G. sulfurreducens</i> mCh	87
5.5 The potential of MFC	87
A Appendix	89
A.1 Fluorescent polyelectrolytes in microplate reader	89
A.2 Correlation of parameters for MFC on ITO	92
A.3 Growth comparison <i>G. sulfurreducens</i> WT and mCh	93
A.4 WT current production in the electrochemical flow cell	94
Bibliography	95

List of Figures

1.1	BES contribution to a circular economy	2
1.2	Basic principle of MFC	4
1.3	Electron transfer pathways	6
1.4	Acetate metabolism by <i>G. sulfurreducens</i>	8
1.5	Biofilm formation scheme	9
1.6	Coating scheme LbL-coating	13
1.7	Polyelectrolytes used in LbL-coating	14
1.8	Randles equivalent circuit	16
3.1	The electrochemical H-cell	21
3.2	ROIs defined on a biofilm x-z image	25
3.3	Histogram of a biofilm x-z image	28
3.4	Electrode covered with silicone	32
3.5	Coating procedure for H-cell experiments	33
3.6	Sample in HR-SKP chamber	34
3.7	Flow cell construction plan	35
3.8	Flow cell assembled	36
3.9	Flow cell anode and cathode chamber	37
3.10	Flow cell setup without CLSM	38
4.1	Coating of GAC _{mag}	42
4.2	Graphite coated with PEI ₅ and PEI ₁ - HR-SKP heat map	44
4.3	Graphite coated with PEI ₅ and PEI ₁ - HR-SKP histogram	44
4.4	Graphite coated with (PEI-PSS) ₂ -PEI medium incubation - HR-SKP heat map	46
4.5	ITO multi-coat - HR-SKP heat map	47
4.6	CLSM images of fluorescently coated electrodes after incubation	48
4.7	EIS Lbl-coating Nyquist plot	50
4.8	EIS Lbl-coating Bode plot	51
4.9	Adhesion of <i>G. sulfurreducens</i> to GAC _{mag}	52
4.10	<i>G. sulfurreducens</i> MFC on graphite	54
4.11	MFC potential optimisation on ITO	57
4.12	Biofilms for different potentials on ITO	59
4.13	Thin biofilm for +0.05 V vs. SHE on ITO	60
4.14	SEM images of ITO and graphite surface	61
4.15	CLSM images of ITO and graphite surface	62
4.16	MFC on coated ITO	64
4.17	Biofilm PEI ₊ coated ITO - whole electrode	65
4.18	Biofilm PEI ₊ coated ITO - detail	66
4.19	Biofilms on differently coated ITO	67
4.20	Current curve and OD ₆₀₀ of <i>G. sulfurreducens</i> mCh and WT with fu- marate supplement	70
4.21	Biofilms <i>G. sulfurreducens</i> mCh and WT with fumarate supplement	70

4.22	Current curve of <i>G. sulfurreducens</i> mCh on ITO	71
4.23	Biofilm <i>G. sulfurreducens</i> mCh on ITO	72
4.24	Abiotic EIS of flow cell - Bode plot	73
4.25	Abiotic EIS of flow cell - Nyquist plot	74
4.26	Current production and R_{CT} of <i>G. sulfurreducens</i> mCh in flow cell down-under	75
4.27	Nyquist plot of <i>G. sulfurreducens</i> mCh in flow cell down-under	76
4.28	Biofilm in flow-cell in down-under mode and after turning around	77
4.29	Current production and R_{CT} of <i>G. sulfurreducens</i> mCh in flow cell with turning around	78
4.30	CLSM imaging of <i>G. sulfurreducens</i> mCh biofilms pre and post incuba- tion under air	78
4.31	Growth curve and metabolites of <i>G. sulfurreducens</i> 1:2.5	81
4.32	Growth curve and metabolites of <i>G. sulfurreducens</i> 1:5	82
4.33	Malate production by stationary cells	83
A.1	Emission scan of serial dilution of PEI-Rho	90
A.2	Emission scans of H-cell experiment with PEI/PSS-Rho	91
A.3	Growth comparison <i>G. sulfurreducens</i> WT and <i>G. sulfurreducens</i> mCh	93
A.4	WT current production in upright flow cell	94
A.5	WT current production in down-under flow cell	94

List of Tables

3.1	Technical dimensions of flow cell components.	37
4.1	Surface potential of coated and non-coated GAC _{mag} pre- and post ddH ₂ O/buffer incubation (0.125 M phosphate buffer) is shown as mean zeta potential of technical triplicates \pm SD (absolute values). For non-treated particles SD shows the error propagation of the technical triplicate and two particles sets coated in different experiments. For PEI-PSS-PEI coated particles post buffer incubation no zeta potential could be determined.	43
4.2	Surface potential of a planar graphite electrode with a non-coated section, a section coated with (PEI-PSS) ₂ -PEI and one with only PEI ₁ (in V vs. SHE). The median surface potential of the area analysed with the HR-SKP is given with the SD of surface potential in the respective area. Data from the respective areas were manually split according to the peaks in the histogram. An illustration of the data is also shown in Figure 4.2 and 4.3.	45
4.3	Surface potential of non-coated ITO and ITO coated with PSS-, CHI+, ALG- and PEI+, analysed with the HR-SKP. Data are given as median \pm SD of the respective sections marked on the electrode.	47
4.4	Mean and SD of maximum current density, start-up time, time until maximum current production was reached, biofilm thickness and η_C for MFC on graphite electrodes at +0.6 V vs. SHE applied. n = 14 for the first three parameters shown, n = 6 for biofilm thickness, n = 9 for η_C . For values marked with * n=1.	55
4.5	Max j as primary MFC performance indicator is indicated for different <i>G. sulfurreducens</i> pure culture MFC at poised potential on graphite electrodes. *For [99] n = 6 in one reactor. n = 3 for [156] (biological replicates), n = 14 in this work (biological replicates).	56
4.6	Current density, start-up time, biofilm thickness and η_C for different potentials applied in MFC on ITO electrodes. Indicated are mean values \pm SD. Potentials are given in V vs. SHE, with n = 3.	58
4.7	Maximum current density, start-up time, biofilm thickness and η_C for two experiments on each coating PSS-, CHI+, ALG- and PEI+. Mean and SD for non-coated ITO as are given as reference (n = 3).	64
4.8	Maximum current density, start-up time, time until maximum current was reached and biofilm thickness for a biological triplicate of flow cell experiments in <i>down-under</i> mode.	75
4.9	Growth parameters for two different electron donor/acceptor ratios. Values are given as mean \pm SD of a biological triplicate.	81
A.1	Pearson correlation coefficients for correlation among MFC performance indicators and applied potential. **** p < 0.0001, *** p < 0.001, ** p < 0.01, * p < 0.1	92

List of Abbreviations

AFM	A tomic F orce M icroscopy
ALG	A lginate
BES	B io E lectrochemical S ystem
CE	C ounter E lectrode
CHI	C hitosane
CLSM	C onfocal L aser S canning M icroscope
CNT	C arbon N anotubes
η_c	C oulombic efficiency
ddH₂O	d ouble d istilled H₂O
DET	D irect E lectron T ransfer
DMSO	D imethyl S ulfoxid
EAB	E lectroactive B acteria
EET	E xtracellular E lectron T ransfer
EIS	E lectrochemical I mpedance S pectroscopy
EPS	E xtracellular P olymeric S ubstances
GAC	G ranular A ctivated C arbon
HPLC	H igh P ressure L iquid C hromatography
HR-SKP	H eight R egulated S canning K elvin P robe
ITO	I ndium T in O xide
LbL	L ayer b y L ayer
MES	M icrobial E lectrosynthesis
MFC	M icrobial F uel C ell
OCP	O pen C ircuit P otential
PEEK	P oly E ther E ther K etone
PEG	P oly E thylene G lycol
PEI	P oly E thylene I mine
PEM	P roton E xchange M embrane
PI	P ropidium I odide
PP	P oly P ropylene
PSS	P oly S tylene S ulphonate
PTFE	P olytetrafluorethylen
PVDF	P olyvinylidene fluoride
QCM	Q uartz C hrystal M icrobalance
RE	R eference E lectrode
ROI	R egion o f I nterest
SD	S tandard D eviation
SEM	S canning E lectron M icroscopy
SHE	S tandard H ydrogen E lectrode
TCA	T ricarboxylic A cid
TEA	T erminal E lectron A ceptor
WE	W orking E lectrode
WT	W ild T ype
XPS	X -ray P hotoelectron S pectroscopy

*For my beloved ones. In loving memory of the ones who left
too early.*

Chapter 1

Introduction

“Energy is a prerequisite for development and sustainable energy systems are a prerequisite for sustainable development” Poul Alberg Østergaard [1]

Sustainable (economic) development is only possible when energy generation emerges from burning fossil fuels to the use of alternatives in power generation. Those are currently mainly wind [2], solar [3], tidal [4] and geothermal energy [5] and energy generated from biomass [6]. There is an additional source of energy that is abundant because modern society produces it continuously: waste.

Waste is a greatly miscellaneous matter and not all types of waste can be re-used, as in being returned to the material cycle, however its environmental impact can be reduced [7]. Different sorts of waste treatment are prioritised by the so-called “waste hierarchy”, that is in order from the preferred to the least preferred option: prevention, minimisation, re-use, recycling, energy recovery and disposal [7, 8]. Context of this work are biodegradable wastes, positively framed bio-waste resources, which sum up agricultural wastes, municipal solid wastes, sludge, waste water and food wastes [9]. All of those contain a substantial amount of organic compounds and the stored chemical energy can be converted to electrical energy by certain microorganisms. This phenomenon is covered by a set of emerging technologies called bioelectrochemical systems (BES). BES include:

- Microbial fuel cells (MFC) to produce electricity for example from wastewater streams by the interaction of bacteria with an anode [10–12]
- Microbial electrolysis cells for hydrogen formation [13]
- Microbial electrosynthesis cells (MES) for chemical synthesis on a cathode [13]
- Microbial desalination cells, which are basically MFC-driven electro dialysis cells [14]
- Microbial metal recovery cells where heavy metal cations are the electron acceptors at the cathode of an MFC [15]

Core to all systems are electroactive bacteria (EAB) that are capable of direct or indirect interaction with either an anode or a cathode. So-called exoelectrogenic bacteria are capable of transferring electrons outside the cell to insoluble electron acceptors such as metal ions or solid electrodes as required in MFC applications. *Vice versa*, electrorophic organisms can process electrons from a cathode and catalyse reduction reactions from CO₂ to organic compounds for example [16]. The microbial production of valuables solely from (preferably green) energy and CO₂ is the most attractive application for MES, as it is the one with the least ecological footprint. Value-added products from substrates present in waste(water) streams include hydrogen,

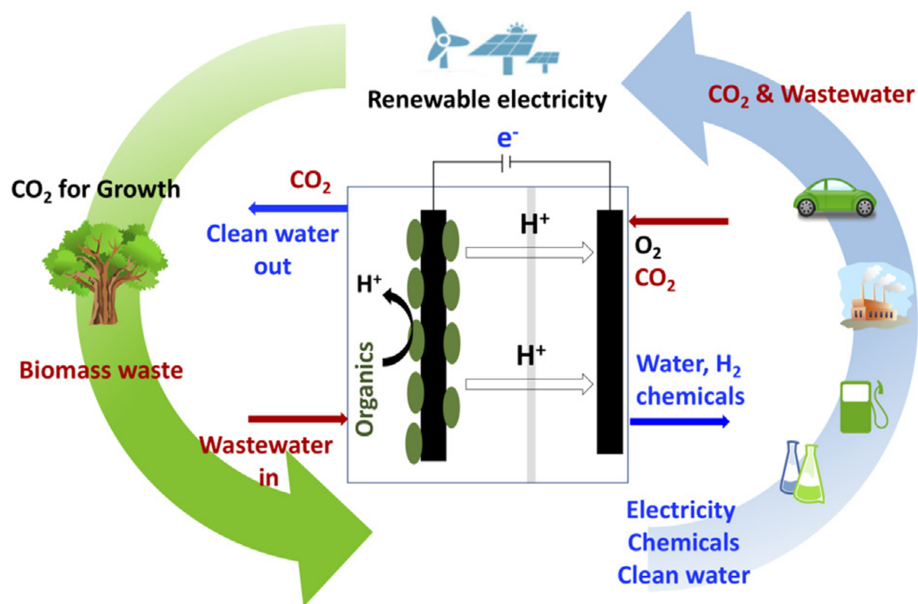


FIGURE 1.1: Jung et al. showed schematically how BES can contribute to a circular bioeconomy [18]. The principle is based on EAB that a) use renewable electricity to produce valuable chemicals from CO_2 (in green) and b) produce electricity from waste(water) streams that are an abundant industrial product (in blue).

methane, volatile fatty acids, alcohols, hydrogen peroxide and metals [17]. Major challenges in this field are reactor scale-up, post-processing of the products and optimisation of the reaction system with regards to long-term operation and optimal conditions for the microbial catalysts [17].

In contrast to MES processes that require energy input, exoelectrogenic bacteria in MFC digest biodegradable organic or inorganic matter in absence of oxygen and use the anode as electron sink which induces an electrical current. The microorganisms mostly associated to this process are *Geobacteraceae*, that form biofilms on the electrode and preferably metabolise acetate [19]. An ideal process is catalysed by a syntrophic community in which the complex substrate “waste” is broken down initially to simpler substrates that can then be used by *Geobacteraceae* for example [10]. The MFC process also benefits economically from the anaerobic metabolism of most bacteria used so that energy intensive aeration for aerobic digestion (as in traditional wastewater treatment) is no longer necessary [20]. Challenges that are associated with this young technology and are yet to be solved are discussed in the following paragraphs.

Generally, both concepts, MES and MFC, potentially contribute to a circular bioeconomy; in the chemical industry as well as in the energy sector, as illustrated in Figure 1.1 [18]. In contrast to conventional (linear) wastewater treatment, the product “waste” in a circular system is not a dead end but is re-introduced to the cycle and used for chemical or electricity production. Biomass-containing wastewater is used as influx for a BES where exoelectrogens produce electricity, protons and CO_2 by degrading organic compounds. Consecutively, electrons, protons and CO_2 can be used by electrothrophic organisms (external energy input required) to produce molecules for the chemical industry that then produces wastewater again - and the circle is closed [18].

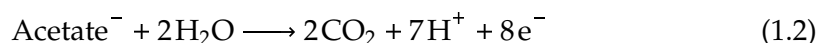
Economic assessments of MFC and MES applications were summarised by Jung et al. [18] with diverse results. For MFC evaluation the outcome depended greatly on the used wastewater stream and to what kind of traditional wastewater treatment plant the new system was compared to (e.g. larger treatment plants are more cost effective than smaller ones [21, 22]). Common performance indicators having the largest impact on the outcome of the assessments were coulombic efficiency (η_C) of the system (the ratio of electron input in the form of organic material and the electron output as in current produced), power density and chemical oxygen demand removal [18, 20, 23]. MFC fall behind traditional wastewater treatment plants especially in terms of initial investment where mainly the electrode material and the membrane (that is needed to separate the anode from the cathode reaction space) contribute to the costs [18]. Also scale-up of MFC (which can improve cost efficiency) is still limited due to increasing electrical resistance in larger reactors and stacking arrangements that often have operational limits [24].

While the outcome of economical assessments for MFC partly depends on the standards applied, the assessments for MES are more uniform. Currently product titres are low and costs for reactors high but the prognosis is promising: The immense development potential of a technology that is capable of producing high-value chemicals from waste streams at high purity and with potentially negative CO₂ balance is emphasised frequently [18, 25, 26].

Even though BES are not yet technologically ready to compete with the traditional linear way of wastewater treatment or chemical production routes, the ecological value of these sustainable technologies is beyond economical consideration and simply awaits further research. This credo was the motivation for this work to which the investigation of bacteria-electrode surface interaction in MFC was central. The following parts of the introduction focus on details of the MFC technology, *Geobacteraceae* as model organisms for MFC and anode properties.

1.1 Microbial fuel cells

An MFC consists of at least two electrodes: the anode and the cathode (schematic structure shown in Figure 1.2). Additionally, the system can be equipped with a reference electrode (RE). Anode and cathode can be separated by a membrane that generates two chambers, the anode and the cathode chamber, which contain the anolyte and the catholyte. The electric circuit is closed either by an electrical resistance or a potentiostat that allows to apply a distinct potential to provide controlled and reproducible reaction conditions. The electrolyte can be a certain type of wastewater or in more defined systems a biological buffer system with a carbon source suitable for the microorganism used (e.g. glucose, acetate etc.). Net reactions of potential metabolic routes are shown in equation 1.1 and 1.2 [27]. A comprehensive review of different substrates used in MFC was published by Pandey et al. [28]. No additional soluble electron acceptor is added to the buffer to force the anode to be used as electron sink. The reaction taking place at the cathode is primarily oxygen reduction due to its abundance and high reduction potential (equation 1.3) [29, 30]. The different ways of interaction between EAB and the anode, that are indicated by red dots in Figure 1.2, will be explained in more detail in section 1.2.



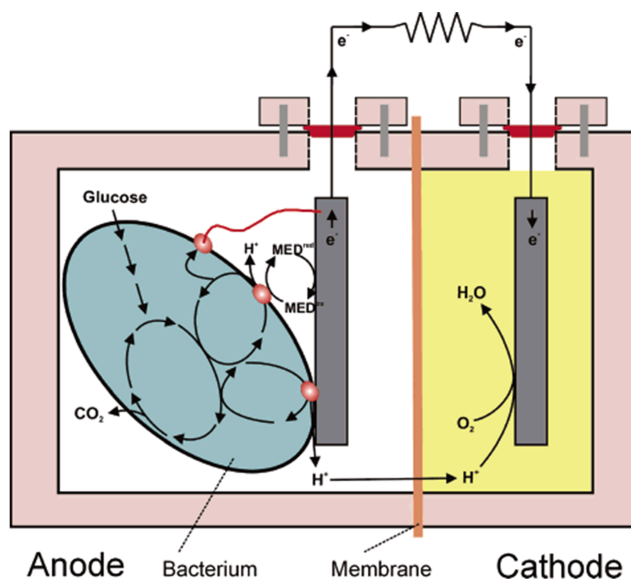


FIGURE 1.2: The basic principle of an MFC is shown (Figure from [11]). An organic substrate (e.g. glucose) is metabolised in the anode chamber and the electrons (as a product of the oxidation reaction) are transferred to the anode (either directly, via mediators or cell appendices). At the cathode a substrate is reduced, e.g. O₂ that, together with protons released in the reduction reaction at the anode, produces H₂O. The electric circuit is closed by an electrical load, either a resistor, a potentiostat or a consumer.



MFC experiments are standardised only to very little extent so far as experiments differ in the used bacteria, in electrode material and size, organic substrate (e.g. wastewater stream), anolyte, operation time and reactor design. All that makes it difficult to compare studies among each other. Still, the underlying biological principal as shown in Figure 1.2 (with glucose as exemplary electron donor) puts the experiments on a common footing.

The most common design (in lab-scale and mainly applied in this work as well) is a two-chambered H-shaped MFC in which anode and cathode chamber are separated by a proton exchange membrane (PEM), with a typical volume of 250 ml [11]. Key property to the membrane is that protons can pass to the cathode chamber but ideally not the substrate or electron acceptor (O₂) to prevent a short-circuit. The so-called H-cell is suitable for lab-scale experiments to test new electrode materials or microbial communities but usually produces low power densities due to the large distance between anode and cathode that, additionally to the membrane, contributes to the high internal resistance [11]. Other reactor geometries and scale-up possibilities were reviewed by Janicek et al. and many others [11, 24, 31]. They include single-chamber reactors (without membrane), cylindrical reactors, as well as plate and tube-shaped reactors. In tubular reactors the anodes are often cylindrical brushes or granular activated carbon (GAC). The cathode is then wrapped around the anode together with a membrane to separate the chambers [31]. An alternative are flat-plate reactors where anode and cathode are sandwiched with the separating membrane. MFC can be scaled-up to higher volumes to a certain extent but single reactors can also

be numbered-up. As many as 50 flat-plate reactors were connected in the work of Liang et al. to an overall volume of 1000 L [32]. Illustrative examples for the practical application of MFC are the work of the Ieropoulos group who established urine as an MFC substrate. The developed MFC supplied a Gameboy Colour® with power for 150 h, using stacks of 160 electrodes in an overall volume of 28 L [33, 34].

1.2 Electroactive organisms

All BES are based on the finding that certain microorganisms are able to interact with an electrode. Currently over 100 microorganisms from all three domains of life are known to perform extracellular electron transfer (EET) [16, 35]. Among those, metal-reducing *Shewanellaceae* [36] and *Geobacteraceae* [37] are the most prominent classes. Even *Escherichia coli* was used for current production after certain adoption time to the MFC environment and with specially treated electrodes [38]. If natural environments lack O₂, which is usually used as the terminal electron acceptor (TEA) by aerobically respiring microorganisms, alternative TEA come into play. When those cannot be transported into the cell, the interior redox machinery of the cell has to expand across the outer membrane which is the basis for bacteria-electrode interaction [39].

Four fundamental mechanisms how electrons can be transported from or to an insoluble TEA are described schematically in Figure 1.3 [39]. Electrons can be transferred via proteins bound to the outer membrane, called direct electron transfer (DET) [40, 41], some EAB possess cell appendices with metallic-like conductivity for long-range electron transfer [42–44], also redox conductivity via electron hopping [45] and external mediators are used for electron transfer [46]. Decisive for each pathway are macromolecular structures like multi-heme cytochrome complexes or other redox shuttles [47]. In addition to bacteria-electrode interaction, a phenomenon that has been named direct interspecies electron transfer is known that takes place between exoelectrogenic and electrotrophic organisms in mixed cultures [16].

EAB were also focus of genetic engineering approaches, with different scopes: either increase of produced currents or increase of substrate range. Current generation was for example increased by improving biofilm formation and conductivity. Gene deletion in *G. sulfurreducens* led to a more cohesive biofilm and thereby to enhanced current production [48]. Extension of substrate spectra, e.g. in engineered *S. oneidensis* strains, allowed them to metabolise xylose [49], glucose [50] or glycerol [51].

In depth analysis of all known EET pathways was beyond the scope of this work but DET as used by *G. sulfurreducens* and other *Geobacteraceae* will be explained in more detail in the next section.

1.2.1 *G. sulfurreducens* electron transfer

G. sulfurreducens PCA was used as model organism in this work due to its good biofilm formation capacity. It was first isolated from a hydrocarbon-contaminated ditch and published by Cavacco et al. in 1994 [37] and then described as “obligately anaerobic, nonfermentative, nonmotile, gram-negative rod” from the phylum of proteobacteria with a size of 2 to 3 by 0.5 µm and the capability to reduce Fe(III) with acetate or H₂ as electron donor. This makes it a respiratory metal-reducing organism. Its temperature optimum is 30 to 35 °C and it grows in up to 50 % of seawater NaCl concentration [37]. Current production with a pure culture of *G. sulfurreducens* PCA was first published in 2003 by Bond and Lovley who emphasised the high current

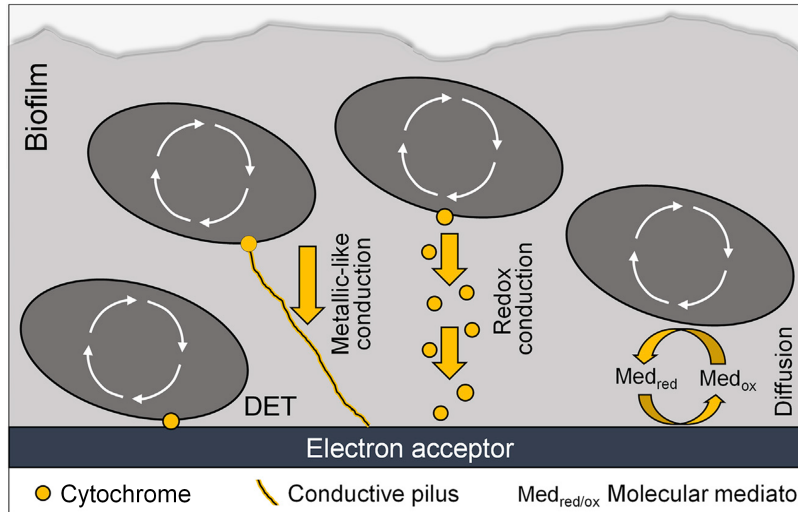


FIGURE 1.3: Four major pathways how EAB transfer electrons to an insoluble electron acceptor are shown (Figure from [39]). Electrons can either be transported directly via outer membrane-bound proteins, via electrically conductive pili, through redox conduction or by the use of external mediators.

production efficiency. The electron transfer rates were comparable to when Fe(III) served as TEA and were coupled to complete oxidation of acetate or H_2 as substrate [52].

EET mechanisms of *G. sulfurreducens* have not yet been fully resolved but many key factors have been identified already. In MFC application *G. sulfurreducens* forms up to 50 μm thick biofilms on the anode, i.e. the organism transfers electrons directly to the electrode and does not use external mediators [53]. In early works on the conductivity of *G. sulfurreducens* biofilms, type IV-pilin protein PilA was identified as important structural subunit for the reduction of insoluble electron acceptors such as Fe(III). When *pilA* was deleted in the study, the bacteria were no longer capable of attaching to or reducing insoluble Fe(III) but could still reduce soluble TEA [54]. In studies with conducting probe atomic force microscopy (AFM) of immobilised pili on a graphite surface a linear correlation between the measured current and voltage applied to the pili was detected. That led the authors to the conclusion that pili are the electrical conduction between *G. sulfurreducens* cells and insoluble TEA [54] and they coined the term *e-pili* [55].

In a consecutive study these results were extended regarding the interaction with anodes and it was stated that pili were required for high power output of thick biofilms and that low current production with thin *G. sulfurreducens* biofilms was also possible with the *pilA*-mutant [56]. Responsible for conductivity of the e-pili are most probably aromatic amino acids in the carboxyl-terminus of PilA that transfer electrons by π - π -stacking [57]. According to the authors their findings support the hypothesis that the conductive pili are necessary to interconnect layers of the biofilm so that also the outermost layers of a thick biofilm can contribute to current production [56]. This is in fact an essential feature of *G. sulfurreducens* current production: not every cell in the biofilm requires direct electrode contact in order to produce current. The nanowires (as e-pili are also called) anchor in the outer membrane and are associated with a series of outer membrane proteins, namely cytochromes and porins: OmcS,

OmcZ, OmcB, OmcE, OmcT, OmpB and OmpC [58–60]. Together they form porin-cytochrome-outer membrane-complexes to transport electrons from the quinone and quinol pool to the outer membrane and further to the TEA [61, 62]. The cytochromes are thought to accept electrons directly from the organism they are attached to as well as from neighbouring cytochromes. Thereby, a redox-gradient is generated within the biofilm with an increased portion of reduced cytochromes in further distance of the electrode. If the local concentration of oxidised cytochromes is too low, metabolic activity and biofilm growth is reduced [63]. At least two of the cytochromes (OmcS and OmcZ) have found to be co-located to the nanowires and might play a role in transferring electrons from nanowires to the TEA, however this interaction has not yet been clarified [63, 64].

A lively scientific discussion is still ongoing about the roles that especially OmcS and OmcZ play in contrast to PilA regarding electrical conductivity in *G. sulfurreducens* biofilms. The Malvankar group published a theory after which the observed nanowires are actually filaments comprised of OmcS and that the correlation of PilA and those nanowires is caused by the role of PilA in the secretion of the OmcS filaments rather than PilA composing the filaments [65]. Accordingly, electrical conductivity should be caused by the protein's hemes being stacked in 4–6 Å distance thereby allowing fast electron transport between the heme molecules [65]. They further published that in an electric field *G. sulfurreducens* cells are stimulated to produce filaments that additionally contain OmcZ embedded in stacked β -sheets in contrast to the helical structure proposed by the theory that promotes the e-pili-hypothesis [66]. Later in that sequence a study was published that opens space for both, the e-pili and the cytochrome-stack theory. When cell appendices of living cells were inspected with atomic force microscopy, two different groups were identified: One with 3 nm diameter that corresponds to the characteristics of e-pili, and the other with 4 nm diameter, corresponding to the findings of cytochrome-comprised filaments. Further, PilA was substituted with an artificial pilin-protein with no conductive properties, and cell appendix morphology was the same as observed for the wildtype, but 3-nm filament conductivity was 100-fold lower. Additionally, when the most abundant *G. sulfurreducens* outer membrane cytochromes were deleted the 4-nm filaments could no longer be observed but conductivity of the 3-nm filaments was identical to the wildtype [67]. Overall, there might be two classes of filaments responsible for the conductivity of *G. sulfurreducens* biofilms.

1.2.2 *G. sulfurreducens* metabolism

G. sulfurreducens is able to grow on acetate, H₂, lactate, formate and CO as electron donors [68–70], potential soluble electron acceptors are Fe(III)-citrate, Fe(III)-phosphate, Co(III), U(VI), S⁰, fumarate, malate [68] and to some extent also O₂ (microaerobic growth reported in [71, 72]). In this work solely the donor-acceptor-pair acetate-fumarate was used for cultivation, therefore only this metabolic pathway is discussed in the following.

Acetate is oxidised to CO₂ via the tricarboxylic acid cycle (TCA), with fumarate reduced to succinate, as seen in equation 1.4 and Figure 1.4 [73], whereby the equation only covers the dissimilated acetate. The complete oxidation of acetate releases 8 electrons, thus 4 mol of fumarate are reduced to 4 mol succinate for every mol acetate reduced. In [73] it was shown that only approximately 50% of acetate are dissimilated and the remaining is used for production of biomass. Hence, the actual donor/acceptor ratio observed is 1:2. Fumarate is entirely reduced to succinate, which

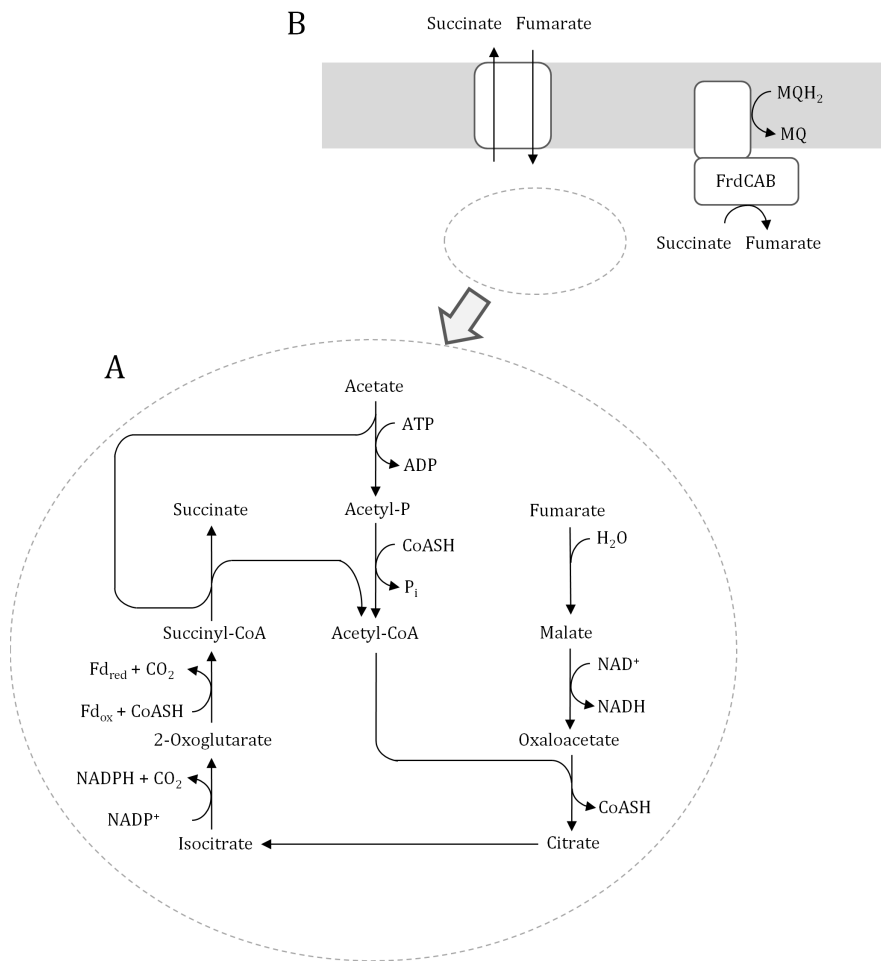
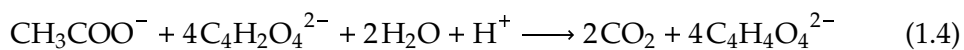


FIGURE 1.4: A: Acetate metabolism in the TCA-cycle with fumarate as electron acceptor. TCA is not closed as succinate is secreted to the medium and external fumarate continuously supplied to fuel the reaction (adapted from [73]). B: Fumarate is simultaneously reduced via the TCA and by the membrane-bound enzyme FrdCAB which is coupled to ATP synthesis via the menaquinone pool (adapted from [74]).

is secreted to the medium, so the TCA as found in *G. sulfurreducens* metabolism, is not a closed loop. Instead, the externally added fumarate is converted to oxaloacetate by fumarase and malate dehydrogenase and continuously introduced to the TCA cycle [73]. Additionally, fumarate is reduced at the membrane-bound *G. sulfurreducens* fumarate reductase FrdCAB which is coupled to the menaquinone pool and thereby to ATP-synthesis. This enzyme simultaneously acts as succinate dehydrogenase to close the TCA-cycle when not fumarate but Fe(III) is the electron acceptor [74, 75]. ATP is solely synthesised by electron transport phosphorylation, fuelled by NADH and NADPH delivered to the menaquinone pool [73].



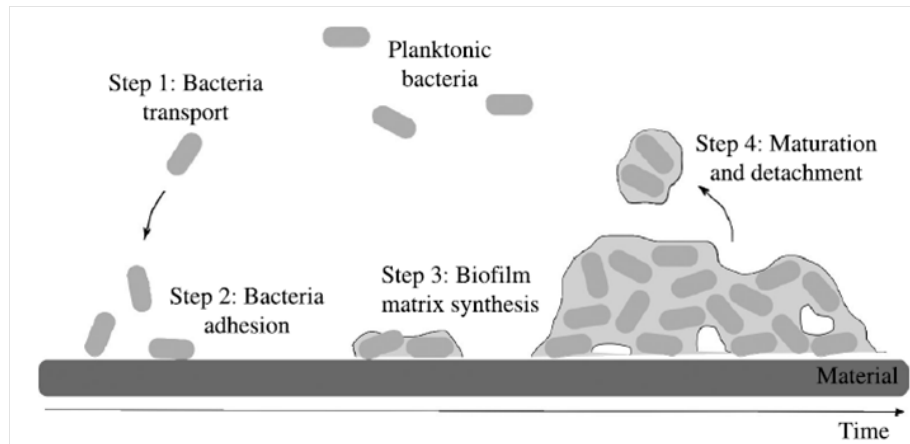


FIGURE 1.5: Biofilm formation according to the 4-step-scheme [76]. Planktonic bacteria approach the surface, single bacteria adhere, form microcolonies and start matrix production until a mature biofilm is formed.

1.3 Surface interaction and biofilm formation

Biofilms are the most ubiquitous form of bacterial life on earth. A biofilm is a complex network of bacteria and a viscous extracellular matrix that protects the cells from stressors like dehydration, toxins, variations in pH, osmolarity or temperature [76, 77]. Further, the matrix stores nutrients and hinders molecules from diffusion [76]. The close proximity of the cells in a biofilm also enhances intercellular communication via quorum sensing [78]. All these factors make a biofilm a very resilient form of life which is a problem especially in the medical field but offers many advantages in biotechnological applications [79].

Biofilm formation differs depending on the bacterial community and morphological features but a 4-step principle is common to most organisms that form biofilms (Figure 1.5) [76]:

- Bacteria transport to the surface
- Bacteria adhesion to the surface
- Bacteria proliferation and matrix synthesis
- Biofilm maturation and partial detachment

First, bacteria approach the surface driven by physical forces, such as Brownian motion, gravity or hydrodynamic forces in stirred/flow systems (for bacteria without flagella) [76, 80]. The second step is divided into a reversible and an irreversible phase of bacterial adhesion to the surface. The ability of bacteria to adhere to a surface is governed by physico-chemical properties of the surface such as electrostatic charge, hydrophobicity, wettability, surface microtopography and surface hardness [81–83]. The so-called surface sensing is also influenced by pH and ionic strength of the medium and initiates a signalling cascade that, among other effects, triggers changes in cell wall composition that promote adhesion and the secretion of a conditioning film [82, 84]. Prior to irreversible attachment, cells form that film by secreting macromolecules like lipids, polysaccharides and nucleic acids, among others. Those

macromolecules interact with and potentially mask the surface chemistry of the substrate [83].

That complex process of bacteria surface interaction is usually modelled analogous to colloid particles interacting with a surface according to the (extended) DLVO-theory [76, 85, 86]. However, this model is limited to short-period interaction with the surface since elasticity of the cells, cell appendices (pili, flagella), variations in cell wall composition (lipids, sugars) as well as external factors such as shear stress are not taken into account [87].

After initial bacteria-surface contact, the progressive removal of interfacial water allows for closer contact of cells with the surface and for short-range forces like hydrogen bonds and covalent interactions from cell wall components to come into play [76]. Cells might even rotate to use more hydrophobic surface structures to displace water and expose their most adhesive sites to the surface [84]. This promotes the transition from reversible to irreversible adhesion to the surface.

After the successful formation of a monolayer of adhered cells, proliferation starts and microcolonies spread across the surface (also known as swarming) [76]. Cells start to produce the biofilm matrix that is species-specific and consists of hydrated extracellular polymeric substances (EPS) that constitute up to 90 % of the biofilm mass [88]. The EPS is mainly composed of polysaccharides, proteins, nucleic acids and lipids that fulfil various roles within the biofilm network, among those are cellular adhesion to a surface, enzyme and cell immobilisation, mechanical stability of the biofilm, nutrition and hydration [88].

The mature biofilm is a complex community with a tertiary structure including pores and channels ensuring access to water, O₂ and nutrients [76]. Biofilm architecture can generally be divided into two types: a) irregular shape and mushroom/pillar-like structures separated by voids (mostly water channels), with low surface coverage and b) uniform and flat topology with compact layers and high surface coverage [89].

Generally, this sessile form of life is drastically different from planktonic bacterial cells; in *E. coli* biofilms almost 40 % of the genes are expressed differently compared to a planktonic culture [90]. Common characteristics can be extracted for biofilm formation and behaviour, however biofilms of various organisms are as versatile as the organisms itself and any multi-species biofilms is always more than the sum of its parts [91].

1.4 Electrode materials

For electroactive bacteria, that are capable of direct electron transfer (DET), the choice of electrode material is essential since a firm electrode-bacteria interaction is necessary for efficient current production [92]. In the following sections, electrode material properties and potential modifications are discussed.

MFC anode material should fulfil the following properties [93]:

- a) Good electrical conductivity and low internal resistance
- b) High biocompatibility
- c) Non-corrosiveness
- d) Sufficient mechanical strength

e) Cost-effectiveness

Most electrodes are either metal- or carbon-based or a combination of both. Carbon-based materials are often favoured because of their good biocompatibility, corrosion-resistance and cost-effectiveness, but a major advantage of metal electrodes is their superior electrical conductivity [94]. Gold and platinum electrodes have been frequently used in fundamental MFC research since they are electrochemically inert, but due to their high price their application in large-scale MFC is of a theoretical nature [94–96]. Other metals and the corresponding metal oxides have been successfully employed as anode material, especially stainless steel, but even copper and silver, that are originally known for their antimicrobial activity [94, 97].

Nevertheless, carbon materials are most frequently used as anodes in MFC experiments, also because of their malleability. Carbon electrodes come in all shapes and textures, from graphite rod to graphite fiber brush to carbon cloth, carbon paper, carbon felt, reticulated vitreous carbon (RVC) and lastly GAC that will be subject of the next section (also see Figure 4 of [98]). Pros and cons of the various shapes were conclusively summarised by Zhou et al., stating that all geometries aim to solve the problems that come with carbon as electrode material, that is: maximising active surface area without introducing a clogging-problem at the same time and handle the fragility of three-dimensional carbon structures [93].

In [99] Kipf et al. compared titanium and stainless steel electrodes with different carbon-based materials with respect to their usability for *G. sulfurreducens* pure culture MFC. They found that the highest current density was produced on graphite foil but with marginal differences to activated carbon cloth, stainless steel and graphite felt.

For special applications, e.g. optical or spectroscopical methods, transparent electrode materials are required. Here, mostly indium-tin oxide (ITO) or gold sputtered glass slides (e.g. in [100–102]) are used because they have good electrochemical properties and allow the observation of biofilm formation through the electrode in real-time. In this work ITO electrodes were intended to be used for *in situ* biofilm analysis in an electrochemical flow cell.

1.4.1 GAC in fluidised bed reactors

GAC is a carbon-based electrode material that aims to maximise the available electrode surface area due to the particles' highly porous structure. Thereby current production should be maximised proportionally to the available surface. GAC is a very heterogeneous material and pore size distribution highly influences interaction of bacteria with the material, as well as particle conductivity. If the pores are too small bacteria cannot adhere and too many pores decrease electrical conductivity [98]. In [103] internal resistance of the reactor could be decreased by 25 % and power output increased 6-fold by exchanging a carbon cloth anode for a packed bed of GAC. MFC with GAC as electrode material are also suitable to set up hybrid-systems of MFC and pollutant removal since GAC simultaneously filters dyes and other organic suspended solids from wastewater streams [104]. With the particulate electrode, GAC-MFC systems are predestined for stirred or fluidised operation. In [105] the authors showed that a stirred bed of GAC increased power output by 17 % compared to the packed bed, which led them to the hypothesis that the exoelectrogenic bacteria together with the GAC formed a bio-capacitor that transiently stored charge and was rapidly discharged when in contact with the current collector. The positive effect

of fluidised GAC on liquid flow patterns and substrate distribution and thereby on current generation was also verified by fluid dynamics simulation in [106].

In this work the surface properties of magnetic GAC developed by M. Stöckl in [107, 108] should be improved for a potential application in magnetic stabilisation of a fluidised bed. The magnetic particles were also used for their simplified handling since they can be separated from the supernatant by attracting particles with an external magnet. The specific surface of these particles produced from GAC and magnetite was measured as $300 \text{ m}^2 \text{ g}^{-1}$. Given the potential of GAC as anode material to improve MFC current output, the magnetic GAC (GAC_{mag}) was subject to surface modification to test whether bacterial adhesion to the particles could be enhanced.

1.5 Electrode modifications

Seen from a material's perspective, modification of the electrode is the major engineering approach to improve MFC productivity. Those approaches can roughly be clustered into following classes [92]:

- a) Increase accessible electrode surface by building 3D-electrode structures
- b) Facilitate bacterial colonisation by modifying chemical surface properties

a) includes construction of sponge or foam-like electrode structures from various, mostly carbon-based materials [109–112]. Besides, coating of electrode material with carbon nanotubes (CNT) or other nanoparticles is used to increase the electrode surface, often in combination with chemical surface modification [113–117].

For b) electrode surfaces are mostly coated with (conductive) polymers, redox-active substances, or are modified electrochemically; or treated with a combination of those. Those modifications can influence bacteria-surface interaction either on nanometer-scale, i.e. on the level of single-cell-surface interaction or on micrometer-scale, i.e. biofilm formation on a particular surface is influenced [92].

For both approaches, a) and b), it is important to choose coatings that are not only attractive for microorganisms but also electrically conductive, as well as to design 3D electrode structures that prevent surface clogging [92].

Central to this work was to alter the chemical surface properties of carbon (and ITO) anodes to improve surface colonisation. As displayed in section 1.3, bacteria-surface interaction is influenced by a plethora of factors of which electrostatic interaction was chosen to be investigated in more detail in this work. Therefore, in terms of electrode modification, the focus lay on coatings that influence electrode surface charge and at best decoupled of other factors like surface roughness, surface hardness or overall available surface area. It should be emphasised once more that this covers only a small section in the complex puzzle that bacteria-surface interaction is.

In this section some approaches (of the manifold literature there is on this topic) on surface engineering with the focus on surface charge and the conductivity of the coating shall be named.

A hypothesis that is widely accepted in literature is that positive charge at the anode surface influences electrode colonisation positively as most bacteria have a negatively charged outer surface charge so that this combination should be beneficial [92, 118]. Relevant cationic groups are mostly NH_3^+ that can be linked to the surface by different chemical or electrochemical treatments, such as the addition of nitric acid, ethylenediamine, ammonium nitrate, ammonium persulfate, polyaniline or

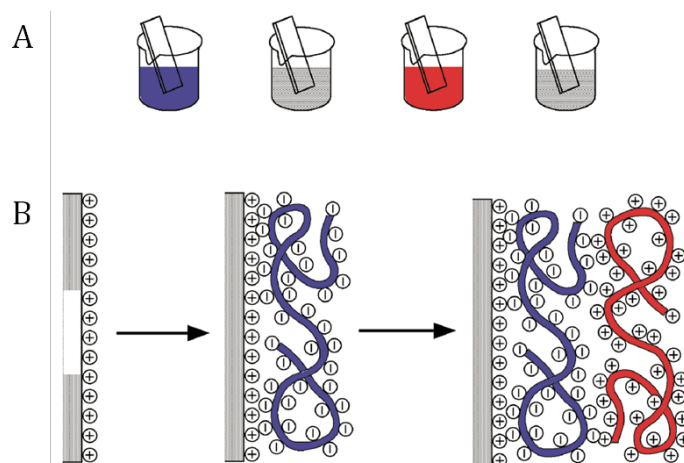


FIGURE 1.6: The LbL-coating scheme was adopted from Decher [129]. The polymer that is applied first bears the opposite charge compared to the substrate surface charge (in blue), the first layer is then washed (in grey), before the next polymer with the opposite charge compared to the first layer is applied (in red).

diazonium salts [119, 120] or the electrochemical oxidation with HNO_3 [121, 122]. Surface charge also influences hydrophobic/hydrophilic properties of a surface, with hydrophilic surfaces also mostly preferred for bacterial attachment [123]. Besides providing the electrode surface with charged moieties, electrodes can be coated with conductive polymers to enhance not only hydrophilicity but improve electrical properties of the electrode at the same time. Applied polymers are polyaniline [124], polypyrrole [125, 126] or poly(3,4-ethylenedioxythiophene) [127]. Electrical properties of the coating were also improved by coating with redox active substances, e.g. anthraquinone or naphthaquinone and Os or Ni containing polymers [114, 128]. A quantitative comparison of the named approaches is omitted at this point due to the multi-variability of the applied MFC systems (as described in section 1.1).

1.5.1 Layer-by-Layer coating

The method of choice for electrode surface modification in this work was layer-by-layer adsorption from liquid polymer solution, also known as “electrostatic self-assembly” (in the following abbreviated with LbL). The coating method that is based on the consecutive adsorption of polyanions and polycations to a surface was first published by Gero Decher in 1997 [129] and is described briefly in the following.

The substrate is dipped sequentially to alternately charged polyionic solutions and by the electrostatic repulsion of identically charged ions only one polymer-molecule per coating adheres to the substrate’s surface (theoretically) (see basic principle in Figure 1.6 [129]). Due to electrostatic attraction the consecutive polyion then adheres to the previous layer in red in Figure 1.6). Central to this method are washing steps, performed in between oppositely charged polyions (in grey in Figure 1.6). This prevents a contamination of the second polyionic solution with the first which would cause agglomeration and precipitation of the polymers, thereby disturbing the coating process.

Major advantage of this method is its simplicity and reproducibility, as well as the versatility of coatings that can be applied. The very basic principle of LbL coating that

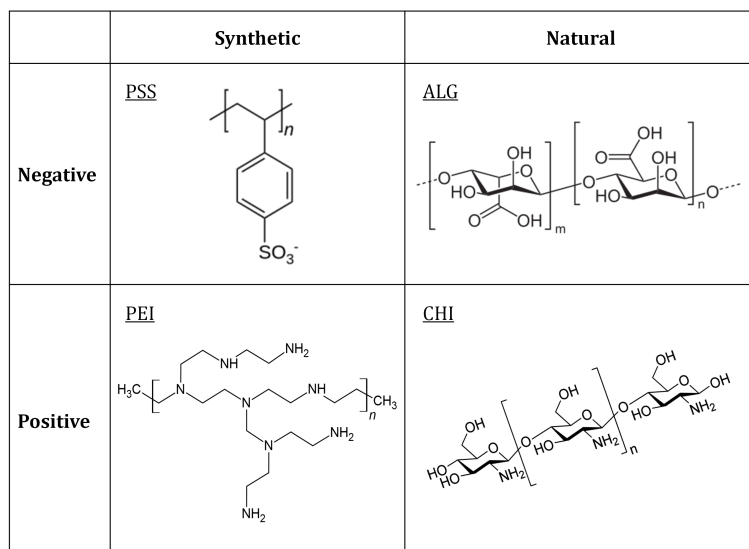


FIGURE 1.7: Polyelectrolytes PSS, ALG, CHI and PEI are used in LbL-coating. PSS and ALG are negatively charged and PEI and CHI positively, ALG and CHI are natural polyelectrolytes, PSS and PEI are synthetic.

is shown in Figure 1.6 is called immersive assembly and has been highly advanced to a multiplicity of coating methods and materials used. Methods include spray- and spin-coating, electromagnetic coating, but also ink-jet printing of polymeric substances, assembly of hybrid layers of inorganic and organic compounds, inclusion of particles between the layers, as well as LbL assembly of 3D printed cell layers [130].

Regardless of the method, the LbL coating aims to modify the physico-chemical properties of the surface with different objectives. In biomedical application for example the goal is mostly to facilitate adhesion of mammalian cells to a substrate (as in tissue engineering) and prevent bacterial adhesion to inhibit inflammatory responses, especially in dentistry [131, 132]. Guo and colleagues summarised how LbL-coating alters surface charge, surface wettability, stiffness of the surface as well as surface roughness and its impact on cellular adhesion. Surface charge can be easily altered by choosing the terminal polymer; the polyelectrolytes used in this work (with the implied charge) are shown in Figure 1.7. Surface wettability or hydrophobicity can also be influenced by the choice of polyelectrolytes, e.g. by introducing fluorinated polymers [133], or polymers with alkyl side-chains [134], as well as the attachment of polyethylene glycol (PEG) moieties [135, 136].

As mentioned earlier, surface hardness also impacts bacterial adhesion which can be influenced using LbL-coating. Mechanical stiffness of the coating depends on film swelling, which in turn highly depends on pH and salt concentration of the coating solutions and the medium [137]. The impact of salt on the film thickness is also illustrated in the coating scheme in Figure 1.6 B, with the coiled lines indicating polymers that are not necessarily spread flat on the surface. The architecture of the polyionic film is very reproducible, with the requirement that the ionic strength of the coating solution remains constant [138]. Higher ionic concentration generally increases film thickness due to low molar mass ions from the solution binding to the polymer and thereby leading to that coiled conformation [139, 140]. However,

excessively high ion concentration can also lead to detachment of layers and delayed adsorption due to blocking of the polymers' ionic binding sites [138].

Not only coating stiffness but also surface roughness is influenced by the salt concentration of the coating solution [141]. Roughness is a measure for irregularities on a coated 2D surface and can be categorised into microscale (from 1 to 100 μm), submicron (100 nm to 1 μm) and nano-roughness (less than 100 nm) [131]. It was shown that surface roughness can increase with increasing ion concentration [141].

1.6 Biofilm analysis

The *G. sulfurreducens* biofilm on the anode is the centre of interest of MFC experiments in this work and was analysed under various aspects. Methods for biofilm analysis are diverse and comprehensively summarised in [142]. The method of choice depends on the stage of biofilm formation that should be analysed, the point of interest (EPS or cells) and whether the method should be *in situ* or *ex situ*. For productive biofilms, analysis of the product adds on top. In this work, chronoamperometry was used to measure productivity of the electroactive *G. sulfurreducens* biofilms, biofilm morphology and thickness was analysed using Confocal Laser Scanning Microscopy (CLSM) and electrochemical properties were measured with electrochemical impedance spectroscopy (EIS).

1.6.1 CLSM

Confocal microscopy allows highly resolved biofilm inspection in three dimensions, thereby gathering spatial and structural information, necessary for example to quantify biofilm thickness. The difference to epifluorescence microscopy is the optical sectioning of the image that is achieved by focussing the laser beam with a spatial filter (pinhole or slit). The specimen is then confocal with the point of light emerging from the pinhole and fluorescence from outside the focal plane of interest is excluded. The final image is generated by scanning the specimen point-by-point and reconstructing the single images mathematically to a whole 3D representation [143].

Prerequisite for CLSM is the fluorescence of the specimen. In combination with various fluorophores, selected components (EPS or single species in a multi-species biofilm) within the biofilm can be localised for example using *in situ* hybridisation of fluorescent probes [144]. Alternatively, cells can be stained with nucleic acid dyes like SYTO9 or SYBR-green [145]. With SYTO9 in combination with propidium iodide (PI) the spatial distribution of viable and non-viable cells can be analysed. SYTO9 is cell permeable while PI is not, so that dead cells appear red (to yellow) while viable cells are stained in green [146]. However, this only allows endpoint analysis of the biofilm since the dyes are cell lethal. *In vivo* analysis is possible with genetically modified strains expressing genes coding for fluorescent proteins like GFP or mCherry (induced auto-fluorescence) [147, 148]. Although, it can be laborious to construct these strains it is so far the most common way for 4D biofilm analysis (x-y-z-time).

1.6.2 EIS

Apart from biofilm thickness and structure, the electrical properties of electroactive biofilms are of interest for MFC characterisation. Those can be analysed with EIS which is a non-invasive method and allows *in situ* biofilm analysis [149]. EIS is used

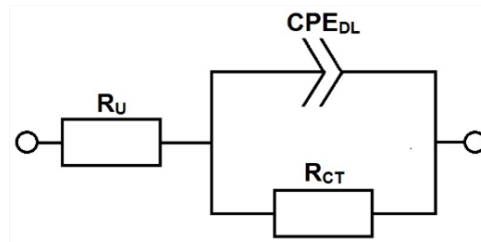


FIGURE 1.8: Equivalent electrical circuit to fit EIS data from MFC experiments. R_U : electrolyte resistance, R_{CT} : charge transfer resistance, CPE_{DL} : double layer constant phase element.

to measure resistances occurring in the MFC system, namely internal resistance of the biofilm, electrolyte resistance, resistance induced by the membrane and charge transfer resistance occurring at the electrode surface [150]. When analysing BES with EIS a potential (or current) is applied to the working electrode that alternates in small amplitudes from the system's open circuit potential. In the course of the measurement the frequency of the applied potential is varied from high to low frequencies (commonly from 100 kHz to around 50 mHz) and the resulting current and phase shift are measured. The impedance (Z), i.e. the resistance under applied potential (or current), is defined as the ratio of applied potential and the induced current, and depends on the frequency of the alternating potential and the phase shift of the current. By mathematical definition it can further be subdivided into an imaginary (Z_{IMAG}) and a real fraction (Z_{REAL}) [151].

Data can be fit to a Randles type equivalent circuit that allows to calculate charge transfer resistance R_{CT} and electrolyte resistance in the system from the equivalent model (Figure 1.8).

The measured impedance can additionally be illustrated as Bode plot which plots Z_{TOT} (the total impedance) and the phase shift against the applied potential frequency or in the Nyquist plot which distinguishes $-Z_{REAL}$ vs. Z_{IMAG} . For example see Figures 4.24 and 4.25 in chapter 4.7.2).

Chapter 2

Objective

Even though energy generation from waste via MFC cannot yet compete with traditional wastewater treatment, its sustainable potential justifies additional research effort. MFC productivity benefits significantly from efficient bacteria-electrode interaction, especially since *Geobacteraceae* which dominate current producing communities require direct contact to the anode for electron transfer. Within this work, current output of *G. sulfurreducens* MFC should be increased and production start-up time decreased by altering surface chemistry of the electrode. According to previous analyses on bacterial adhesion to electrodes it was hypothesised that a positive surface charge should have a positive impact on MFC performance. To test this hypothesis the following tasks had to be performed in advance:

- Establish a routine for LbL-coating of GAC, graphite and ITO electrodes
- Establish a method for surface charge determination for both particles and planar electrodes
- Determine the statistical robustness of MFC in H-cells on graphite electrodes
- Identify optimum poised potential for MFC on ITO electrodes

Finally, MFC performance on LbL-modified surfaces with different chemical surface properties should be tested. As MFC in H-cells only allows endpoint analysis of electroactive biofilms, the effect of surface coating should also be tested *in situ* in an electrochemical flow cell developed by Stöckl et al. [149]. This system allows the observation of the initial phase of biofilm formation (cellular adhesion) which is supposed to be mainly influenced by the coating. Preparatory tasks for flow cell experiments were:

- Optimise the flow cell design for facilitated handling
- Establish the fluorescent strain *G. sulfurreducens* mCh in the flow cell system

Conducting the according research should help optimising bacteria-surface interaction in MFC and thereby increasing overall current production efficiency.

Chapter 3

Material and Methods

3.1 Chemicals

All chemicals were of at least analytical grade and purchased from Roth (Roth, Karlsruhe, Germany), Sigma-Aldrich (Sigma-Aldrich Chemie GmbH, Taufkirchen, Germany) or Fluka (Fluka™ Analytical, Leicestershire, UK).

3.2 Bacterial strains and conditions

G. sulfurreducens strain PCA (DSM 12127) was obtained from DSMZ (German Collection of Microorganisms and Cell Cultures GmbH, Braunschweig, Germany) (wildtype as WT in the following), *G. sulfurreducens* mCherry (*G. sulfurreducens* mCh in the following) was kindly provided by Derek Lovley's group (Microbiology Department, UMass Amherst, USA). The strain was originally constructed for the use with a green fluorescent pH sensitive dye to analyse the change of pH in a biofilm in real-time [148]. The plasmid backbone is based on pCM66 which is a broad-host vector described in [152]. Kanamycin resistance was exchanged for spectinomycin, a *taclac* promoter introduced and the multiple cloning site exchanged for the one from pCD342 in [153]. The insertion of the *mCherry* gene led to the plasmid pRG5mCh [154].

All cultivations were done anaerobically in serum flasks sealed with a butyl septum (Glasgerätebau Ochs, Bovenden, Germany). Flasks were incubated shaking at 30 °C and 180 rpm (Shaking throw 25 mm, Ecotron Infors HT shaker, Bottmingen, Switzerland). Growth medium was DSM826 and contained (per liter): 0.1 g KCl, 1.5 g NH₄Cl, 0.5 g Na₂HPO₄, 0.82 g Na-Acetate as electron donor (equals 10 mM), 4.8 g Na₂-fumarate as electron acceptor (equals 30 mM), 2.5 g NaHCO₃, 10 ml of vitamin mix and 10 ml of trace mineral mix. Vitamin mix contained (per liter): 2 mg biotin; 2 mg folic acid; 10 mg pyridoxine-HCl; 5 mg thiamine-HCl × 2 H₂O; 5 mg riboflavin; 5 mg nicotinic acid; 5 D-Ca-pantothenate; 0.1 mg vitamin B₁₂; 5 mg p-aminobenzoic acid and 5 mg lipoic acid. Trace element solution contained (per liter): 1.5 g nitrilotriacetic acid; 3 g MgSO₄ × 7 H₂O; 0.5 g MnSO₄ × H₂O; 1 g NaCl; 0.1 g FeSO₄ × 7 H₂O; 0.18 g CoSO₄ × 7 H₂O; 0.1 g CaCl₂ × 2 H₂O; 0.18 g ZnSO₄ × 7 H₂O; 0.01 g CuSO₄ × 5 H₂O; 0.02 g KAl(SO₄)₂ × 12 H₂O; 0.01 g H₃BO₃; 0.01 g NaMoO₄ × 2 H₂O; 0.03 g NiCl₂ × 6 H₂O; 0.30 mg Na₂SeO₃ × 5 H₂O; 0.40 mg Na₂WO₄ × 2 H₂O). The medium containing all components except for fumarate, NaHCO₃ and vitamin solution was degassed with N₂/CO₂ (80%/20%) (Aligal 12™; Air Liquide, Paris, France) gas mixture for 90 min, afterwards NaHCO₃ was added and medium transferred to an anaerobic chamber (Rigid Chamber, Coy Laboratory Products Inc., Grass Lake, Michigan, USA).

Each 48 ml medium were aliquoted under N₂/H₂ (95%/5%) atmosphere (forming gas) to 250 ml serum flasks, sealed with a butyl septum and the septum secured with aluminium caps (Glasgerätebau Ochs, Bovenden, Germany). Then the forming

gas atmosphere was exchanged by evacuating the flasks three times and refilling them with N₂/CO₂ gas mixture. Subsequently serum flasks were autoclaved.

Prior to microbial cultivation, 1.5 ml Na₂-fumarate (160 g l⁻¹) (if not indicated differently) and 0.5 ml vitamin solution were added to each flask and degassed for another 15 min to remove any oxygen that might have diffused through the septum during storage of the flask. For *G. sulfurreducens* mCh 250 µg l⁻¹ spectinomycin were supplemented additionally as selection marker. Prior to inoculation, medium and inoculum were pre-warmed for 30 min and 1.5 ml of a stationary culture (maintenance culture) used to inoculate a fresh culture. The maintenance culture was stored for maximum two weeks in the dark at 4 °C, and refreshed every two weeks from cryo culture.

For cryo cultures, early stationary phase cells were mixed with oxygen free DMSO in an anaerobic chamber to a final DMSO concentration of 7 % and each 3 ml aliquoted to 5 ml cryo vials with a pre-adjusted N₂/CO₂ gas atmosphere (Glasgerätebau Ochs, Bovenden, Germany). Cryo cultures were stored at -80 °C. When cultures were inoculated from cryo culture, growth medium was supplemented with 1 g l⁻¹ oxygen free yeast extract.

3.3 Sampling procedure for growth experiments

Growth experiments were carried out in triplicates and monitored by measuring optical density of the cell suspension at 600 nm (OD₆₀₀ in the following) with a photometer (Biochrom WPA CO7000; Biochrom, Cambridge, UK) and analysing metabolite concentration (acetate, fumarate, malate, succinate) in the supernatant using high pressure liquid chromatography (HPLC; see section 3.4). Growth kinetics were calculated using the R package “growthcurver” [155]. Shaking flasks were always transferred to the anaerobic chamber for sampling to avoid oxygen entry when drawing a sample. 0.8 ml sample were drawn with a syringe and transferred to a cuvette to measure OD₆₀₀ (no dilution necessary). Afterwards the sample was filtered with an 0.2 µm polyvinylidene fluoride (PVDF) filter (Roth, Karlsruhe, Germany) and transferred to an HPLC vial. Samples were stored at -20 °C until further use.

3.4 HPLC analysis

Na-Acetate, Na₂-fumarate, DL-malic acid and succinic acid (acetate, fumarate, malate and succinate in the following) concentrations were analysed with HPLC (Shimadzu Deutschland GmbH, Duisburg, Germany) using a Rezex™ ROA-Organic Acid H+ (8 %) column (300 mm x 7.8 mm) with a SecurityGuard Standard Carbo H+ cartridge (4 mm x 3 mm, both Phenomenex Ltd. Deutschland, Aschaffenburg, Germany), with a refractive index detector (RID-10A). Column method was: 5 mM H₂SO₄, 0.6 ml/min, 30 °C, 24 min. Injection volume was 10 µl. Retention times at the described conditions were: malate: 11.4 min, succinate: 13.9 min, acetate: 16.7 min; fumarate: 17.6 min. Concentrations of calibration standards for all components ranged from 0.5 mM to 100 mM and a calibration curve was determined separately for each new HPLC measurement. Results were always fitted linear and metabolite concentration calculated from the linear equation. R² was always > 0.997.

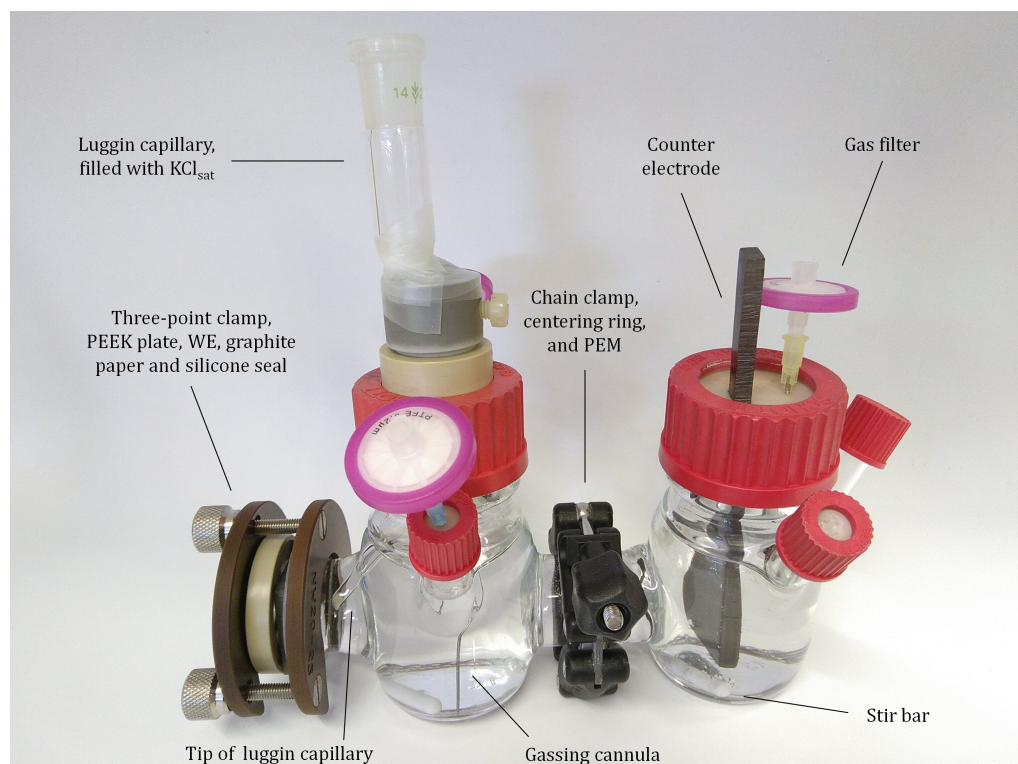


FIGURE 3.1: Modified electrochemical H-cell with a three electrode system (RE not shown but to be inserted to the Luggin capillary).

3.5 The electrochemical H-cell

3.5.1 Reactor construction

MFC experiments with *G. sulfurreducens* were carried out in a modified electrochemical H-cell as shown in Figure 3.1 (on the model of H-cells developed by M. Stöckl and used in [156]). The reactor consisted of two 100 ml glass bottles that served as anode and cathode chamber and were connected via two flanges of 25 mm diameter. In the following the anode will be called working electrode (WE), the cathode counter electrode (CE). The WE chamber was equipped with a second flange of identical diameter that served as attachment for the WE. In addition, both chambers had three (CE chamber), respectively two (WE chamber) GL14 glass joints arranged at a 45° angle to the glass bottle and sealed with 2 mm silicone septa for sampling and gas inlet/outlet. The chambers were separated by a proton exchange membrane (PEM) (diameter 28 mm, Nafion 117, QuinTech, Göppingen, Germany) and connected via a centering ring and a chain clamp (both EVAC AG, Grabs SG, Switzerland).

The WE was either a graphite poly propylene (PP) compound material (bipolar plate PPG86, referred to as “graphite” in the following; Eisenhuth GmbH & Co. KG, Osterode am Harz, Germany) or indium tin oxide (ITO) coated borosilicate glass (30 mm x 30 mm x 1.1 mm; resistance $20 \pm 6 \Omega$; Präzisions Glas & Optik GmbH, Iserlohn, Germany) and was attached to the flange with a 3-point-clamp (DN 25, material Pertinax, Neubert Glas, Geschwenda, Germany) and a 1 mm silicone seal in between glass flange and electrode. That left an electrode area of 4.9 mm² in contact with the electrolyte. Electrode densities, calculated for every MFC experiment, refer to that geometrical electrode area. Graphite WE were contacted using stainless steel

plates of 1 cm x 1 cm that were inserted between the backside of the electrode and a non-conductive PEEK plate (poly ether ether ketone). ITO WE were contacted using ring-shaped cut-outs of 0.13 mm thin graphite foil (type RCT®-DKA-SBGR) placed between the silicone seal and the conductive side of the ITO electrode and also secured in the 3-point clamp with a non-conductive PEEK plate.

For all H-cell experiments the CE was a paddel-shaped graphite electrode with a geometrical surface of 30.2 cm² in contact with the electrolyte, of which 12.2 cm² were facing towards the WE. The CE was inserted to the chamber via a silicone septum in the bottle lid. In order to stir the system, magnetic stir bars (material: polytetrafluorethylen (PTFE), cylindrical shape 25 mm x 6 mm) were added to each chamber.

For potential control, an Ag/AgCl reference electrode (RE) was placed inside a Haber-Luggin-capillary filled with either KCl_{sat} or 3 M Na₂SO₄. The Haber-Luggin-capillary was inserted through the lid of the WE chamber and fixed with a screw for positioning. The potential of the RE was checked against a so-called mother-electrode prior to each experiment. The mother-electrode served as reference point for the RE in the way that their potentials were measured against each other to ensure that the RE provided the correct reference potential as output. Potential of the Ag/AgCl electrode is -0.2 V vs. SHE. In the following all potentials are indicated vs. SHE.

Both chambers were filled with double-distilled water (ddH₂O) prior to autoclaving. For experiments with a graphite-WE the whole reactor was autoclaved as is (except for the RE). When ITO was used as WE the reactor was autoclaved with a graphite electrode as “dummy” electrode since there was no information available about stability of the ITO coating in wet heat. In this case WE and graphite foil contacting were assembled to the autoclaved reactor under a sterile workbench. Details on electrode preparation are described in the following paragraph.

3.5.2 Electrode preparation

To provide a fresh electrode surface for the cathode reaction, and to increase the geometrical surface for the counter reaction, the graphite CE was grind down with SiC-grinding paper prior to each experiment (FEPA grain size 600). When graphite was used as anode material the electrode was polished with SiC-paper to provide an even and comparable surface for all experiments (FEPA grain size 2400).

ITO electrodes were cleaned with a mix of 60 % 1-propanol/33 % 2-propanol/7 % ethanol (Bacillol®; Paul Hartmann AG, Heidenheim, Germany), rinsed with ddH₂O and sterilised in dry heat for 3.5 h at 80 °C prior to usage. New graphite foil contacting was cut out for each experiment and heat sterilised at the same conditions as ITO electrodes.

3.5.3 Electrochemical cultivation of *G. sulfurreducens* in H-cells

After autoclaving, ddH₂O was exchanged for *G. sulfurreducens* growth medium (not anoxic) omitting fumarate (110 ml CE chamber, 125 ml WE chamber) and setup under an incubator hood that was tempered to 30 °C (Certomat® H; B.Braun, Melsungen, Germany). In the incubator hood the H-cells were placed on magnetic stir plates and both chambers stirred at 120 rpm. Spinning direction was inverted every 2 min to support uniform biofilm growth. During the experiment the WE chamber was constantly degassed with N₂/CO₂ via a 12 cm cannula inserted through one of the GL14 glass joints. The gas flow rate was 30 ml/min, controlled with a rotameter.

Another short cannula was inserted through the second glass joint in the WE chamber and served as gas outlet. To allow sufficient oxygen influx into the CE chamber a cannula was also inserted through the silicone septum of this chamber. All cannulas were equipped with sterile PTFE filters (diameter 0.22 μm) to prevent contamination. Finally, electrodes (respectively the contacting) were connected to a potentiostat using alligator clips. Since different potentiostats were used, the respective potentiostat model is indicated individually for each experiment in the respective Results section. Current curves were recorded during the experiments and current density j calculated as current divided by available WE surface which was $(2.5\text{ cm}/2)^2 \cdot \pi = 4.9\text{ cm}^2$ for all H-cell experiments. As a second measure besides the current density the start-up time was analysed for each experiment. Start-up time was defined as the time until the current increased by 50 μA , respectively until current density had increased by 10 $\mu\text{A cm}^{-2}$.

Prior to inoculation the medium in the WE chamber was degassed with N_2/CO_2 for approximately 2 h. Open circuit potential (OCP) was recorded during this time and the establishment of a stable OCP was used as indicator for proper establishment of the $\text{CO}_2/\text{HCO}_3^-$ buffer system. When this is reached the pH in the anode chamber is 6.8 - 7.0. Afterwards, electrodes were polarised. Electrode potential varied among the MFC experiments and is indicated separately with the respective results.

Cells for H-cell experiments were grown in septum flasks in *G. sulfurreducens* growth medium for 42 h until early stationary phase and harvested by centrifugation (15 min at 4000 rpm at room temperature; Centrifuge 5180 R; Eppendorf, Hamburg, Germany). Cells were washed once with 0.125 M phosphate buffer and inoculated to the WE chamber to an OD_{600} of 0.15. All harvesting steps were carried out in an anaerobic chamber.

During the experiment samples were drawn for OD_{600} and metabolite analysis. Metabolite concentration was determined in the HPLC as described in section 3.4 and coulombic efficiency calculated from acetate consumption as described in the following section.

3.5.4 Calculating Coulombic Efficiency

Coulombic efficiency (η_C) was calculated as shown in Equation 3.1 according to [157] and [158], with the denominator being the charge transferred from the biofilm to the electrode during the experiment, z the number of electrons resulting from the complete oxidation from acetate to CO_2 (8 electrons), and $r_{e,m}$ the electron transfer rate given by acetate consumption; thereby $r_{e,m}$ is F (the Faraday constant = 96485 As/mol) times moles of acetate consumed during the experiment.

$$\eta_C = \frac{\int_{t=0}^t Idt}{8 \cdot r_{e,m}} = \frac{\int_{t=0}^t Idt}{8 \cdot F \cdot c_{ac,consumed}} \quad (3.1)$$

3.6 Biofilm analysis

To assess the impact of electrode material and applied potential on *G. sulfurreducens* biofilm formation biofilm thickness as well as viability were analysed.

3.6.1 Live/Dead staining

Non-fluorescent *G. sulfurreducens* WT biofilms were stained with fluorescent dyes SYTOTM9 Green Fluorescent Nucleic Acid Stain (Syto9) and Propidium iodide (PI; both InvitrogenTM, Waltham MA, USA) immediately after an experiment was aborted (also known as LIVE/DEADTM staining). Stock solutions in 0.125 M phosphate buffer were 6 μ M Syto9 and 30 μ M PI. Dyes were mixed 1:1 in a final volume of 400 μ l per biofilm (stained area 5 cm²). Electrodes with biofilms were carefully detached from the WE chamber, placed in a petri dish (5 cm diameter), overlaid with 400 μ l staining solution and incubated at room temperature for 15 min in the dark. Afterwards, staining solution was removed and the biofilm rinsed three times with 0.125 M phosphate buffer, a fourth buffer volume remained on the biofilm to avoid desiccation.

3.6.2 Imaging using CLSM

Microscopic images of the biofilms were taken immediately after the end of an experiment with an upright CLSM (TCS SP8, Leica Microsystems GmbH, Wetzlar, Germany) with galvanometric stage. In order to image the biofilm in a hydrated state, and thereby retrieving a realistic value for biofilm thickness, a dip-in objective was used (HC APO UVIS CS2, 63x magnification, numerical aperture 0.9, refraction index 1.33). For *G. sulfurreducens* WT biofilms laser intensity (OPSL 488) was set to 5 % and an excitation beam splitter DD488/552 was used with a PMT (photomultiplier tube) detector set to emission wavelengths between 500 and 545 nm (for the green channel) and the HyD between 615 and 788 nm (for the red channel). *G. sulfurreducens* mCh was imaged using the red fluorescence of the expressed mCherry protein. With OPSL 552 set between 20 and 30 % intensity (depending on the biofilm thickness and quality of the fluorescence signal) and PMT set between 555 and 795 nm. Images of a 185 μ m x 185 μ m large area were taken with various sizes in z-direction, at a step size of 0.63 μ m.

Leica software LAS X Version 3.5.5 (Leica Microsystems CMS GmbH, Wetzlar, Germany) was used for image evaluation.

In the following, CLSM images are shown with inverted colours (pink-blue on white background instead of green-red on black background) to improve visibility.

3.6.3 Measuring biofilm thickness

A method for quantitative determination of biofilm thickness was developed in order to analyse a high number of microscopic images semi-automated. The method is based on the programming language R [159] and published in [160].

First, x-z images of the biofilm were recorded on ten randomly picked areas on the biofilm covered anode. On these images ten regions of interest (ROI) were defined, each with one tenth of the image's width (18.5 μ m) (this is illustrated with Figure 3.2). Fluorescence intensity was recorded within the length of each ROI and plotted against the z-axis, resulting in a histogram as shown in Figure 3.3. The thickness of the biofilm can now be extracted from the range of the histogram in which fluorescence is above a certain threshold level, indicated by the dashed line in Figure 3.3. Histogram data can be exported from the LASX software as .csv files which are then input for the R script that calculates biofilm thickness.

The function of the R-script is explained in the following. The R-packages needed are *data.table*, *reshape2*, *dplyr*, *ggplot2* and *cowplot*. The .csv-files exported from the

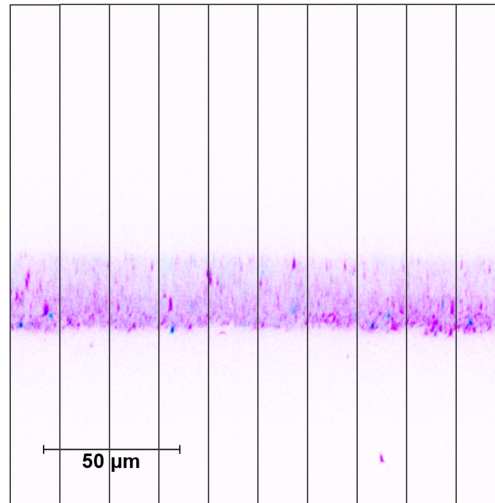


FIGURE 3.2: An x-z image of a Syto9 stained biofilm is shown with ten ROIs defined, each of $18.5\mu\text{m}$ width. Fluorescence intensity is recorded within the length of each ROI.

LASX software must be converted to UTF-8 first, otherwise the R function *fread* is unable to read the files. This can be done for example with the online tool “subtitletools”, available on <https://subtitletools.com/convert-text-files-to-utf8-online>.

```
library("ggplot2")
library("reshape2")
library("dplyr")
library("cowplot")
library("data.table")

# First, a list of all filenames is extracted from the folder in
# which the files are stored. The file ending .csv is used as the
# identifier (pattern)
filenames <- list.files("CLSM/Line profiln", pattern="*.csv", full.
  names=TRUE)

# All files are read with the function fread and stored in a list,
# combined with the file names
data <- lapply(filenames, fread)

# There is a separate column in which z-axis coordinates are stored
# for each ROI separately but since it is identical for each ROI,
# the redundant columns can be deleted.
# The argument of seq() depends on the number of ROI defined in one
# image. seq(3,19,2) applies for 10 ROI in one image.
data <- lapply(data, function(x) x[,-seq(3,19,2)])

# In "data" intensity values are arranged column-wise, which is
# then melted to a tidy data set with intensity values stored row-
# wise in "value" and the ROI names as identifier stored in "
# variable"
data_melt <- lapply(data, function(x) melt(x, id = c("Axis [m]")))
```

```

# An additional identifier column with the last part of the file
  name is added to link data with the information which electrode
  was analysed. Therefore path before filenames is removed (keep
  expression after square break; attention - sub() leaves blank
  space before the name)
filenames_short <- sub(".*]", "", filenames)
data_melt <- mapply(cbind, data_melt, "file"=filenames_short,
  SIMPLIFY=F)

# For easier data handling the tables are converted to data frames
df_data_melt <- do.call(rbind.data.frame, data_melt)

# Missing values are deleted from the data frames and the z-axis
  coordinates are converted from meter to micrometer
df_data_melt <- df_data_melt[complete.cases(df_data_melt), ]
df_data_melt$file <- as.factor(df_data_melt$file)
df_data_melt$`Axis [m]` <- df_data_melt$`Axis [m]`*10^6

# For each file-ROI combination an extra column is added which
  indicates the row with the maximum fluorescence intensity, i.e.
  the peak of the histogram (id_max). In addition a row number is
  added (id). This is needed later to identify the upper and the
  lower boarder of the biofilm
df_data_melt <- df_data_melt %>%
  group_by(file, variable) %>%
  mutate(id = row_number(),
  id_max = id[value == max(value)])

# Image pixels belonging to the biofilm (and not to the background)
  are defined as those with an intensity higher than 3*mean of
  the background signal. All background pixels are replaced with
  NA (an "empty" value). Since the background above (buffer and
  planctonic cells) and below the biofilm (electrode) have
  different background intensities the calculation is performed
  separately for left (first line; id < id_max) and right (first
  line; id > id_max) of the histogram's maximum. That is why the
  information about the histogram peak was stored in the data
  column "id_max" before. The threshold is defined here as 3-times
  the mean background intensity but for higher background signal,
  i.e. fluorescence of a different electrode material the
  threshold might need to be adapted (e.g. 2 time the background
  signal)

# Replace background with NA (separately for left and right of the
  peak)
replace_background <- df_data_melt %>%
  group_by(file, variable) %>%
  mutate(value = replace(value, id < id_max & value < 3*mean(head
    (value, n = 100)), NA),
    value = replace(value, id > id_max & value < 3*mean(tail
    (value, n = 100)), NA))

# Delete NA from data frame
no_background <- na.omit(replace_background)

```

```
# Plots of the data frames before and after subtracting the
  background signal to randomly check on the correctness of the
  threshold definition
minus_background <- ggplot(subset(no_background, file == " 2_5 z.
  csv"), aes('Axis [m]', value)) +
  geom_point(aes(colour = variable), size = 0.75) +
  scale_x_continuous(limits = c(0, 200)) +
  scale_y_continuous(limits = c(0, 200)) +
  xlab(expression(paste("z-axis in ", mu, "m"))) +
  ylab("Fluorescence intensity") +
  plot.options.legend +
  theme(legend.position = "none")

all <- ggplot(subset(df_data_melt, file == " 2_5 z.csv"), aes('Axis
  [m]', value)) +
  geom_point(aes(colour = variable), size = 0.75) +
  scale_y_continuous(limits = c(0, 200)) +
  scale_x_continuous(limits = c(0, 200)) +
  xlab(expression(paste("z-axis in ", mu, "m"))) +
  ylab("Fluorescence intensity") +
  plot.options.legend +
  theme(legend.position = "none")

plot_grid(all, minus_background, align = "v", nrow = 2)
```

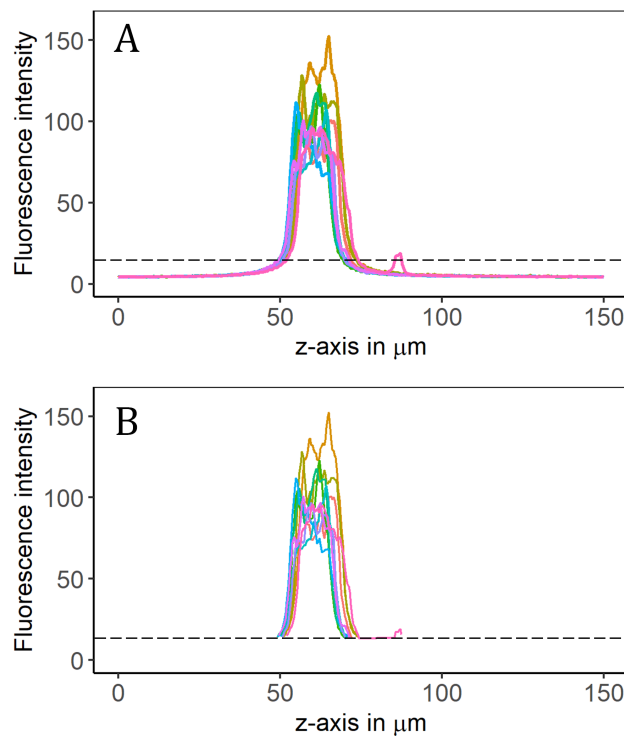


FIGURE 3.3: Plotting fluorescence intensity along the z-axis results in a histogram as shown in A. Each line represents the intensity recorded in one ROI. The dashed line indicates the intensity threshold that differentiates the biofilm signal from the background. Data plotted in B is the result after background subtraction. Here, a signal above threshold, caused by a planctonic cell floating above the biofilm, is visible. The signal would falsify thickness determination if not deleted by using the described method of choosing the first gap.

While the border between the electrode and the biofilm is defined as the point at which the intensity exceeds $3 \times \text{mean}(\text{background signal})$, it is more difficult for the "end" of the biofilm (the transition between the biofilm and the buffer). Even though the biofilm was washed prior to CLSM analysis, there can still be cells floating above the biofilm that disturb the measurement. These fluorescent spots on the image can have a signal intensity > 3 -times background intensity and thereby falsify the definition of the biofilm end (see example in Figure 3.3). A rescue for this is to define the first occurring case in the histogram at which the intensity is $< 3 \times \text{mean}(\text{background})$ as the biofilm end. Since row numbers were added to the data table and all background pixels were eliminated from the table afterwards, the first case for which fluorescence intensity $< 3 \times \text{mean}(\text{background})$ is the first gap in the consecutive row number column (with $\text{id} > \text{id}_{\text{max}}$, i.e. after maximum of the histogram). The gap can be detected by calculating the difference between entries of the row number column. Hence, the script "searches" for any difference other than 1 to search for the break in consecutiveness. While this solves the problem for the "end" of the biofilm, it might now overlook the "beginning" of the biofilm if there is no gap in the row number. This is bypassed by doubling the first row of each histogram. The difference in row number is then 0 for these cases and thereby grabbed by the script. When the difference is calculated, the resulting data column is one entry short compared to the

row number column, so an additional entry had to be added to the column (0 in this case) to allow the addition of this vector to the existing data frame. With the data prepared in this way statistical measures of the biofilm can be calculated, i.e. biofilm thickness and standard deviation (SD) for each z-image and each biofilm.

```
# Duplicates the first row of every file-variable combination
no_background2 <- no_background %>%
  group_by(file, variable) %>%
  slice(rep(1:n(), c(2, rep(1, each = n() - 1))))

# calculates the difference in rownumber between consecutive rows
diff <- diff(no_background2$id)

# adds an additional item to the end of the vector, number 0 in
  this case
diff[length(diff) + 1] <- 0

# adds the vector to the data frame
no_background2$diff <- diff

# This step extracts the gaps resulting from the deleted background
  , by filtering all rows for which the vector "diff" is not "1" (
  i.e. non-consecutive rows)
all_gaps <- subset(no_background2, diff != 1)

# For some images the background line left if the histogram (the "
  electrode-part") oscillates around values greater and smaller
  than 3*mean(background) which also causes gaps in the "diff"-
  vector but relevant to define the "End" of the biofilm are only
  values to the right of the maximum, i.e. id > id_max. The "End"
  of the biofilm is then the first value for each image-ROI (=
  file-variable) combination stored in the "Axis" column of the
  all_gaps2 data frame.
all_gaps2 <- all_gaps %>%
  group_by(file, variable) %>%
  subset(id > id_max)

end <- all_gaps2 %>%
  group_by(file, variable) %>%
  summarise(end = 'Axis [m]')[1])

# For the "Begin" of the biofilm in turn the last gap to the left
  of the maximum is relevant, i.e. id < id_max. The "Begin" of the
  biofilm is then the last value for each image-ROI (= file-
  variable) combination stored in the "Axis" column of the all_
  gaps_begin data frame.
all_gaps_begin <- all_gaps %>%
  group_by(file, variable) %>%
  subset(id < id_max)

summary <- all_gaps_begin %>%
  group_by(file, variable) %>%
  summarise(begin = tail('Axis [m]', 1))
```

```

# Values for the "End" are added to the data table in which the
  values for the "Begin" are already stored. Then, the biofilm
  thickness can be calculated as the difference between the z-axis
  coordinates for "End" and "Begin".
summary$end <- end$end
summary$thickness <- summary$end - summary$begin

# To summarise the results for each electrode, an electrode
  indicator is added to the table (there are 100 file-ROI
  combinations, therefore each electrode name is replicated 100
  times).
summary$electrode <- as.factor(rep(seq(1,6), each = 100))

# The result can be plotted split up to each image and ROI or
  summarised in a boxplot
ggplot(summary) +
  geom_point(aes(x = file, y = thickness, colour = variable)) +
  xlab("Filename") +
  ylab(expression(paste("Biofilm thickness in ", mu, "m"))) +
  theme(axis.text.x = element_text(angle = 270), legend.title =
    element_blank())

ggplot(summary) +
  geom_boxplot(aes(x = electrode, y = thickness), width = 0.2) +
  scale_y_continuous(limits = c(0, 50), breaks = seq(0, 50, 10)) +
  ylab(expression(paste("Biofilm thickness in ", mu, "m"))) +
  xlab("Electrode")

# Statistical indicators are calculated as mean and SD of biofilm
  thickness, first for each z-image, then for each biofilm. The SD
  in the summary per biofilm is calculated as error propagation
  from the variances (= SD2) of the z-image summary.
# Plotting the thickness calculated for each z-image allows to
  detect outliers and to visually compare them to the actual image
summary_z <- summary%>%
  group_by(file, electrode)%>%
  summarise(mean_1 = round(mean(thickness), 1),
            sd_1 = round(sd(thickness), 1))

summary_biofilm <- summary_z%>%
  group_by(electrode)%>%
  summarise(mean_sum = round(mean(mean_1), 1),
            sd_sum = round(sqrt(sum(sd_1^2)), 1))

```

Finally, some remarks on image acquisition in order to receive a valuable result. Aside from thoroughly stained biofilms, proper imaging is essential. The described method relies on the intensity difference between a background signal and the biofilm signal, hence the bigger the difference, the more reliable is the method. A thoroughly stained biofilm, that is rather too brightly exposed than too dark, leads to good results. In addition, the threshold ($3 \times \text{mean}(\text{background})$) was defined iteratively and might have to be adjusted in case the background to biofilm signal relation is different.

3.7 Layer-by-layer coating

Surface charge of activated carbon particles, planar graphite and ITO electrodes was modified using LbL-coating [129]. Since the coating procedure, as well as analysis of

the surface charge varies greatly for particles and planar electrodes, they are described separately in the following paragraphs.

3.7.1 Coating solutions

Four different coating solutions were prepared with the following polymers: chitosan (Poly(D-glucosamine), low molecular weight; Aldrich, St. Louis MO, USA) (**CHI**; positively charged), alginate (Alginic acid sodium salt, low viscosity; Alfa Aesar, Kandel, Germany) (**ALG**; negatively charged), polystyrenesulfonate (Poly(sodium 4-styrenesulfonate), average Mw 70000; Aldrich, St. Louis MO, USA) (**PSS**; negatively charged) and polyethyleneimine (50 % (w/v) in H₂O; FlukaTM Analytical, Leicestershire, UK) (**PEI**; positively charged). All coating solutions consisted of 1 g l⁻¹ polymer, 0.2 M NaCl and 0.05 M NaOAc in ddH₂O. pH was adjusted to 5.6 with acetic acid. ALG was pre-dissolved in ddH₂O and CHI in 1 % (v/v) acetic acid. Prior to use, coating solutions were filtered using 0.22 μm PVDF filters and fresh coating solutions were prepared for every experiment.

3.7.2 Coating of GAC_{mag}

For application in a fluidised bed reactor, GAC_{mag} was coated with the above mentioned polymer solutions. GAC_{mag}, developed by M. Stöckl in [107] (patent [108]), was chosen due to its advantage in handling since the particles can easily be retained during sampling due to their magnetic properties.

For coating 1.5 ml polymer solution were added to 25 mg particles in a 2 ml eppendorf tube. Tubes were inserted to a tube revolver (Roth, Karlsruhe, Germany) and coated rotating for 10 min at room temperature. After each layer, the coating solution was discarded and particles were washed three times with ddH₂O. For washing, the magnetic particles were attached to the tube wall with a magnet, ddH₂O was discarded, fresh water added and particles washed by inverting the tube 5 times. Negatively and positively charged polymers were always coated alternately. The respective coating combinations are indicated individually in the Results section.

To analyse the interaction of LbL-coatings with ions from buffer or medium, coated particles were incubated in 0.125 M phosphate buffer, resembling ionic strength of the *G. sulfurreducens* medium but without the need of a gas tight compartment required for the CO₂/HCO₃⁻ equilibrium in the actual medium. 25 mg particles were incubated in 2 ml buffer for 18 h in the tube revolver.

3.7.3 Zeta sizer

Surface charge of coated particles was analysed with a Zetasizer® (Nano ZS; Malvern Panalytical, Malvern, UK) [161]. Here, analysis of the surface charge is based on the particle's mobility in an electrical field. 25 mg coated particles were diluted in 1 ml ddH₂O and filled in a folded capillary cell (DTS1060). To avoid particle sedimentation at the bottom of the cell, the cell was stored in a horizontal position until insertion into the instrument. Zeta potential was measured at 23 °C, with water set as solvent and carbon as particle material.

3.7.4 Coating of planar electrodes

Planar graphite and ITO electrodes were stored in 5 cm petri dishes and either overlaid with or completely immersed in coating solution. A different dish was used for each

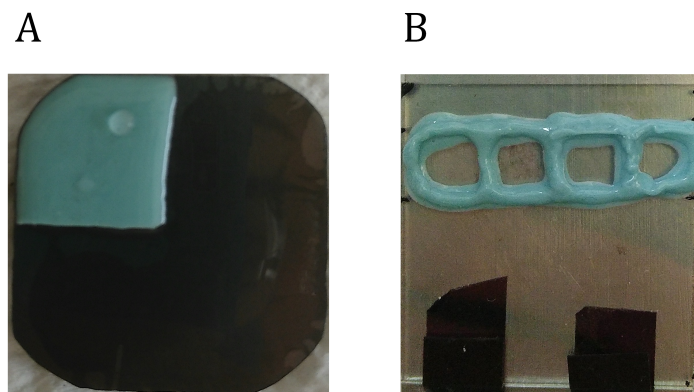


FIGURE 3.4: A) Graphite electrodes were partly covered with silicone to apply different numbers of layers on one electrode. B) Four cavities were marked on ITO electrodes to analyse different coating compositions.

solution to avoid cross-contamination. The petri dishes were shaken in an orbital shaker at 70 rpm (Shaking throw 10 mm; Incubator ES-20; Biosan, Riga, Latvia) for 15 min at room temperature. After each layer the coated electrode was removed from the petri dish and washed three times with ddH₂O.

To parallelise surface charge analysis electrodes were divided into different sections with two-component duplicating silicone (Picodent twinsil®; Wipperfurth, Germany) to prepare multiple coatings on one electrode. For example: Half of the electrode was covered with silicone, four layers ((PEI-PSS)₂) were coated on the other half, then the silicone was removed and a final layer PEI applied, resulting in the coatings (PEI-PSS)₂-PEI and PEI₁ on one electrode (Figure 3.4 A).

To test the interaction between salts from the *G. sulfurreducens* growth medium and the polyelectrolyte coating, LbL-coated graphite electrodes were incubated in phosphate-buffered growth medium (w/o fumarate, hence resembling the medium in the WE chamber in H-cell experiments) for 64 h (shaking at 120 rpm, shaking throw 10 mm). Coated electrodes were analysed with a height-regulated scanning Kelvin probe (HR-SKP; further explained in the following section) before and after incubation.

In order to compare the coatings, which were applied in H-cell experiments on ITO electrodes at once, the electrode was again treated with silicone. A grid was created with, resulting in four cavities that were then coated individually. The electrode with the grid and mounted on a steel plate for HR-SKP analysis is shown in Figure 3.4 B). Each cavity was overlaid with 200 µl coating solution and coated for 10 min at 70 rpm. The coating solution was carefully removed with a pipette, not to cross-contaminate the cavities and washed three times with 200 µl ddH₂O. Then, the next layer was applied. After the final washing the electrode was air dried and the silicone removed. The coated electrode was analysed with the HR-SKP that scanned the surface from left to right and thereby analysed the surface potential across all cavities.

For application of coated ITO electrodes in H-cell experiments an "in-place" coating setup was chosen (see Figure 3.5). To ensure that the coating did not electrically impair the contact between the conductive ITO layer and the graphite paper used for contacting, a sterilised electrode together with the contacting was mounted on a sterile half cell and stored in a sterile workbench. 1 ml coating solution was added



FIGURE 3.5: One WE chamber is shown, prepared for LbL-coating. The ITO electrode and graphite paper were mounted to the glass body and coating solution was added through the second flange. During incubation the flange was covered with parafilm. Reactors were incubated shaking in this upright position.

via the flange that later connects the two chambers, the flange was sealed with parafilm (Pechiney Plastic Packaging, USA) and the WE chamber incubated shaking at 100 rpm (shaking throw 25 mm, Ecotron Infors HT shaker) at room temperature for 15 min. After each coating step the coating solution was removed, three times 2 ml sterile ddH₂O was added and the WE chamber gently shaken to remove any remaining coating solution. Subsequently to the washing procedure after the final coating layer, the WE chamber was reassembled with the Nafion membrane, the CE chamber and the Luggin-capillary (all sterilised in advance) and immediately filled with *G. sulfurreducens* growth medium without fumarate to omit drying of the LbL-coat. Hereafter, the experimental procedure was as described in 3.5.3.

Coating with fluorescent polyelectrolytes

Rhodamine-labelled PSS and PEI were supplied by Surflay Nanotech (Berlin, Germany). PEI^R: label degree monomer/dye 361, Mw 750 kD; PSS^R: label degree 167, Mw 70 kD. Coating solutions were prepared as described in section 3.7.1. Two different coatings were prepared to test if PSS or PEI was more suitable as basal coating layer. (PEI^R-PSS)₂-PEI^R and (PSS^R-PEI)₂-PSS^R were prepared as described in section 3.7.4, mounted to an H-cell filled with anoxic medium and polarised at +0.1 V vs. SHE.

To assess whether parts of the coating were detached from the electrode during electrode polarisation and incubation in *G. sulfurreducens* medium, samples were taken from the WE chamber and fluorescence measured in a microplate reader (Spark®, Tecan; Männedorf, Switzerland). Fluorescence emission was scanned from 570 to 700 nm with an excitation wavelength of 525 nm and resulting spectra compared with spectra of diluted coating solutions. The lower detection limit for PEI^R and PSS^R was 1 mg l⁻¹ (gain 200).



FIGURE 3.6: A sample in the HR-SKP chamber with the tip positioned few μm above the measured surface.

After 111 h the H-cell experiment was aborted and the electrodes analysed with the CLSM. Rhodamin-tagged polymers were imaged at the same conditions as mCherry fluorescence (described in section 3.6.2) but with lower laser intensity (7 %).

3.7.5 Height-regulated scanning Kelvin probe

Since the electrophoretic principle of the Zetasizer® is not applicable to determine surface potential of a planar surface, the HR-SKP was used for this purpose (SKP KM, Wicinski-Wicinski GbR, Surface Scanning Systems, Germany). The tip of the Kelvin probe (shown in Figure 3.6) acts as a contactless vibrating capacitor and thereby measures the Volta potential of a conductive surface. The method is described thoroughly in [162–164]. Before each measurement the probe was calibrated at measurement conditions (humid air > 90 % relative humidity) with a Cu/CuSO₄ as RE. The measured potentials are displayed relative to SHE. The scanned surface area differed among the experiments and is indicated separately in the results section; the scanning step size was always 50 μm in x- and y-direction.

The coated electrodes were stored in ddH₂O until shortly before the measurement to preserve the LbL structure as well as possible. The samples were air dried before starting the analysis. ITO electrodes, since they are conductive on one side only, were attached to a steel plate using carbon adhesive pads, thereby connecting the conductive upper side of the sample with the non-conductive bottom side and the steel plate. The steel plate then contacts with the HR-SKP table. Graphite electrodes were inserted into the HR-SKP as they are.

3.8 Adhesion of bacteria to coated particles

As a quantification measure for attachment of bacterial cells to (coated) GAC_{mag}, OD₆₀₀ reduction in the supernatant was determined when particles were incubated in a cell suspension. Adhesion of *G. sulfurreducens* to coated GAC_{mag} was tested in 100 ml septum flasks, with two flasks containing 0.1 g (coated) particles and one without particles as OD₆₀₀ reference. Therefore, 150 ml *G. sulfurreducens* were cultivated until stationary phase and inoculated to 3 x 25 ml anoxic, sterile phosphate buffer (0.125 M, pH 6.8) with or without particles. All flasks were degassed with N₂/CO₂ for 45 min,

and frequently shaken during degassing, to remove any oxygen bound to the particles. After inoculation, GAC_{mag} were immediately accumulated on the flask wall with a magnet and the t_0 sample taken. In the following, samples were taken every 5 min until 20 min post inoculation, time intervals were then longer, until the last sample was taken after 150 min. Incubation of the flasks was carried out shaking at 180 rpm and 30 °C.

3.9 The electrochemical flow cell

3.9.1 Reactor construction

The electrochemical flow cell used in this work is a further development of the system developed by Stöckl et al., described in [149].

The cell was made from PEEK by the DECHEMA workshop and consists of two chambers, separated by a PEM. The construction plan is shown in Figure 3.7. The PEM was placed between two 1 mm silicone seals, which were then placed in the recess on the CE chamber (Figure 3.9 B). The ITO electrode was contacted with a Pt-frame (0.025 mm thin, frame width 2 mm; Chempur, Karlsruhe, Germany), which was then secured with a brass screw, that served as adaptor for a banana jack (component 1 in Figure 3.8). The shiny silverish rectangle (component 3 in Figure 3.8) is the flag of the frame that is hold in place by the brass screw. The Pt-frame stayed attached to the WE chamber and was not disassembled for cleaning.

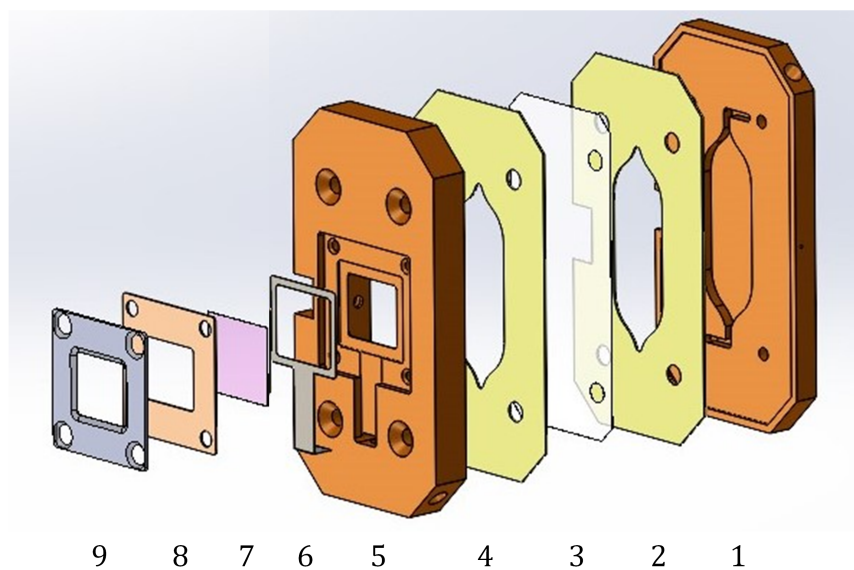


FIGURE 3.7: Assembly of the flow cell is shown schematically. From right to left (bottom to top in the assembled flow cell): CE chamber (1), silicone seal (2), PEM (3), silicone seal (4), WE chamber (5), Pt contacting frame (6), ITO anode (7), silicone seal (8), stainless steel frame (9).

For flow cell experiments ITO coated cover glass was used as WE to allow observation of the biofilm through the electrode. Since the immersion objective of the microscope is manufactured to compensate for the refraction of a 0.175 mm thin cover glass, no thicker electrode could be used. ITO coated borosilicate glass of size 20 mm x 22 mm x 0.175 mm, resistance $20 \pm 5 \Omega$ (Präzisions Glas & Optik GmbH, Iserlohn,

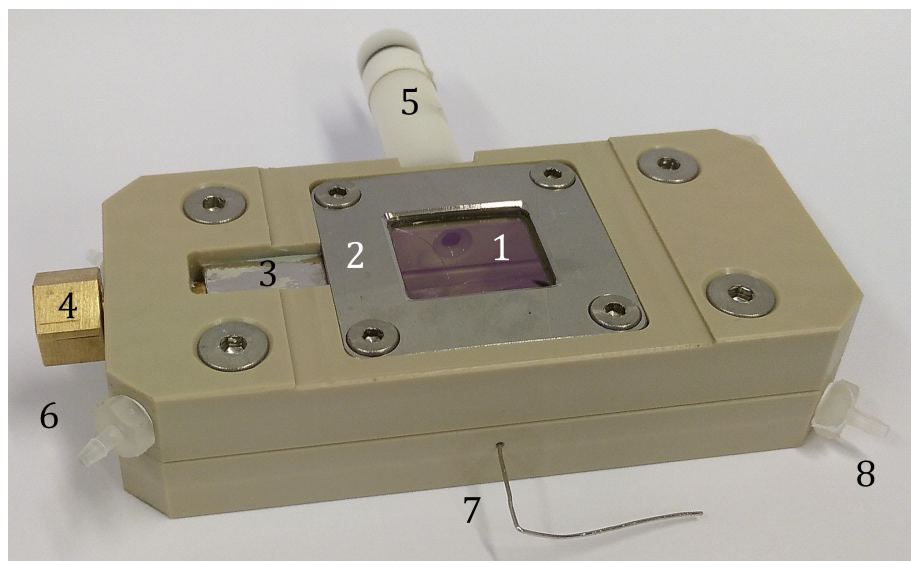


FIGURE 3.8: Flow cell with ITO (1) anode and steel frame for attachment on top (2), Pt-contacting (3) to the brass screw (4) used for anode contacting, inserted RE (5), WE chamber influx (6), Pt-wire for cathode contacting (7), CE chamber efflux on the right (8).

Germany) was used as electrode. The electrode was pre-treated as described in section 3.5.2 and afterwards inserted into the WE chamber with the conductive side facing the Pt-frame. Another 1 mm silicone seal was placed on top of the electrode before the whole construction was fastened with a 1 mm stainless steel frame. Due to the thin glass the screws could not be tightened very much, therefore the silicon seals were not sufficient to entirely seal the electrode-Pt-contact, unfortunately. It is crucial to prevent electrolyte from entering the electrode-Pt-contact since this would perturbate the electrochemical system. Therefore, a thin silicone frame (the same as used in 3.7.4) was applied manually as additional seal.

After the WE was mounted to the WE chamber, both chambers (with the PEM-sandwich) were screwed together and the RE (RE-3VT RE screw type (Ag/AgCl, 3 M NaCl), ALS Co., Ltd, Tokyo, Japan) was inserted through the hole seen on the front side of the WE chamber in Figure 3.9 A. Afterwards, the tubing was attached to both chambers (tubing material: PharMed®-BPT, inner diameter: 0.8 mm) and a bubble trap inserted to the WE influx tube (Figure 3.10, component 3). The WE reservoir was constantly degassed with N_2/CO_2 and gas bubbles, which might emerge via the tubing, should be caught in the bubble trap instead of accumulating at the WE. All above mentioned assembly steps were done in a sterile workbench.

After attachment of the tubings, flow cell plus tubing was transferred to an incubator hood where tubes were connected to the reservoirs filled with each 50 ml *G. sulfurreducens* growth medium (without fumarate). The set-up used for preparatory experiments without operation together with the CLSM is shown in Figure 3.10. The tubes were connected to the reservoir bottles with 12 cm cannulae via a septum in the bottle lid (see components 1 and 2 in Figure 3.10). In addition, one short cannula for oxygen influx was inserted to the CE reservoir (component 2), and one for pressure relief to the WE reservoir. Gas inlet and outlets were equipped with sterile PTFE filters (diameter 0.22 μm) to prevent contamination.



FIGURE 3.9: The two chambers of the flow cell are shown; with (A) the WE with the transparent ITO anode atop the chamber and (B) the CE chamber with the platinum cathode.

Electrolytes were pumped through the flow cell with a peristaltic pump (REGLO Digital MS-2/6; Ismatec, Wertheim, Germany) at 0.5 ml min^{-1} , if not indicated differently.

Any technical dimensions of the flow cell are listed in Table 3.1.

3.9.2 Sterilisation procedure

Tubing was sterilised with a clean-in-place (CIP) procedure: First, tubing was flushed with ddH₂O for 30 min at 2 ml min^{-1} , then with 2 M NaOH for 30 min at 1 ml min^{-1} , followed by 70 % EtOH for 30 min at 1 ml min^{-1} . Finally tubing was cleaned with sterile ddH₂O for 45 min at 1 ml min^{-1} .

Both flow cell chambers were autoclaved disassembled, together with the bubble trap that was autoclaved filled with water, and the silicone seals and the membrane, that were autoclaved in a beaker filled with water.

TABLE 3.1: Technical dimensions of flow cell components.

Component	Dimension
Bubble trap	20 mm diameter; 5 ml volume
Pt CE	15.9 mm x 27.4 mm; 4.36 cm^2 area
ITO WE	14.3 mm x 12.7 mm; 1.8 cm^2 area
CE chamber volume	50 mm x 15.9 mm x 2.8 mm; 2.2 ml volume
WE chamber volume	50 mm x 15.9 mm x 7 mm; 5.6 ml volume
Width influx and efflux channels	2 mm
Width Pt frame WE contacting	2 mm
Outer dimensions	41.1 mm x 82.1 mm x 19.6 mm



FIGURE 3.10: The experimental set-up of the flow cell in the incubator hood (without the CLSM) is shown. Component 1 is the WE reservoir, 2 the CE reservoir and 3 the bubble trap.

The RE was first slewn in 70 % EtOH for 30 s and then cleaned with sterile ddH₂O before insertion to the WE chamber.

3.9.3 MFC in flow cell setup

After setting up the flow cell under the incubator hood the WE electrodes were connected to a Gamry Interface1000 potentiostat (Gamry Instruments, Warminster, PA) and OCP measurement was started. The whole system was degassed with N₂/CO₂ over night to make sure all oxygen possibly trapped in the tubing was removed before inoculation. After approximately 16 h, WE polarisation was started and *G. sulfurreducens* mCh was harvested. Medium in the WE reservoir was supplemented with 5 to 10 mM Na₂-fumarate as electron acceptor (and 250 µg l⁻¹ spectinomycin to sustain selection pressure) before inoculation. The WE was polarised for at least 90 min and 50 ml *G. sulfurreducens* mCh culture harvested in mid exponential phase (after 24 h growth). The culture was washed once with 0.125 M phosphate buffer and inoculated to the WE reservoir with a syringe. Experiments were carried out at 30 °C. OD₆₀₀ and metabolite concentration were measured during the experiment as described in section 3.3.

3.9.4 Flow cell characterisation with EIS

In order to electrochemically characterise the modified flow cell, EIS was measured with K₄[FeCN₆] as redox probe. Therefore, 10 mM K₄[FeCN₆] in 0.5 Na₂SO₄ was pumped through the WE chamber and 0.5 Na₂SO₄ through the CE chamber (at 0.5 ml min⁻¹, at 30 °C). Potentiostatic EIS was performed at frequencies ranging from 100 kHz to 50 mHz, an amplitude of 10 mV root mean square (rms) and 10 points per decade at an OCP of +0.23 to +0.27 V vs. SHE (Standard Hydrogen Electrode). OCP was measured for 30 min.

EIS analysis was fitted with a Randles type equivalent circuit (Figure 1.8) as described already before in [165, 166]. Fitted R_{CT} values were calculated with the Gamry Echem Analyst software (Gamry Instruments, Warminster, USA) in simplex mode.

3.9.5 Biofilm characterisation with EIS

During flow cell experiments, electrochemical impedance of the biofilm-electrode-system was measured periodically at polarisation potential and with the same parameters as described in section 3.9.4 above but without an additional redox probe. As impedance was measured automatically by the potentiostat, the peristaltic pump was not stopped for measurements. Intervals between the measurements varied and are stated individually in the Results section, applied potential is also stated with the results (section 4.7.2 and section 4.7.3).

3.9.6 EIS of LbL-coated electrodes

A stable set-up of the three electrode system is beneficial for unobstructed EIS, therefore impedance of LbL-coated electrodes was assessed in the flow cell setup. Analysis was conducted in 0.075 M phosphate buffer with 10 mM K₄[Fe(CN)₆] as redox probe in the WE reservoir. An ITO electrode was mounted to the flow cell, sealed with silicone and the system degassed with N₂. Subsequently, EIS of the non-coated electrode was measured at the open circuit potential (between +0.2 und +0.25 V vs. SHE).

Afterwards, the flow cell was detached from all tubings, the chamber unscrewed and membrane and RE stored in ddH₂O, respectively KCl. Then, the WE was LbL-coated while attached to the WE chamber, i.e. without detaching it from the Pt-frame to ensure identical contacting properties for the coated and the non-coated electrode. Each 1 ml coating solution were used, with 3 x 1 ml ddH₂O wash in between the layers and in addition the whole WE chamber was rinsed with ddH₂O after the third washing step to ensure that no coating solution remained in the chamber. The flow cell was then re-assembled, connected to the tubings and filled with phosphate buffer. EIS was measured after 30 min of degassing. EIS of the coating combinations (PEI-PSS)₂, (PEI-PSS)₂-CHI and (PEI-PSS)₂-PEI-ALG was measured without changing the buffer-K₄[Fe(CN)₆] solution, (PEI-PSS)₂-PEI was measured a different day with a new solution.

3.10 Data analysis

All (statistical) data analysis was done with R, version 4.1.0 ("Camp Pontanezen") [159], with RStudio as graphical user interface (version 1.4.1717 "Juliet Rose") [167]. The R-package *ggplot2* was used to produce all plots [168].

Chapter 4

Results and Discussion

4.1 Lbl-coated GAC_{mag}

GAC_{mag} were coated to improve their properties as adhesion material for bacteria in fluidised bed reactors operated as MFC. Zeta potential of the particle surface was measured with a Zeta Sizer®. The results are shown in Figure 4.1 with measurements immediately after coating shown in light grey and zeta potential after treatment in dark grey. Treatments were incubation in H₂O or in 0.125 M phosphate buffer to examine the effect of high salinity on the coating. Incubation in ddH₂O served as negative control. Analysed was the absolute charge, as well as the change in zeta potential of coated particles with respect to non-coated GAC_{mag}. Thereby, a negative zeta potential indicated that the particle carried a net negative charge and a net positive charge if the zeta potential was positive. Figure 4.1 shows means with SD of technical triplicates of zeta potential analysis. Results are also summarised in Table 4.1. Coating compositions were PEI, PEI-PSS, PEI-PSS-CHI and PEI-PSS-PEI.

ALG and PSS as final layer resulted in a negative zeta potential (-11.0 ± 52.6 mV, respectively -28.8 ± 9.9 mV), while the cationic polyelectrolytes CHI and PEI led to a positive surface potential (43.5 ± 9.9 mV, respectively 36.8 ± 7.1 mV). These net charges were expected, considering the chemical structure of the polyelectrolytes (shown in Figure 1.7): ALG and PSS are polyanions, CHI and PEI polycations. In detail, CHI resulted in a stronger positive charge than PEI and PSS in a stronger negative charge than ALG. Non-coated particles also showed a negative surface potential, which can be explained by the surface chemistry of GAC that is dominated by negatively charged carboxy-groups [169].

SD was between 19 and 32 % for PSS, CHI and PEI as the final layer, while ALG on the surface resulted in a high SD of over 400 %. Large deviation in the zeta potential analysis indicates that the particles as collective do not behave uniformly in the electric field so that no adequate zeta potential can be determined. Aggregation of the particles during ALG-coating and thereby high differences in particle size might also be an explanation. The determined absolute charge for particles with ALG as final layer is therefore erroneous.

Incubation in ddH₂O did not change the surface potential significantly, only for CHI as final layer the zeta potential was reduced after ddH₂O incubation. In contrast, when analysing the interaction of coated particles with buffer salts, it showed that for all coatings the surface potential became more negative when incubating the particles in phosphate buffer for 18 h. This indicates that the positively charged surfaces were possibly shielded by anions from the buffer and that anions might also adhere to the already negatively charged surfaces, even though that should not be possible due to electrostatic repulsion. Instead, it would have been expected that negatively coated surfaces attracted cations present in the buffer. The increase in

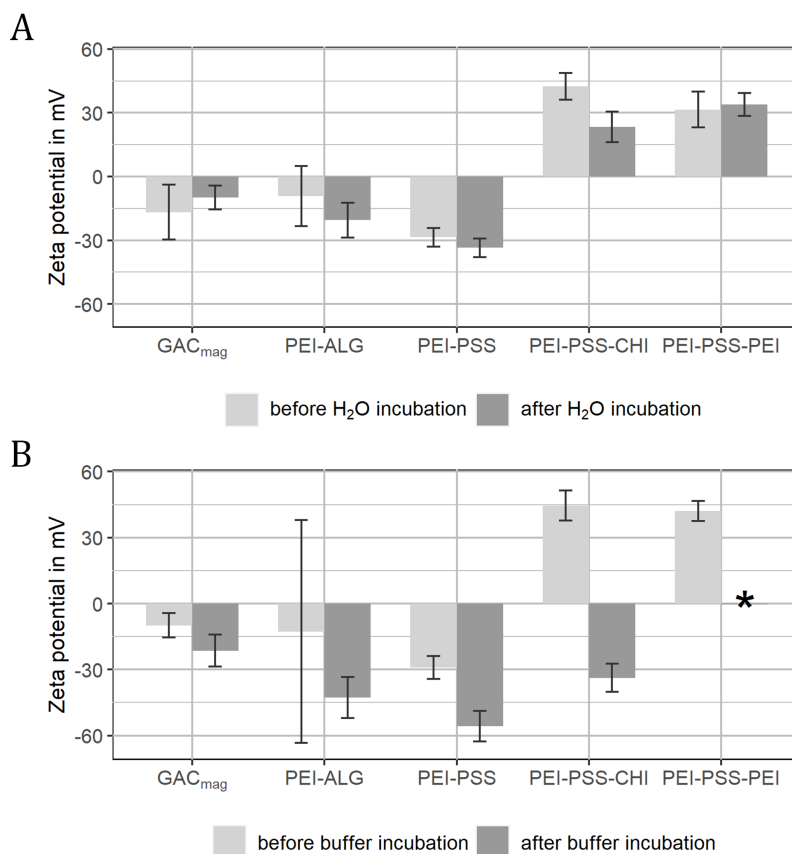


FIGURE 4.1: Zeta potential analysis of differently coated particles and non-coated GAC_{mag}. Results immediately after coating are shown in light grey and zeta potential after incubation in ddH₂O (A) or 0.125 M phosphate buffer (B) for 18 h in dark grey. Zeta potential of particles coated with PEI-PSS-PEI could not be determined after buffer incubation, indicated by the asterisk.

negative surface potential for ALG and PSS might be explained by anions covering areas on the particle surface where the underlying positively charged PEI-layer was not entirely covered by PSS/ALG. Since GAC particles have a large surface that is also rather rugged, it might not be covered homogeneously, leaving positively charged surface non-covered by PSS/ALG, therefore prone to adhere anions from the buffer. This might then induce a more negative charge.

Unfortunately, for PEI as the final layer, no output could be generated from the zeta potential analysis (indicated by the asterisk in Figure 4.1). Zeta potential analysis is very sensitive to high salt concentration, therefore, if some particles capture a high amount of salt and salt is released during analysis (even though particles were immersed in water after buffer incubation and prior to analysis), errors occur.

TABLE 4.1: Surface potential of coated and non-coated GAC_{mag} pre- and post ddH₂O/buffer incubation (0.125 M phosphate buffer) is shown as mean zeta potential of technical triplicates \pm SD (absolute values). For non-treated particles SD shows the error propagation of the technical triplicate and two particles sets coated in different experiments. For PEI-PSS-PEI coated particles post buffer incubation no zeta potential could be determined.

Coating	Mean zeta potential \pm SD in mV		
	Treatment	ddH ₂ O	Buffer
GAC_{mag}	-13.3 \pm 13.7	-9.9 \pm 5.5	-21.4 \pm 7.3
PEI-ALG	-11.0 \pm 52.6	-20.5 \pm 8.2	-42.7 \pm 9.4
PEI-PSS	-28.8 \pm 9.3	-33.5 \pm 4.4	-29.0 \pm 5.2
PEI-PSS-CHI	43.5 \pm 9.9	23.4 \pm 7.3	-33.8 \pm 6.4
PEI-PSS-PEI	36.8 \pm 7.1	33.9 \pm 5.4	-

4.2 Lbl-coated planar electrodes

Planar electrodes for the use in electrochemical H-cells were LbL-coated in addition to the magnetic particles described in the previous section. As a proof of principle graphite electrodes were coated first, due to their frequent use in MFC research. A larger variety of coatings was subsequently tested on ITO electrodes as well.

4.2.1 Graphite electrodes

With the HR-SKP, surface potential of planar surfaces can be determined in contrast to the Zetasizer® that analyses electrophoretic mobility of particles. By dividing a graphite electrode into three sections using silicone, different surface properties could be generated: non-coated graphite, (PEI-PSS)₂-PEI and PEI₁. Data can be presented either as heat map or as histogram. The 2 mm \times 22 mm scan of the HR-SKP as heat map illustration is shown in Figure 4.2 with the highest potential for the non-coated part in black and the lowest surface potential for (PEI-PSS)₂-PEI, shown in light grey. For quantitative comparison of surface potential, data were split according to the potential abundance, shown as histogram plot in Figure 4.3. By manual splitting of the histograms according to the occurring peaks, median and SD of surface potential were extracted for each coating. Since the data were not normally distributed the median is given instead of the mean. Results are shown in Table 4.2. The graphite electrode had a surface potential of 0.57 ± 0.01 V vs. SHE, one layer of PEI produced a surface potential of 0.36 ± 0.02 V vs. SHE and (PEI-PSS)₂-PEI with five layers of polymer coating resulted in 0.28 ± 0.01 V vs. SHE. This showed that a) the coating method is applicable to planar graphite electrodes since the surface potential is significantly different between non-coated graphite and LbL-coated sections, and b) that the difference in surface potential between graphite and coated sections increases with the number of layers coated.

Buffer incubation of coated graphite electrodes

Analogous to incubation of coated particles, coated graphite electrodes were incubated in saline medium to test coating integrity and surface potential (phosphate-buffered *G. sulfurreducens* medium was used in this case). Surface potential of a partly

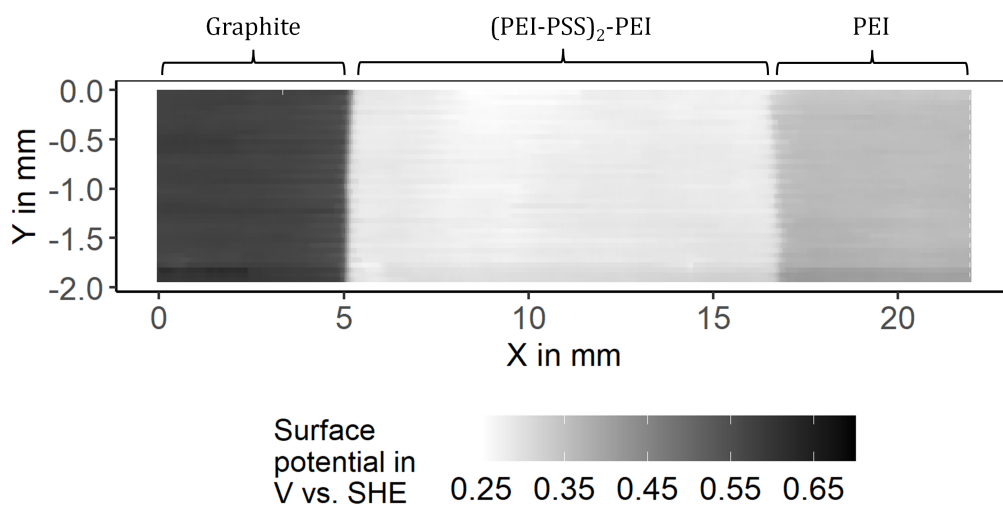


FIGURE 4.2: A graphite electrode was divided in three sections with silicone and the resulting surface characteristics analysed with the HR-SKP. Data are shown as heat map with the highest potential in black and the lowest in light grey. The non-coated graphite surface is to the left, the mid section was coated with (PEI-PSS)₂-PEI and the right section with one layer PEI.

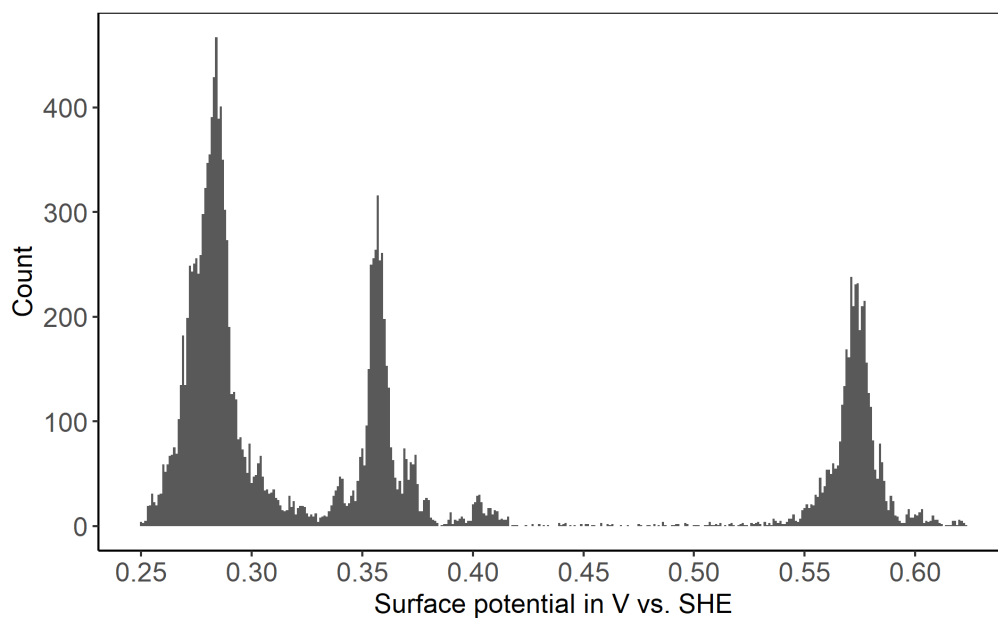


FIGURE 4.3: A graphite electrode was divided in three sections with silicone and the resulting surface characteristics analysed with the HR-SKP. Data are shown as histogram. Quantitative comparison of surface potential of the sections was achieved by splitting the histogram according to the peaks and calculating median and SD for each coating, accordingly. See Table 4.2.

TABLE 4.2: Surface potential of a planar graphite electrode with a non-coated section, a section coated with (PEI-PSS)₂-PEI and one with only PEI₁ (in V vs. SHE). The median surface potential of the area analysed with the HR-SKP is given with the SD of surface potential in the respective area. Data from the respective areas were manually split according to the peaks in the histogram. An illustration of the data is also shown in Figure 4.2 and 4.3.

Surface	Median surface potential in V vs. SHE \pm SD
Non-coated graphite	0.57 ± 0.01
(PEI-PSS) ₂ -PEI	0.28 ± 0.01
PEI ₁	0.36 ± 0.02

coated graphite electrode (half graphite, half (PEI-PSS)₂-PEI) was analysed prior to incubation in *G. sulfurreducens* medium and immediately after 64 h incubation. In Figure 4.4 HR-SKP data are shown before (top) and after (bottom) incubation. As observed for buffer incubation of the particles, surface potential of the positively charged LbL-coat changed in interaction with salt medium. Prior to incubation, surface potential was $0.33 \text{ V} \pm 0.03$ vs. SHE and changed to $0.55 \text{ V} \pm 0.02$ vs. SHE after 64 h. In the meantime, surface potential of the non-coated graphite increased only by 0.04 V.

As seen for particle incubation, either anions from the medium adhere to PEI or the coating was partly detached during the incubation process. Both effects would have similar symptoms, as surface potential converges to graphite surface potential in both cases.

The uncertainty in these results has its source in the fact that for both methods of analysis the surface potential cannot be measured in the actual medium but is measured in ddH₂O in the Zeta sizer® or at the polymer-air interface in the HR-SKP. This problem should have been circumvented by the incubation of coated material in buffer, but as described, also this tactics could not describe the effect of medium-coating interaction entirely.

For planar electrodes some alternatives exist as alternative to the HR-SKP: X-ray photoelectron spectroscopy (XPS) [170], Raman microscopy [171] and quartz chrystal microbalance (QCM) [172]. The first two are based on the chemical identification of certain atoms or functional groups on the modified surface in order to prove the presence of the adsorbed layers. QCM instead detects layer deposition via reduced oscillation of the quartz crystal which also allows analysis of film hydration in liquid, i.e. layer swelling and interaction with medium salts which is not possible with the aforementioned methods. However, the surface potential, which is the actual interest of the modified surface, can only be resolved with the HR-SKP. Additionally, the coating can be measured on the actual electrode material in contrast to the QCM where the quartz crystal has to be coated. There are few instruments specialised on measuring zeta potential of planar surfaces using titration and thereby allowing the determination of the isoelectrical point at different pH but also only in solutions with low osmolarity which does not solve the apparent problem entirely (e.g. SurPASS 3 by Anton Parr Germany GmbH; [173]).

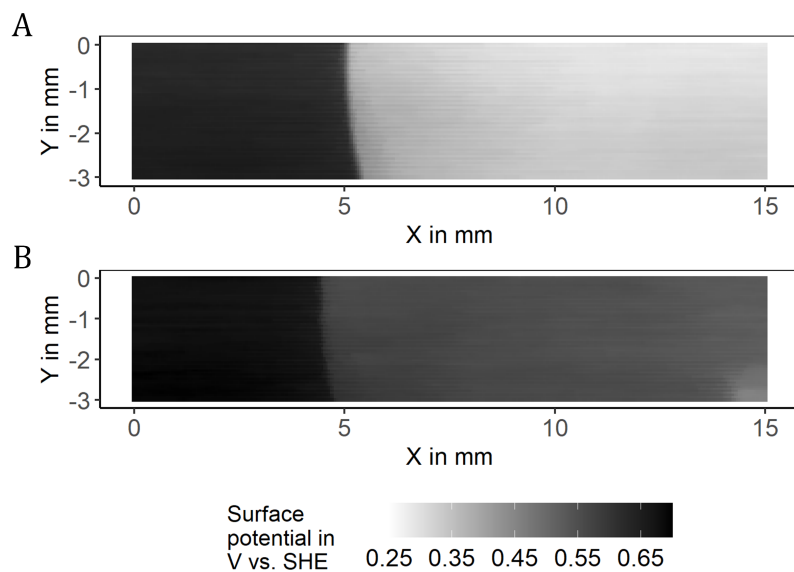


FIGURE 4.4: A (PEI-PSS)₂-PEI coated graphite electrode is shown before (A) and after (B) incubation in *G. sulfurreducens* medium for 64 h. Surface potential of the (PEI-PSS)₂-PEI coat changes from $0.33 \text{ V} \pm 0.03$ to $0.55 \text{ V} \pm 0.02$ vs. SHE.

4.2.2 Coated ITO-electrodes

Bacterial interaction with the electrode is a combination of available surface and surface chemistry. To minimise the effect of available surface and emphasise the impact of electrode surface chemistry on MFC performance, graphite electrodes were polished with SiC grinding paper. However, unevenly polished electrodes might still influence experiments non-reproducibly. Therefore, ITO-coated glass slides with almost no 3D-structure were applied as electrode additionally and coating experiments were performed, accordingly. Electrode preparation with cavities to test different coatings on one electrode is shown in Figure 3.4 B in the Methods section (section 3.7.4). The following coatings were applied: (PEI-PSS)₂ (*PSS-* in the following), (PEI-PSS)₂-CHI (*CHI+*), (PEI-PSS)₂-PEI-ALG (*ALG-*) and (PEI-PSS)₂-PEI (*PEI+*). The resulting surface potential pattern is shown in Figure 4.5, with potential from low to high in a colour gradient from white to black. The surface projection shows uniform surface potential, i.e. surface coverage, for all coatings, which illustrates that the chosen number of polymers for the coating is sufficient to cover the underlying ITO. Quantitative comparison was done, as for coated graphite, by splitting the sections according to the peaks in the histogram. From this point median and SD were calculated (Table 4.3). In the particular order, *PSS-* induced the highest surface potential (0.71 V vs. SHE), showing a higher potential as non-coated ITO (0.60 V vs. SHE), together with *ALG-* (0.66 V vs. SHE). For *CHI+* the potential was similar to ITO potential (0.57 V vs. SHE), while *PEI+* led to a significantly lower potential compared to non-coated ITO (0.34 V vs. SHE).

Those results are consistent with zeta potential analysis of coated GAC_{mag} , except for the obtained result for *CHI+* potential. PEI-PSS-CHI coated particles had a more positive surface potential than PEI-PSS-PEI while for the coated ITO surface this trend was reversed. Those experiments are not entirely comparable though since GAC_{mag} were coated with three polymer layers overall and ITO with five. When the data

shown in Figure 4.2 are taken into consideration it can be observed that an increase in number of layers decreases the surface potential for the cationic polymer (towards more positive surface charge). Taking this into account, one could conclude that the effect of the higher number of layers had a greater influence on coatings with PEI as the final layer and that this is the reason why *PEI+* showed a lower surface potential than *CHI+*.

Generally, considering the hypothesis that a more positive surface potential influences bacterial adhesion to the electrode positively, similar MFC performance is expected for *PSS-*, *ALG-* and *CHI+*, while the performance of LbL-coated electrodes with *PEI+* should be significantly different.

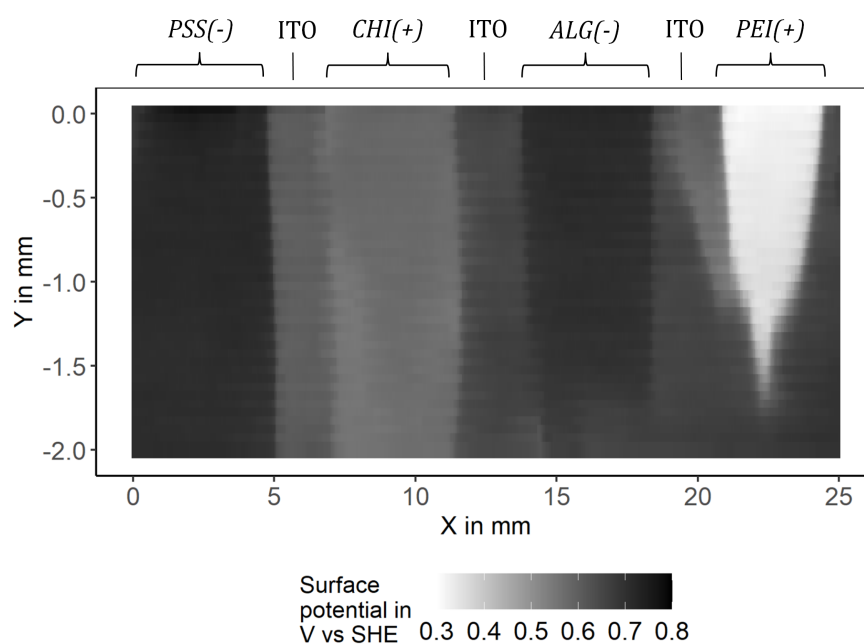


FIGURE 4.5: Four cavities were marked with silicone on an ITO electrode and LbL-coated with *PSS-*, *CHI+*, *ALG-* and *PEI+*. Surface potential was measured with the HR-SKP and is displayed in a colour gradient from white to black, corresponding to 0.3 V in white to 0.8 V in black.

TABLE 4.3: Surface potential of non-coated ITO and ITO coated with *PSS-*, *CHI+*, *ALG-* and *PEI+*, analysed with the HR-SKP. Data are given as median \pm SD of the respective sections marked on the electrode.

Surface	Median surface potential \pm SD in V vs. SHE
Non-coated ITO	0.60 ± 0.01
(PEI-PSS) ₂	0.71 ± 0.01
(PEI-PSS) ₂ -PEI-ALG	0.66 ± 0.01
(PEI-PSS) ₂ -CHI	0.57 ± 0.01
(PEI-PSS) ₂ -PEI	0.34 ± 0.01

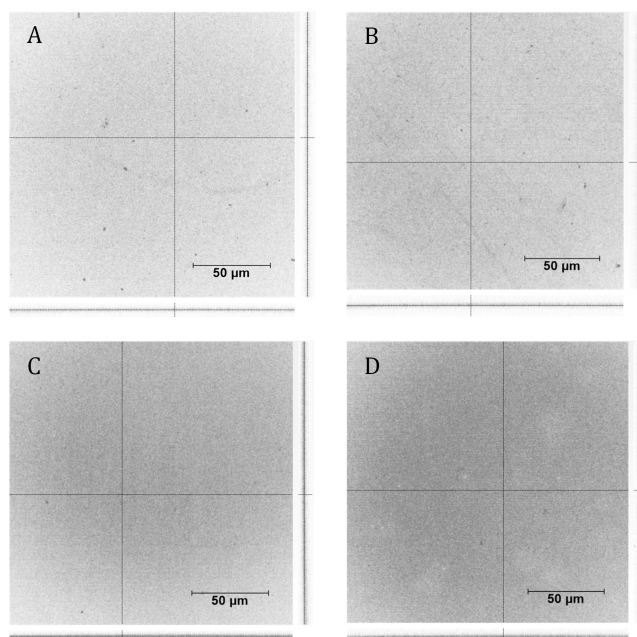


FIGURE 4.6: $(\text{PEI}^{\text{R}}\text{-PSS})_2\text{-PEI}^{\text{R}}$ and $(\text{PSS}^{\text{R}}\text{-PEI})_2\text{-PSS}^{\text{R}}$ electrodes were imaged with the CLSM after polarisation at 0.1 V vs. SHE for 111 h. Representative images show the xy-view, with xz-scans to either sides and reveal evenly coated electrodes.

ITO electrodes with fluorescent polymers

Buffer incubation of coated graphite electrodes showed an increase in surface potential when analysed with the HR-SKP. The surface potential could have changed due to anions adhering to the positively charged PEI-layer or the incubation period could have led to detachment of polymer layers. To distinguish between those phenomena, ITO electrodes were coated with fluorescently labelled polyelectrolytes to assess layer integrity with the CLSM after treatment. To simulate conditions during an MFC experiment as realistic as possible, coated electrodes were mounted to an H-cell, polarised to +0.1 V vs. SHE and samples taken from the WE chamber to analyse fluorescence of the supernatant, additionally. In case larger amounts of fluorescent polymer detached during the experiment, it should be detectable with a microplate reader. Both, PSS-Rho and PEI-Rho (PSS^{R} and PEI^{R} in the following) were used as the basal coating layer to analyse which one was more stable during electrode polarisation. The coating combinations $(\text{PEI}^{\text{R}}\text{-PSS})_2\text{-PEI}^{\text{R}}$ and $(\text{PSS}^{\text{R}}\text{-PEI})_2\text{-PSS}^{\text{R}}$ were used.

The lower detection limit of Rho-labelled polyelectrolytes in the microplate reader was identified as 1 mg l^{-1} in advance (data shown in the Appendix in A.1). Samples were taken from the WE chamber of both H-cells after 22 h, 86 h and 111 h and fluorescence analysed immediately after sampling. Data from fluorescence analyses are shown in the Appendix in Figure A.2. No fluorescence was detected for all time points in both H-cells. Considering the detection limit for the detection of the fluorescent polyelectrolytes in the microplate reader, this means that the concentration of free polymer in the medium was at least lower than 1 mg l^{-1} . However, this

analysis might not be sufficiently sensitive as the amount of polymer deposited on the electrode is very low from the beginning.

The experiment was aborted after 111 h and both electrodes were analysed with the CLSM. The comparison of images before and after the H-cell experiment is shown in Figure 4.6. Imaging parameters were identical for pre- and post-imaging. Qualitative evaluation showed increased fluorescence intensity for PSS^R as basal layer. Fluorescence for (PEI^R-PSS)₂-PEI^R was lower overall, but also did not change significantly over the course of the experiment. xz-scans imply that the surface was very evenly coated; with some minor aggregations in the PEI^R coating. The increase in fluorescence for PSS^R fluorescence could be caused by reorganisation of the polymer-layers during the experiment (salt/water deposition in between the layers, also water extrusion from in between the layers might be possible), but that remains speculative.

Nevertheless, CLSM analysis showed that the coating was stable under MFC conditions. For further coatings PEI was chosen as the basal layer since it showed the largest potential difference to ITO (see Table 4.3), which should be most beneficial for LbL-coating.

4.2.3 EIS of coated electrodes

To evaluate how the coatings affect the electrochemical properties of the anode, EIS of the electrodes was analysed before and after the respective coating, employing K₄[Fe(CN)₆] as redox probe. The corresponding Bode and Nyquist plots are presented in Figure 4.7 and 4.8 and show a typical Randles-like pattern with R_{CT} as charge transfer resistance for the redox reaction Fe(II) ⇌ Fe(III) [149]. For PSS- and CHI+ the half-circles in Nyquist presentation are smaller compared to the bare electrode, indicating rather a decrease of charge transfer resistance than an electrical insulation by the coating. For ALG- and PEI+ the impedance was increased compared to the bare electrode, indicating a higher R_{CT} for the Fe(II) ⇌ Fe(III) redox reaction (while solution resistance R_U was constant at ≈ 14 Ω). Accordingly, good MFC performance was expected, at least for the coatings PSS- and CHI+. Furthermore, inserts in Nyquist plots focussing on the high frequency/low ohmic resistance area (the point of x-axis pass-through) indicate almost identical ohmic resistance of the uncoated and in-place coated electrodes, leading to the assumption that the overall ohmic resistance of the electrodes was not increased by surface modification. It can be assumed that the LbL-surface coatings did not insulate the electrode surface. Numerical comparison of the impedance data between the respective coatings was not done, since the individual EIS analysis of the bare ITO electrodes already differed without coating. Therefore, comparison was only conducted between the bare and in-place-coated electrode (pre- and post-coating).

The in-place coating method in the flow cell used for EIS analysis (and electrode coating for the use in H-cells) ensured that electrical contacting was identical for coated and non-coated ITO. The deviation that was now visible among the non-coated ITO electrodes might be a combined effect of slightly different electrical contact between ITO and the Pt-frame for each EIS experiment and deviations in the manufactured ITO-coatings on the glass slides. Aside from this effect EIS analysis showed that electrochemical properties were not influenced adversely, especially not for coatings PSS- and CHI+.

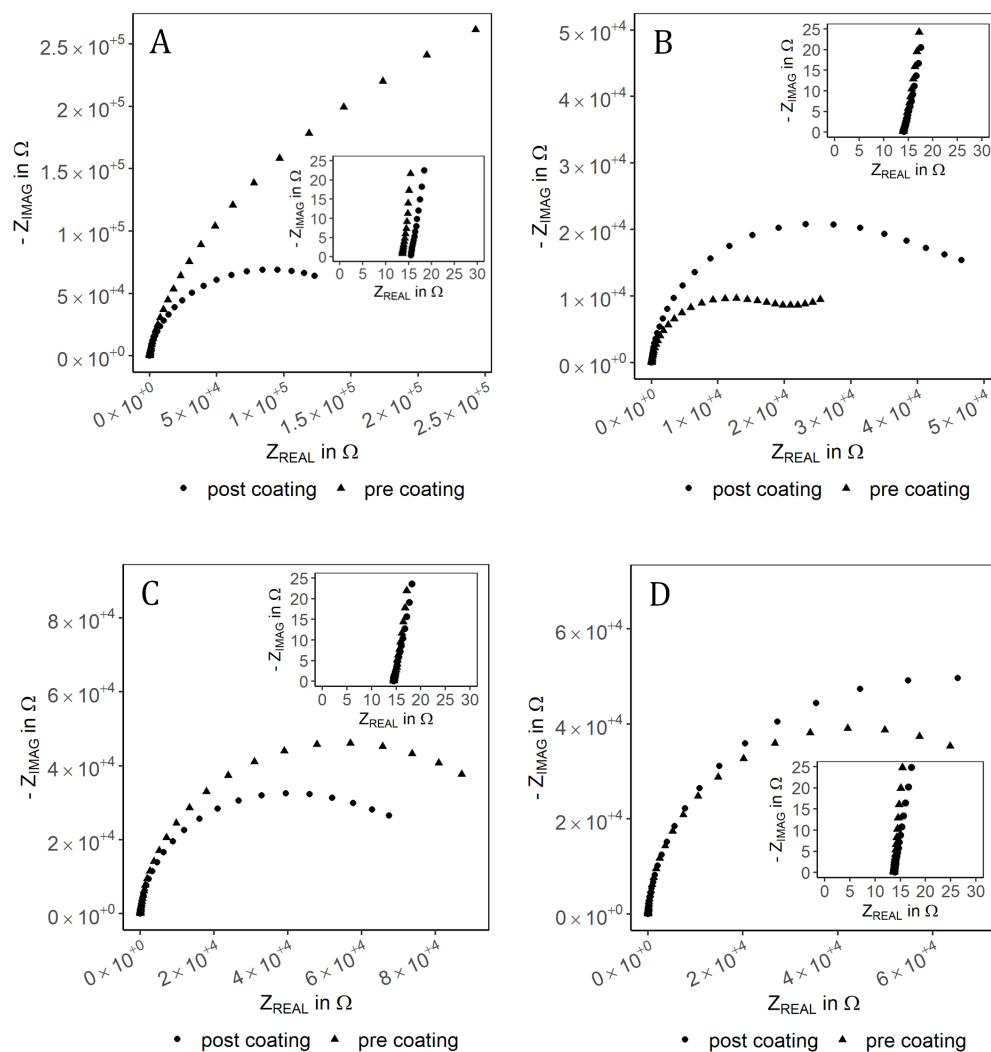


FIGURE 4.7: Nyquist representation of impedance pre and post-coating is shown for all coatings. A: PSS-, B: ALG-, C: CHI+, D: PEI+. Note the different scales on axes. One measurement was performed for each surface modification. The inserts show a close up of the high frequency / low ohmic resistance range. Analysis was performed in 75 mM anoxic phosphate buffer with 10 mM $\text{K}_4[\text{Fe}(\text{CN})_6]$ as redox probe in the WE reservoir at a potential of +0.2 V vs. SHE.

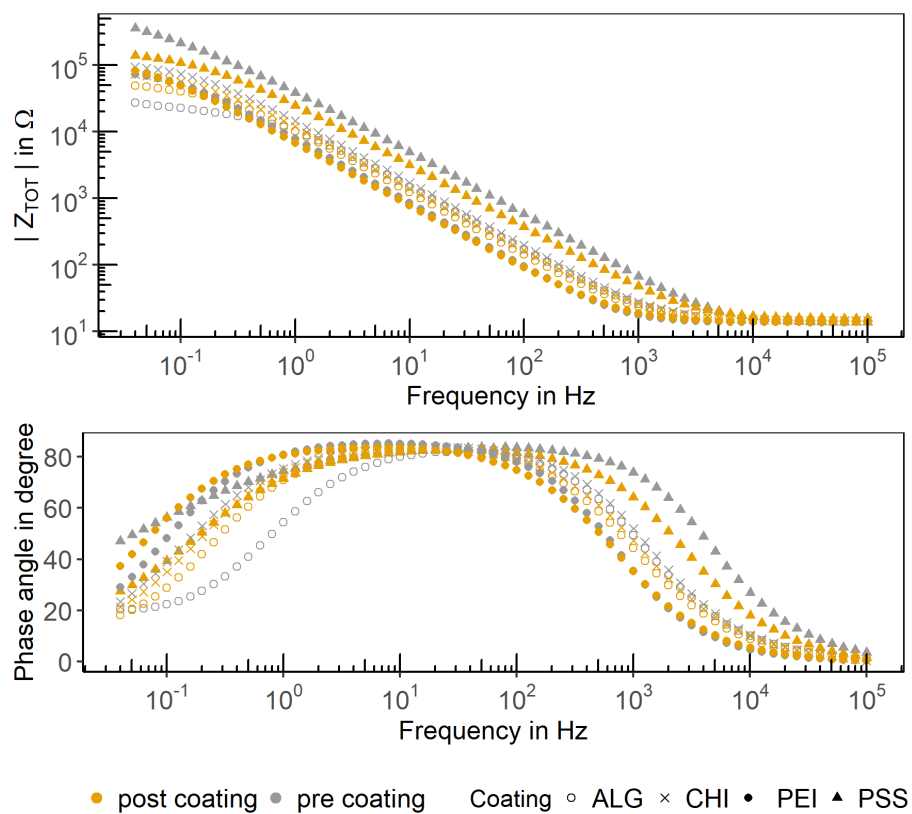


FIGURE 4.8: Bode representation of EIS measurement of coated and non-coated electrodes. Impedance of electrodes pre-coating is shown in grey, post-coating in orange. One measurement was performed for each surface modification. Analysis was performed in 75 mM anoxic phosphate buffer with 10 mM $K_4[Fe(CN)_6]$ as redox probe in the WE reservoir at a potential of +0.2 vs. SHE.

4.3 Adhesion of *G. sulfurreducens* to GAC_{mag}

Due to its large available surface area the GAC_{mag} was expected to bind planktonic *G. sulfurreducens* cells from the medium and the experiment aimed to further improve cellular adhesion by modifying the physico-chemical surface properties of the particles with LbL coating. To test the effect of surface charge and number of coated layers, a negatively and a positively charged surface were generated with the coatings (PEI-PSS)₂ (PSS₄ in the following) and PEI-PSS-PEI (PEI₃ in the following), as well as a positively charged surface constituted of a high number of layers: (PEI-PSS)₁₅-PEI (PEI₁₅). The magnetic properties of the particles were used to facilitate quantitative analysis of cellular adhesion as the particles could easily be separated from cells with a magnet in order to analyse OD₆₀₀.

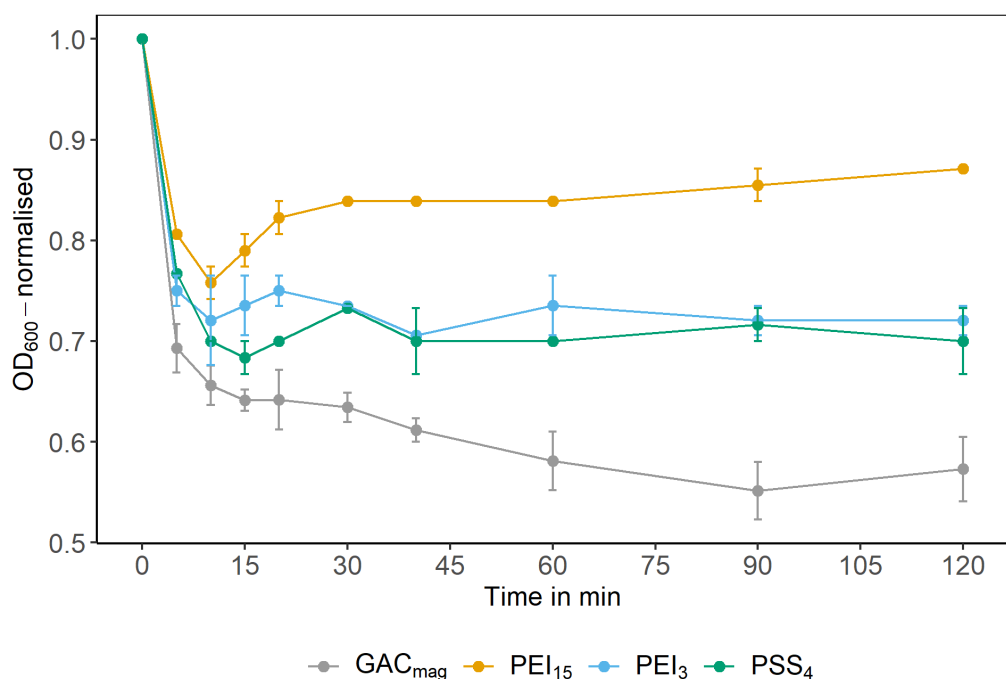


FIGURE 4.9: Decrease of OD₆₀₀ in supernatant was analysed to quantify adhesion of *G. sulfurreducens* to (coated) GAC_{mag} . The legend indicates the layer number and the final layer. Shown is the mean of biological duplicates for coated particles and of $n = 4$ for GAC_{mag} . Error bars show the deviation of the mean.

In Figure 4.9 the decrease in OD₆₀₀ in the supernatant is shown over time. Coated particles were analysed in duplicate, $n = 4$ for non-coated GAC_{mag} . Error bars show the error of the mean. For all experiments the OD₆₀₀ decreased rapidly within the first 10 min, although to a different extent. The reduction until this time point was 24 % for PEI₁₅, 28 % for PEI₃, 30 % for PSS₄ and 34 % for GAC_{mag} . For all coated particles OD₆₀₀ slightly increased after the maximum OD₆₀₀ reduction until it remained stable to the end of the experiment after 2 h incubation. No increase after 10 min incubation could be observed for non-coated GAC_{mag} but further decrease after 30 min. The overall reduction in OD₆₀₀ was 43 % for GAC_{mag} , 30 % for PSS₄, 28 % for PEI₃ and 13 % for PEI₁₅. The OD₆₀₀ of the control that contained cells in medium without

GAC_{mag} remained constant throughout the whole experiment (data not shown in Figure 4.9). Therefore, cell lysis as a reason for OD_{600} reduction could be neglected.

Bacterial adhesion to the non-coated GAC_{mag} followed an isothermal adsorptive behaviour as described for dye adsorption to activated carbon particles in [174] while a lesser and no continuous adsorption to GAC_{mag} was detected when the particles were coated. The adhesion kinetics suggest that the LbL-coat decreased the GAC surface available for adhesion as the decrease in OD_{600} was the largest for non-coated GAC_{mag} and smallest for GAC_{mag} with 15 layers of coating. The charge of the coating played no major role as PEI with positive zeta potential and PSS with negative zeta potential as terminal layer led to comparable OD_{600} reduction. Even though LbL coating deposits only nanometer thin layers on the GAC_{mag} it apparently decreased the available surface for bacterial adhesion, probably by clogging pores on GAC_{mag} particles and thereby decreasing the available surface. In the shown experiment this effect intensified the more layers were applied, which additionally led to detachment of cells back into the medium. To confirm this, the geometrical surface of GAC_{mag} coated with a different number of layers should be determined in further experiments.

Given the described results, LbL-coating was found no suitable method to improve the chemical surface properties of GAC_{mag} in terms of being attractive for bacterial adhesion. Alternative modification methods that will not clog pores are chemical methods like oxidation with nitric acid (for enhancement of carboxy-groups on the surface [175]) or thermal treatment with ammonia (for basic nitrogen functionalities [176]) and could be considered in order to alter the surface charge without influencing available surface area.

In general, robust quantification of adhered biomass to particles was challenging. Analysing the reduction of OD_{600} in the supernatant is an indirect method and relies on efficient separation of bacteria-loaded particles from planktonic cell suspension. The method used in this work was based on the work in [177] in which the adhesion of *S. oneidensis* to activated carbon fabric was evaluated. A similar method was used in [178] and [179] where a defined volume from the supernatant was plated and thereby colony forming units not bound to GAC could be calculated. For quantification of bacterial biomass in GAC-based (drinking) water filters another method was developed that determines ATP-concentration in the bacteria-GAC sample [180]. From analysed ATP-concentrations in calibration samples, the number of cells present on the GAC samples was calculated. The challenge with this method is that the included luminescence measurement is very time-sensitive, i.e. results can differ greatly if the timing is not absolutely identical for all samples. That makes it especially difficult to analyse adhesion isotherms, also considering the sampling procedure from the anaerobic septum flasks. Therefore, the method was not found suitable for a screening-like approach as it was planned with the coated GAC_{mag} .

4.4 MFC in H-cells on graphite electrodes as a benchmark

MFC on graphite electrodes in membrane separated H-cells can be considered the laboratory standard for *G. sulfurreducens* MFC [11]. Therefore, this system was used to create benchmark values for later comparison with LbL-modified electrodes. The parameters maximum current density, start-up time (time till current density exceeded $10 \mu A cm^{-2}$), time until the maximum current density was reached, biofilm thickness and coulombic efficiency η_C were considered for evaluation of the system. In order to analyse if, respectively which impact different potentiostat brands/systems have on

experimental reproducibility and the aforementioned parameters, potentiostats from PalmSens (MultiEmStat3+; Houten, Netherlands), MaterialMates (Multimaster 2.1; Milano, Italy) and Gamry (Reference600; Gamry Instruments, Warminster, PA) were tested. The applied potential was +0.6 V vs. SHE.

Current density over time of 14 *G. sulfurreducens* MFC experiments on non-coated graphite electrodes with different potentiostats is shown in Figure 4.10. Common is the sigmoid shape of the current density curves: the start-up phase is followed by an exponential increase in current density, resulting in a distinct maximum before a plateau phase. But except for the uniform curve shape, the outcome of the potentiostat test was heterogeneous for all performance indicators. Summarised results are shown in Table 4.4 in row *All*. Over the course of 14 experiments the maximum current density was $350 \mu\text{A cm}^{-2} \pm 19\%$, with a start-up time of $23.9 \text{ h} \pm 28\%$ and the maximum current production was reached after $69.8 \text{ h} \pm 15\%$. Biofilm thickness with $40 \mu\text{m} \pm 44\%$ was measured for 6 of 14 experiments and η_C was calculated with $62\% \pm 17\%$ for 9 experiments. Overall, SD was high for all performance indicators but with 15% lowest for the time of maximum current. Noticeable is the absolutely high SD for the start-up time and for the biofilm thickness.

To assess scattering individually for the different potentiostats, mean and SD for each performance indicator were calculated separately for the used potentiostats. SD for experiments with the MaterialMates potentiostat and the PalmSens potentiostat neither differed significantly from each other nor from the SD when all experiments are treated as one pool (considering the first three parameters in Table 4.4). It seems that both potentiostat systems contributed equally to the overall SD, so there is no indication to prefer one system over the other. The Gamry single potentiostat finally produced a result very representative for all previously conducted experiments and with high signal integrity (compared to the signal noise caused by the MaterialMates potentiostat).

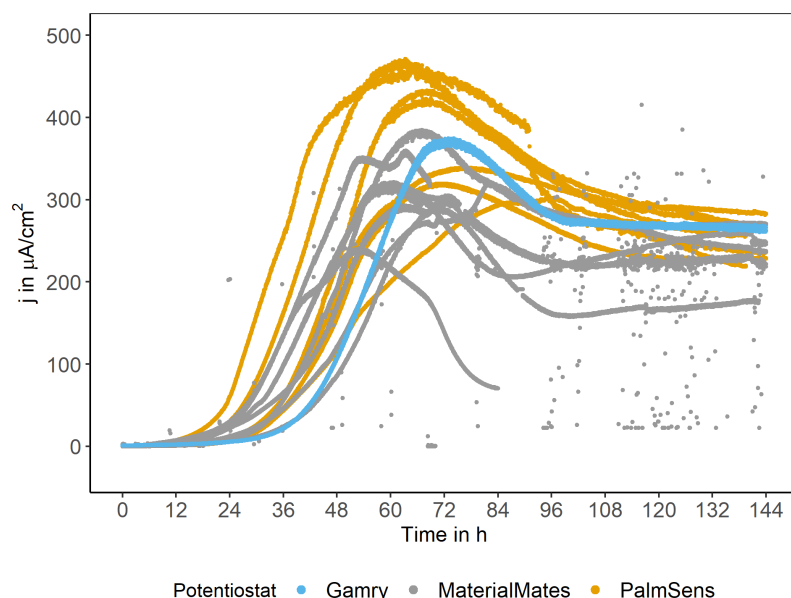


FIGURE 4.10: Current density over time of 14 *G. sulfurreducens* MFC experiments on non-coated graphite electrodes. The grey dots were caused by signal noise in experiments with the MaterialMates potentiostat.

TABLE 4.4: Mean and SD of maximum current density, start-up time, time until maximum current production was reached, biofilm thickness and η_C for MFC on graphite electrodes at +0.6 V vs. SHE applied. n = 14 for the first three parameters shown, n = 6 for biofilm thickness, n = 9 for η_C . For values marked with * n=1.

Potentiostat	Max j in $\mu\text{A cm}^{-2}$	Start-up time in h	Time to max current in h	Biofilm thickness in μm	η_C in %
All	$350 \pm 19\%$	$23.9 \pm 28\%$	$69.8 \pm 15\%$	$36 \pm 44\%$	62 ± 17
PalmSens	$388 \pm 19\%$	$26.0 \pm 29\%$	$73.8 \pm 15\%$	-	66 ± 21
MM	$315 \pm 15\%$	$21 \pm 25\%$	$65.7 \pm 13\%$	$36 \pm 42\%$	52 ± 14
Gamry	375*	30.0*	74.2*	$37 \pm 14\%$ *	-

In general, the H-cell as BES is a reactor in which multiple components are potentially variable and have influence on performance indicators. Crucial components/properties are especially: the RE, the distance between luggin capillary and WE, the distance between CE and WE, and the potentiostat. To set a constant potential the distance between WE and RE must be constant for constant electrolyte resistance. Therefore, the graphite plate used as WE was flanged onto the WE chamber in this reactor instead of inserting an electrode through the lid of the WE chamber (see Figure 3.1). Attachment via a flange also helps keeping the distance between WE and CE constant, however the CE has some leeway due to its insertion through the CE chamber lid via a rubber septum. The H-cell was optimised for the requirements of this work but reproducibility remained a constant issue.

In Table 4.5 maximum current values from representative *G. sulfurreducens* studies are noted that also used two-chambered reactors (like H-cells) with similar reaction conditions (10 mM acetate as electron donor, graphite anodes, poised potential around +0.6 V vs. SHE). Unfortunately, no performance indicators other than maximum current density are usually stated with pure culture *G. sulfurreducens* MFC. Yet, it can be concluded that $350 \mu\text{A cm}^{-2}$ produced in this work are a higher maximum current density than reported for most other pure culture *G. sulfurreducens* MFC (under the given conditions). Reproducibility is also only scarcely touched upon in any work. Kipf et al. used a setup in a modified desiccator that fitted six anodes at once and reached over $700 \mu\text{A cm}^{-2}$ with an SD of only 2% [99]. Even though these experiments were no true biological replicates they still allow to test different electrode materials (or coatings) with a lot less variability in reactor conditions compared to using six individual H-cells.

To improve reproducibility of the results obtained in this work WE material was changed from graphite to ITO glass with the aim to standardise the available electrode surface to a higher extent. ITO glass which was industrially coated (and not manually processed like graphite electrodes with SiC-paper) possesses almost no structural roughness on its surface (scanning electron microscopy (SEM) images of graphite and ITO shown in Figure 4.14). The change in electrode material aimed to especially decrease the deviation in the start-up phase that is the performance indicator most interesting when the aim was to improve bacterial adhesion to the electrode. The results with ITO as WE material are described in the following section.

TABLE 4.5: Max j as primary MFC performance indicator is indicated for different *G. sulfurreducens* pure culture MFC at poised potential on graphite electrodes. *For [99] n = 6 in one reactor. n = 3 for [156] (biological replicates), n = 14 in this work (biological replicates).

Max j in $\mu\text{A cm}^{-2}$	Applied potential in V vs. SHE	Biofilm thickness in μm	Study
98	+0.5	40 ± 6	[56]
114	+0.4	-	[52]
172 ± 29	+0.6	5 - 10	[156]
215	+0.5	-	[60]
350 ± 67	+0.6	36 ± 16	This work
756 ± 15	0	-	[99]

4.5 Optimum potential for MFC on ITO-electrodes

ITO coated glass slides were applied as WE in H-cells to assess whether reproducibility of extracted performance indicators could be improved by using a smoother surface.

Interestingly, *G. sulfurreducens* showed no current response when the same electrochemical conditions were applied on ITO electrodes as they were for MFC on graphite electrodes (applied potential of +0.6 V). In consequence, different potentials were tested in order to find the optimal current response on ITO WE. To reduce experimental bias as well, each reference electrode/luggin capillary combination was assigned a position in the incubation hood that remained the same for all conducted experiments and these positions were then randomised among the biological triplicates. Doing so, it should be avoided that any side effect from reference electrode or position in the incubator hood biased the bioelectrochemical system. Potentiostats from IPS (IPS Elektronik GmbH & Co KG, Münster, Germany) together with a Gamry1000 and a Gamry600 Reference potentiostat were used since the results with the multi potentiostats from PalmSens and Material Mates were not satisfactory considering reproducibility; as described in the previous chapter. The IPS potentiostats had been used successfully in earlier experiments [156].

After an experimental run time of 90 h WEs were detached and biofilms stained with LIVE/DEAD™ stain for CLSM imaging. Mean and SD for the extracted performance indicators at the applied potentials are summarised in Table 4.6. Additionally, current density over time for all biological triplicates is displayed in Figure 4.11.

Applied potentials from A-F were -0.1, 0, +0.05, +0.1, +0.2, +0.3 V vs. SHE. When -0.1 V vs. SHE were applied current density was the lowest with $244 \mu\text{A cm}^{-2} \pm 19\%$, with the lowest SD compared to all other current density curves. Maximum current density increased with increasing potentials with the highest current density of $417 \mu\text{A cm}^{-2} \pm 20\%$ for +0.3 V vs. SHE. As also seen for MFC on graphite electrodes biological triplicates implied large SD for maximum current density, ranging from 19 to 38%. Due to the high SD no significant differences in current density could be extracted for potentials 0 to +0.2 V vs. SHE. For four of six applied potentials, experiment 3 (blue curve) produced significantly less current compared to the other two experiments of the respective triplicate. Also, experiment 1 (grey curve) led to the highest current produced in four of six of the triplicates.

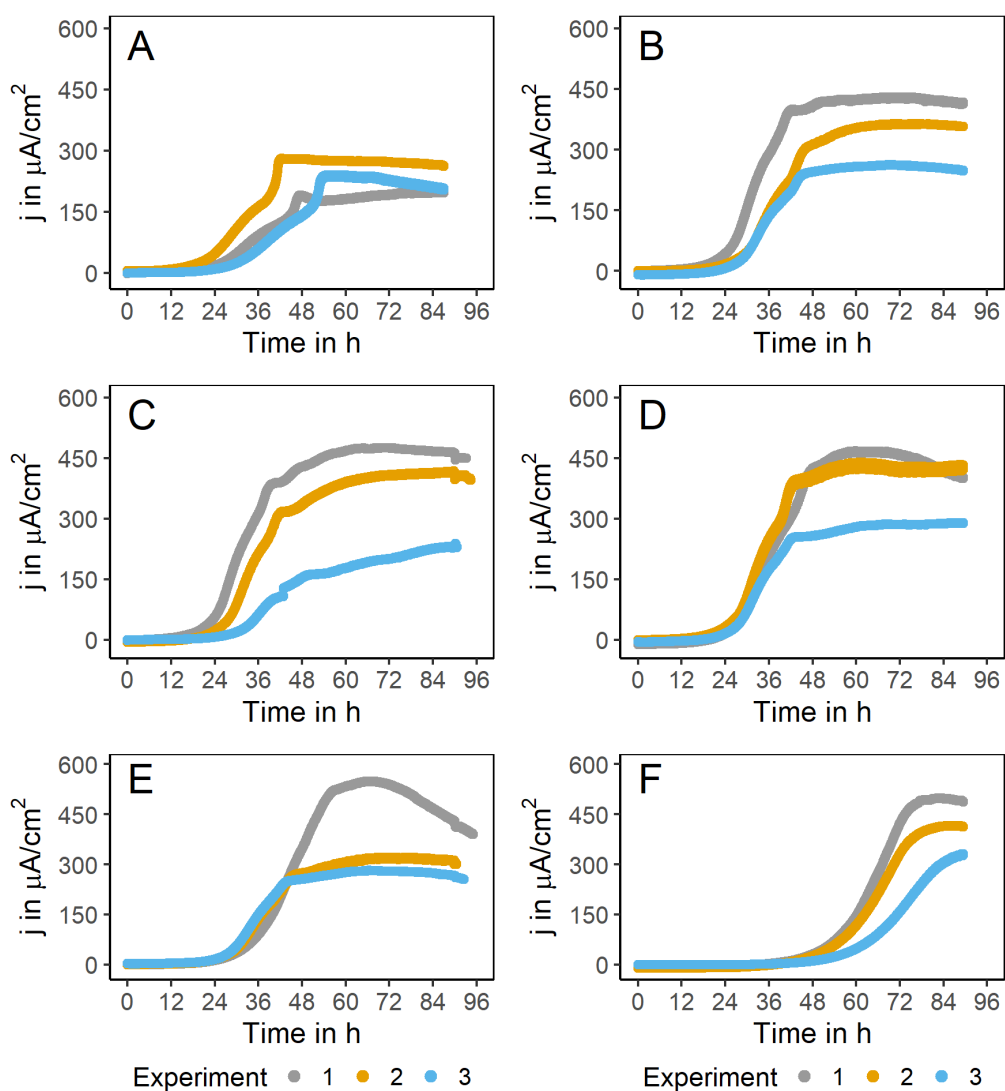


FIGURE 4.11: Current densities for *G. sulfurreducens* MFC on ITO with different applied potentials are shown. Potentials were, from A to F: -0.1, 0, +0.05, +0.1, +0.2, +0.3 V vs. SHE. The coloured lines are biological triplicates carried out in different weeks, on different positions in the incubator hood and each with different potentiostat channel.

TABLE 4.6: Current density, start-up time, biofilm thickness and η_C for different potentials applied in MFC on ITO electrodes. Indicated are mean values \pm SD. Potentials are given in V vs. SHE, with $n = 3$.

Applied potential in V vs. SHE	Max j in $\mu\text{A cm}^{-2}$	Start-up time in h	Biofilm thickness in μm	η_C in %
-0.1	$244 \pm 19 \%$	$20.4 \pm 20 \%$	$23 \pm 30 \%$	63 ± 8
0	$352 \pm 24 \%$	$19.8 \pm 13 \%$	$35 \pm 17 \%$	66 ± 9
+0.05	$377 \pm 35 \%$	$20.0 \pm 26 \%$	$34 \pm 38 \%$	65 ± 12
+0.1	$399 \pm 24 \%$	$19.2 \pm 7 \%$	$38 \pm 18 \%$	71 ± 7
+0.2	$384 \pm 38 \%$	$22.3 \pm 4 \%$	$35 \pm 20 \%$	67 ± 6
+0.3	$417 \pm 20 \%$	$41.4 \pm 12 \%$	$29 \pm 24 \%$	54 ± 12

Considering the start-up time, it was noticeable that five of six applied potentials showed similar start-up times from 19.2 to 22.3 h, however for +0.3 V vs., SHE which produced the highest current, the start-up time was significantly increased to 41.4 h. Overall, SD for the start-up time was lower for five of six applied potentials compared to SD for the maximum current density. For example for +0.1 V vs. SHE and +0.2 V vs. SHE the start-up time was very reproducible (SD = 7, respectively 4 %) even though current density showed large deviations among the triplicates (SD = 24, respectively 38 %).

In order to assess any interdependence between biofilm thickness, η_C and other MFC parameters, Pearson correlation coefficients (ρ) were calculated, using the function *rcorr()* from the R-package *Hmisc* [181, 182]. The correlation matrix is displayed in the Appendix in Table A.2. Mathematically, there was no linear correlation between the applied potential and any of the parameters, but biofilm thickness correlated positively with maximum current density ($\rho = 0.79$, $p < 0.0001$). Hence, the thicker the biofilm, the higher was the maximum current. Further, η_C correlated positively with biofilm thickness ($\rho = 0.74$, $p < 0.001$) and negatively with the start-up time ($\rho = -0.72$, $p < 0.001$), meaning that the thicker the biofilm, the higher is also the efficiency of conversion from acetate to current and the same effect has a short start-up time: the earlier current production sets in, the more efficient it is. Interestingly, length of start-up time did not correlate with maximum current production, i.e. even if the bacterial culture takes a long time for current onset, quality of current production would not be impaired (as seen for +0.3 V vs. SHE applied).

The positive correlation of biofilm thickness with current density and η_C is in fact supported by the analysis of Korth et al. who reported for *Geobacter*-dominated biofilms in MFC that quasi-steady state/mature biofilms transfer electrons more efficiently than early-stage biofilms where more electrons remain in cells and EPS [183]. Even though, in the presented experiments, A was not an early-stage biofilm but still significantly thinner compared to B-F, the hypothesis by Korth et al. might still be applicable. It is then able to explain the higher current densities for biofilms B-F compared to A and the higher η_C of F compared to A-E.

A representative CLSM image of a biofilm for each potential is shown in Figure 4.12 (-0.1, 0, +0.05, +0.1, +0.2, +0.3 V vs. SHE from A to F). Biofilms were stained with LIVE/DEAD™ stain immediately after the end of the experiment and the colours of the digital image were inverted for better visibility. The higher the amount of blue

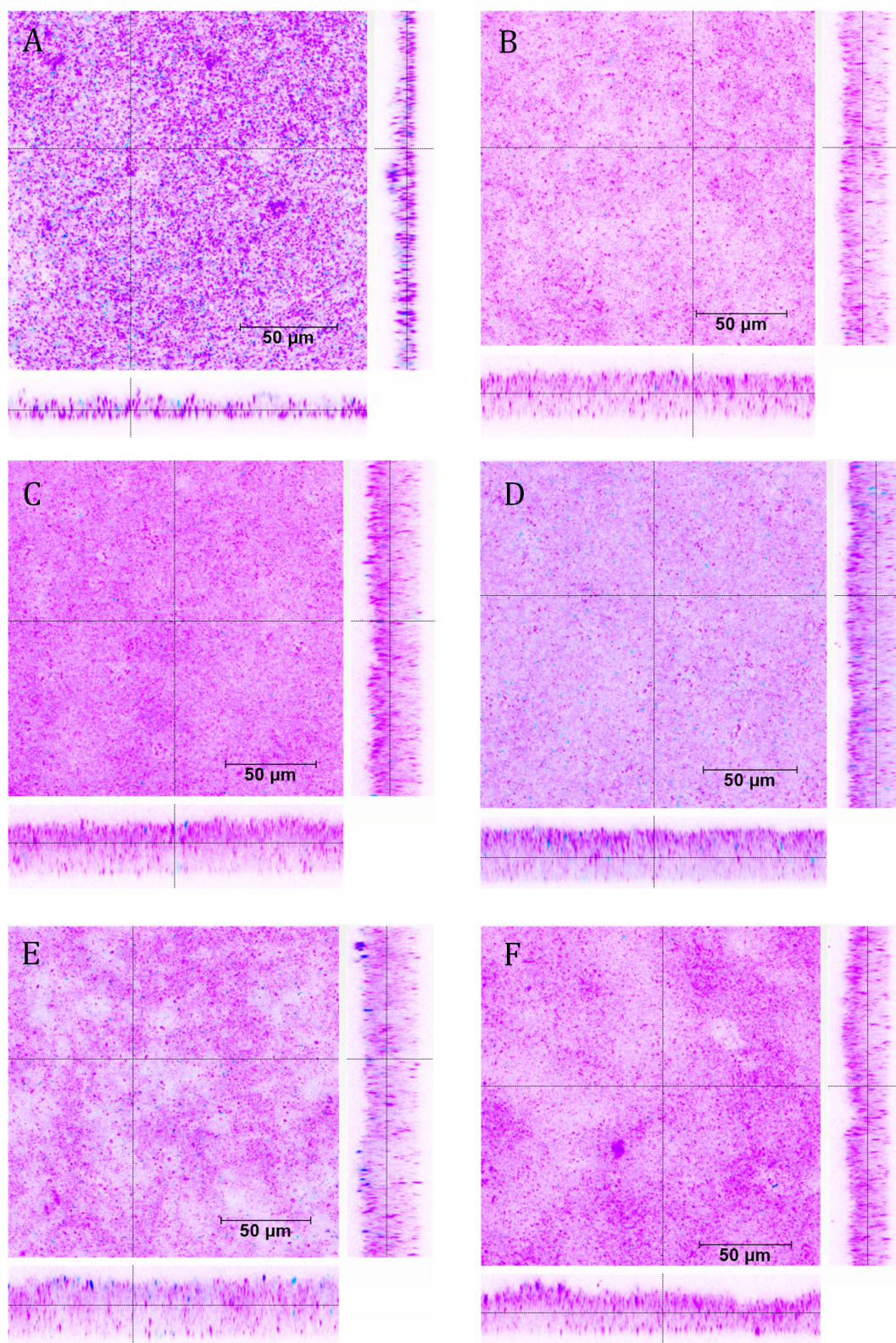


FIGURE 4.12: The image compilation shows CLSM images in xy- and xz-representation for the applied potentials on ITO electrodes; from A to F: -0.1, 0, +0.05, +0.1, +0.2, +0.3 V vs. SHE. Biofilms were stained with LIVE/DEAD™ stain and colour of the digital image inverted. The higher the amount of blue stain in the image, the higher the fraction of dead cells in the biofilm.

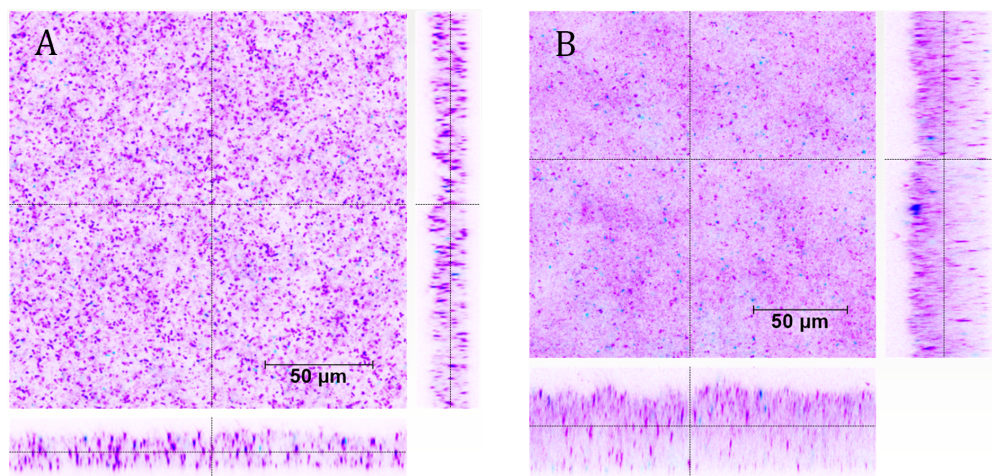


FIGURE 4.13: Shown are two biofilms of the biological triplicate at +0.05 V vs. SHE on ITO with a width of 22 μm for A and 46 μm B, which is obviously significantly different, resulting in an SD of 13 μm .

stain in the image, the higher the fraction of dead cells in the biofilm. Displayed are xy-images of the middle layer of each biofilm together with the xz-representation to inspect lateral biofilm integrity and thickness. As calculated in the correlation analysis biofilm thickness correlated positively with maximum current produced and the thinnest biofilm with the least maximum current for -0.1 V vs. SHE also showed the highest fraction of dead cells in the biofilm (4.12 A). A qualitative comparison did not reveal any major differences between biofilms for the other potentials applied. Also, no reason for the significantly longer start-up time of the biofilm at +0.3 V vs. SHE could be identified from qualitative analysis of the CLSM image (4.12 F).

Emphasised should be the high SD in biofilm thickness for the biofilm at +0.05 V vs. SHE with 13 μm while SD for the other potentials applied were 6, respectively 7 μm . To show that this was not an artefact of the method applied to determine biofilm thickness, representative images of the two other experiments conducted at this potential are shown in Figure 4.13. The biofilm shown in A is obviously significantly thinner (and displays a higher proportion of dead cells) than the biofilm in B and the third one, shown in C in Figure 4.12. Additionally, the thinner biofilm appeared more agglomerated compared to biofilm B in Figure 4.13 and C in Figure 4.12, which have a more uniform appearance. This might also hint lower productivity. In the particular order, the calculated biofilm thickness was 22, 46 and 35 μm , resulting in the said SD of 13 μm . This is most probably also the reason for the high SD (35%) for maximum current density, considering the correlation between biofilm thickness and maximum current production.

For subsequent *G. sulfurreducens* MFC experiments on ITO electrodes +0.1 V vs. SHE was chosen as the optimum potential, taking into account the analysis of relevant parameters. The maximum current density for applied potentials between 0 and +0.2 V vs. SHE did not differ significantly, nonetheless the start-up time was the shortest and most reproducible for 0.1 V vs. SHE, as well as a comparably thick biofilm was produced at this potential, with a high η_C furthermore.

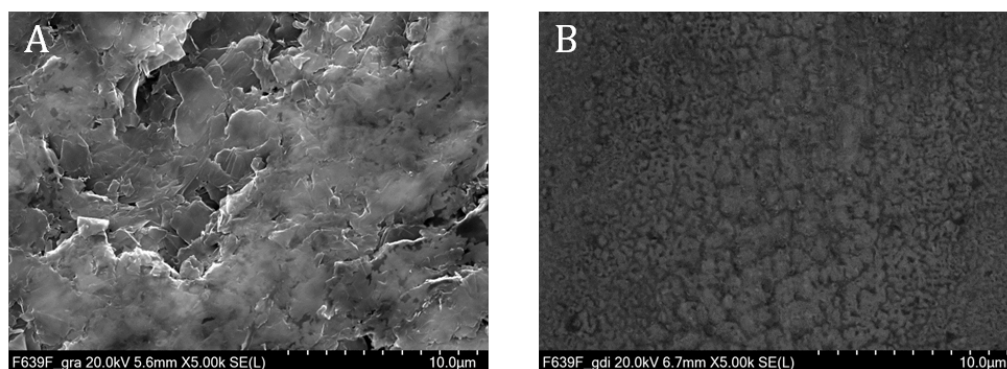


FIGURE 4.14: SEM images of graphite and ITO electrode surfaces at 5000x magnification. A shows the graphite surface which is rougher compared to the smooth surface of the ITO coated glass slides in B.

The distinct behaviour of *G. sulfurreducens* depending the electrode material and the applied potential was unexpected and will be discussed in the following.

Most lab-scale MFC are operated with poised anodes to drive *G. sulfurreducens* EET. Thereby, the more positive the potential, the higher the energy supplied to the system. The fact that *G. sulfurreducens* did not produce current on ITO at +0.6 V vs. SHE while it did on graphite anodes suggests that the applied potential is received differently depending on the electrode material. Figure 4.14 shows SEM images of a sand-paper polished graphite electrode (A) and ITO coated glass (B) at 5000x magnification. Even though the graphite electrodes were polished prior to each experiment, the surface was still furrowed and rougher than the ITO vaporised glass slides that have a smooth surface. The furrows are reflected by the biofilm with a more uneven surface, but no other structural differences could be observed in the biofilm (Figure 4.15). Also, the surface potential measured with the HR-SKP was almost identical with 0.57 V vs. SHE for graphite and 0.60 V vs. SHE for ITO. Hence, it might be the surface topology that not only influences how efficiently bacteria interact with the electrode but also if at all.

This effect was described in [101] as well, for graphite and AuPd sputtered glass. While only little current was produced on AuPd at +0.2 and +0.4 V vs. SHE, a maximum of $100 \mu\text{A cm}^{-2}$ was produced at 0 V vs. SHE (SD was very high in these experiments but the trend was observable). On graphite, current output for 0 and +0.2 V vs. SHE was comparable in [101] (to each other and to AuPd at -0.2 V) but with significantly shorter start-up time at +0.2 V. In [102] the authors reported current production on glassy carbon for 0 V and +0.4 V vs. SHE while reactors with ITO electrodes only had a current response for 0 V vs. SHE.

While these studies reported no or significantly lower current production on ITO for high potentials (+0.4 V vs. SHE), in this work current production at +0.3 V vs. SHE was equally high compared to 0 V vs. SHE, only the start-up time was twice as long and the biofilm slightly thinner but equally viable (Figure 4.11 F and 4.12 F). The molecular mechanisms of *G. sulfurreducens* to adapt to different potentials were described in more detail in [184] and were put into perspective with the need of the organism to adapt to various TEA/a variety of metal oxides in its natural environment. When confronted with a low electrode potential/TEA with low redox potential, genes related to energy conservation were upregulated to compensate for the oxidation of TEA with low redox potential. Also OmcZ concentrations in the EPS

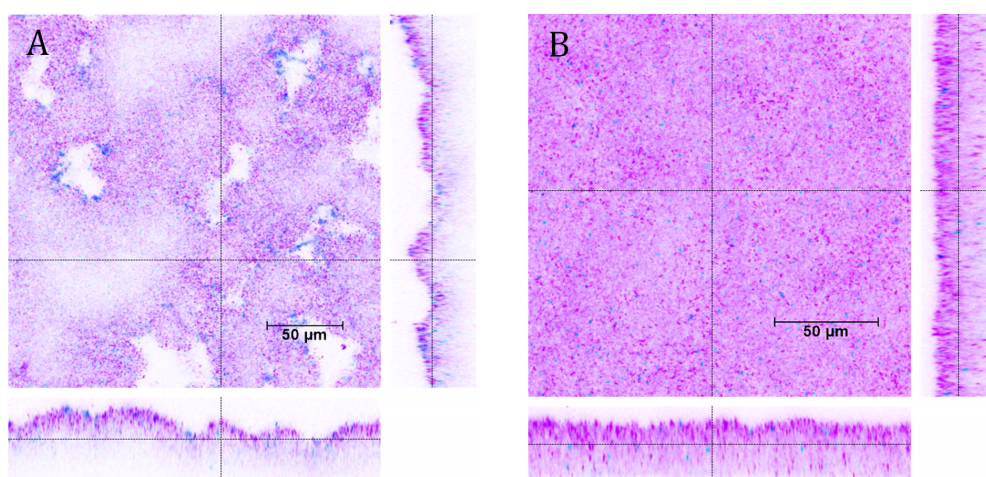


FIGURE 4.15: Shown are LIVE/DEAD™ stained CLSM images of the biofilm surface structure, comparing MFC on graphite (A) and on ITO electrode (B). On these two representative images the focus plane was located just below the biofilm surface to emphasise the more wrinkled structure for the biofilm on the graphite surface.

were increased at lower potentials to maximise EET, while the amount of OmcZ was reduced at high potentials ($> +0.4$ V vs. SHE), presumably to protect the cells from oxidative stress [184]. Further, different redox proteins in the inner membrane were addressed upon change in potential, with a low threshold of -0.1 V vs. SHE. Zacharoff et al. reported that at potentials higher than -0.1 V vs. SHE the inner membrane cytochrome CbcL was preferred in electron transport, while below that ImcH was used [185]. It was emphasised that the whole EET relay is tunable upon changes in electrode potential, making *G. sulfurreducens* very robust towards natural and artificial changes in the redox potential of its surrounding [184, 186].

Those changes in catabolism might explain the current patterns seen for ITO MFC in this work. Assumed that the “low potential redox system” was active at -0.1 V vs. SHE applied, it is less efficient in correcting for the lower potential energy added to the system, so that the current density was significantly lower, as observed in Figure 4.11 A. While it would explain a lower efficiency in current production (low η_C) it does not necessarily explain the thinner and less viable biofilm, as the low potential should not have caused the cells any stress.

For moderately high potentials, in between 0 and $+0.2$ V vs. SHE, no significant change was identified for any of the performance indicators which appeals an earlier theory by Bond et al. that above a certain thermodynamic threshold *G. sulfurreducens* “does not take advantage of excess available potential energy” [63]. This hypothesis was supported by the findings in this work that none of the performance indicators was linearly correlated to the applied potential. This is also valid for other studies on ITO electrodes, e.g. in [187] with the optimum potential identified as $+0.2$ V vs. SHE or [188] with $+0.05$ V vs. SHE.

What remains is the high start-up time at $+0.3$ V. For high potentials ($> +0.2$ V vs. SHE) another adaptation, different to that for > -0.1 V vs. SHE might apply, as here current production is equally high, only start-up is prolonged. In that case the production of protective substances like non-conductive polysaccharides might play a role, as reported in [189] for *G. soli*. The authors hypothesised that high potentials

stimulate a stress response which triggers EPS production and this has to be balanced with efficient electron transfer. In the given example this balance might be established during the prolonged start-up phase and the high current density reached in the course of the experiment underlines the adaptive potential of *G. sulfurreducens*.

This experimental series highlighted how important it is to determine the appropriate potential for poised anodes with respect to the electrode material used. This might even extend to optimising pH and ionic strength as emphasised by He et al. in their spatially resolved model on tunable EET relays [186].

4.6 MFC with LbL-coated electrodes

Coating combinations (PEI-PSS)₂, (PEI-PSS)₂-CHI, (PEI-PSS)₂-PEI-ALG and (PEI-PSS)₂-PEI, whose surface potential was analysed in section 4.2.2, were coated on ITO electrodes to analyse the effect of surface charge on *G. sulfurreducens* in MFC performance. In the following, the coatings are referred to as *PSS-*, *CHI+*, *ALG-* and *PEI+*, named for the final layer of each coating and its terminal charge. PSS as final layer resulted in a strongly negatively charged surface (0.71 V vs. SHE), ALG was less but still negatively charged (0.66 V vs. SHE), similar to the non-coated ITO surface (0.6 V vs. SHE). CHI as the final layer resulted in a slightly more positive charge compared to ITO (0.57 V vs. SHE) and PEI as the final layer produced by far the most positively charged surface (0.34 V vs. SHE) (Table 4.3). For application in the MFC experiment, electrodes were coated “in-place” as described in the final paragraph of section 3.7.4, to omit any negative influence of the coating on the contact between graphite paper and the conductive ITO layer. Hence, the WE-electrical setup for this experiment was identical to MFC experiments on non-coated ITO. Electrochemical cultivation was as described in section 3.5.3, with +0.1 V vs. SHE applied potential as a result of the findings described in section 4.5.

The recorded current density curves are shown in Figure 4.16, together with the result for non-coated ITO at +0.1 V vs. SHE. Due to the versatile behaviour depending on the electrode coating, experiments were terminated at different time points. Shown are biological duplicates of the electrode coatings *PSS-*, *CHI+*, *ALG-* and *PEI+*.

First of all, the current density curves showed that the experimental duplicates were reproducible for *PSS-* and *CHI+*, whereas deviation was higher for *ALG-* and *PEI+* but with a definite trend still. Noticeable was a considerably lower deviation for *CHI+* current curves compared to deviations seen on non-coated ITO in previous experiments. All recorded parameters are summarised in Table 4.7. *PSS-* produced by far the highest current densities with 456 $\mu\text{A cm}^{-2}$ and 377 $\mu\text{A cm}^{-2}$ and also the shortest start-up time (17.9 h and 20.9 h). High currents were produced by 43 μm thick biofilms and with a η_{C} of 74 % and 71 %. The maximum current produced by *CHI+* was about 60 % of *PSS-* maximum current with a start-up time almost twice as long. Analogous to the lower current density the biofilm for *CHI+* coating was thinner with 25 μm , respectively 19 μm . Also η_{C} was lower with 54 %.

Biological duplicates for *ALG-* and *PEI+* showed to be less reproducible and with poor productivity. Maximum current density for *ALG-* was 130 $\mu\text{A cm}^{-2}$, respectively 71 $\mu\text{A cm}^{-2}$ with 54.4 h start-up time for one experiment and a largely extended start-up time of 87.5 h for the other. Associated with the long start-up was a low η_{C} with only 8 %, compared to 42 % for the first *ALG-* MFC. Biofilms were thinner than on *CHI+* electrodes with 15 $\mu\text{m} \pm 60\%$, respectively 14 $\mu\text{m} \pm 50\%$. Considering the *PEI+* coat, surface modification led to no significant current production for one

TABLE 4.7: Maximum current density, start-up time, biofilm thickness and η_C for two experiments on each coating *PSS-*, *CHI+*, *ALG-* and *PEI+*. Mean and SD for non-coated ITO as are given as reference ($n = 3$).

Coating	Max j in $\mu\text{A cm}^{-2}$	Start-up time in h	Biofilm thickness in μm	η_C in %
<i>PSS-</i>	456	17.9	$43 \pm 14\%$	74
	377	20.9	$43 \pm 14\%$	71
<i>CHI+</i>	264	36.9	$25 \pm 20\%$	54
	227	38.5	$19 \pm 32\%$	54
<i>ALG-</i>	130	54.4	$15 \pm 60\%$	42
	71	87.5	$14 \pm 50\%$	8
<i>PEI+</i>	81	58.0	-	24
	-	-	-	-
ITO	$399 \pm 24\%$	$19.2 \pm 7\%$	$38 \pm 18\%$	71 ± 7

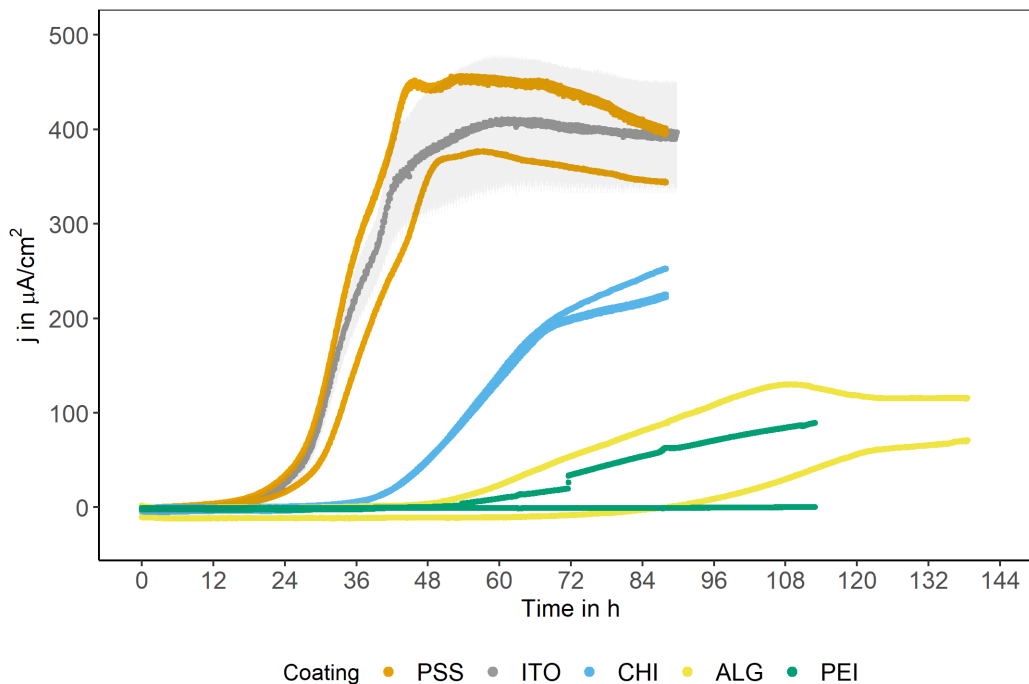


FIGURE 4.16: Current density curves of each two H-cell experiments at +0.1 V vs. SHE for each type of coating are shown with non-coated ITO in grey (mean as solid line, SD as ribbon with $n = 3$), *PSS-* in orange, *CHI+* in blue, *ALG-* in yellow and *PEI+* in green.

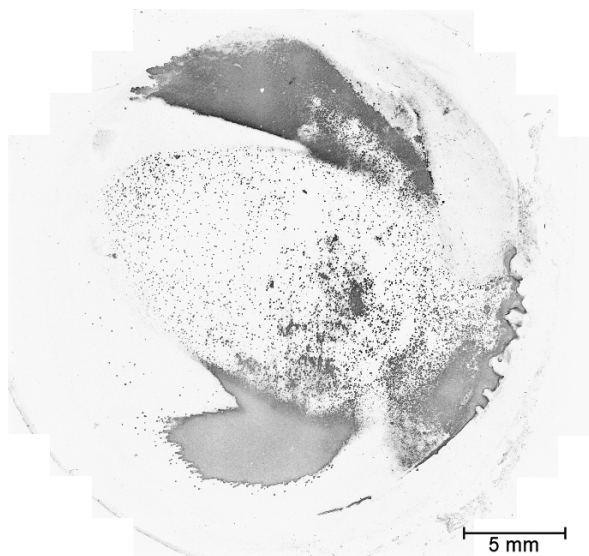


FIGURE 4.17: The Syto9 channel of the LIVE/DEAD™ stained biofilm on a *PEI+* coated electrode is shown, contrast was enhanced and image shown in grey scale for better visibility. Only patches of fully developed biofilm are present at the time point the experiment was terminated (114 h). In the central area micro colonies as the first stadium of biofilm formation are visible (see close-up in Figure 4.18).

experiment and to $81 \mu\text{A cm}^{-2}$ for the other with a start-up time of 58.0 h which was comparable with the start-up time for the faster of the *ALG-* experiments. η_C was 24 %. Biofilm thickness was not calculated for the *PEI+* MFC since no mature biofilm had developed at the time point at which the experiment was terminated. CLSM analysis showed that only patches of mature biofilm had developed within 113 h, while in the middle section micro colony formation was visible. Hence, biofilm formation had not concluded at the point the experiment was terminated. The whole electrode is shown in Figure 4.17 with a close up on micro colonies in Figure 4.18.

Besides quantification of biofilm thickness, results of the LIVE/DEAD™ staining were evaluated qualitatively, a compilation of representative images for the three coating combinations is shown in Figure 4.19. It clearly showed that the biofilms on *ALG-* coating were less viable compared to *PSS-* and *CHI+* (high fraction of blue cells) which was probably the reason for the low current production even though a mature biofilm had formed. This was in contrast to the biofilm on *PEI+* coat, which produced low current density due to an immature biofilm.

In the following, the described results on coated electrodes will be put into relation with the abiotic surface analysis in section 4.2.2.

The applied coatings altered the surface charge and potential, i.e. the electrical field in proximity to the electrode surface as follows: *PSS-* > *ALG-* > ITO > *CHI+* >> *PEI+*. However, the current density curves did not resemble the changes in surface potential accordingly, as the biofilm grown on *PSS-* was the thickest and most viable and produced the highest current with the shortest start-up time and the highest η_C . This correlation of a thick biofilm, high current density and high η_C resembled the result of the potential optimisation experiment (section 4.5). Again, it supports the hypothesis formulated by Korth et al. [183] and indicates that a steady-state biofilm was formed on *PSS-* coated electrodes. In contrast, the lower η_C for *CHI+* and *ALG-*

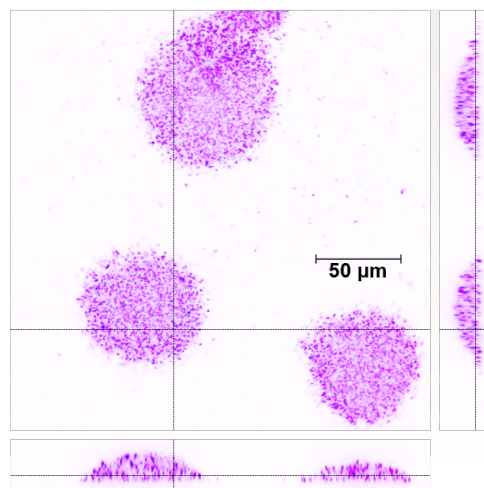


FIGURE 4.18: A detail of the central area of the biofilm on the *PEI+* coated electrode is shown (both channels of the LIVE/DEAD™ stained biofilm image). The micro colonies seen are the early stage of biofilm formation and comprise an immature biofilm at the time point that the experiment was terminated (114 h).

imply immature biofilms where more electrons remain in cells and EPS. In general, the parameters biofilm thickness and viability, current density, start-up time and η_C showed consistency when analysed separately for the respective coatings: the thicker and the more viable the biofilm, the more current was produced, the shorter the start-up time and the higher the η_C .

MFC performance depending on the coating can therefore be ranked as PSS = ITO >> CHI > ALG = PEI. Hence, for the chosen setup, the influence of the surface potential was not as straight forward as: “positively charged polymers are preferred over negatively charged” and contradicted the initial hypothesis.

The study that is closest related to the results from this work is the one published by Guo et al. [123]. They extracted from their work that MFC performance with functional groups added to a glassy carbon surface can be ranked as $-N^+(CH_3)_3 > -OH > -SO_3^- \gg CH_3$; for biomass deposited on the electrode, maximum current and start-up time, though they used a mixed community dominated by *Geobacter* (no pure culture) and had a system with a prolonged start-up time for all cultures (23 to 37 days at 0 V vs. SHE). Also there was no comparison to the non-modified electrode surface, so it is unknown whether the modification improved the MFC performance at all. Still, their work is in line with the hypothesis that hydrophilic, positively charged surfaces are best suited for biofilm formation in MFC [118].

Interestingly, quaternary ammonium compounds are also used for their antimicrobial properties since excessively strong positive electrostatic force potentially rupture the cell surface [190]. Since EIS analysis of *PEI+* coated electrodes showed an increase in R_{CT} in addition, this effect might blend with the potential antimicrobial effect of the chemical structure. This might be an explanation for the poor performance of the *PEI+* coated electrode, even though PEI was also used as compound material with CNT in [191] with power increase. While $-SO_3^-$ was ranked as less favourable than $-N^+(CH_3)_3$ in [123] it did not impair biofilm growth as functional group of PSS in this work. Positively charged CHI is known as biocompatible material and often used to form hydrogels [116, 192, 193] but does not seem to boost MFC performance when

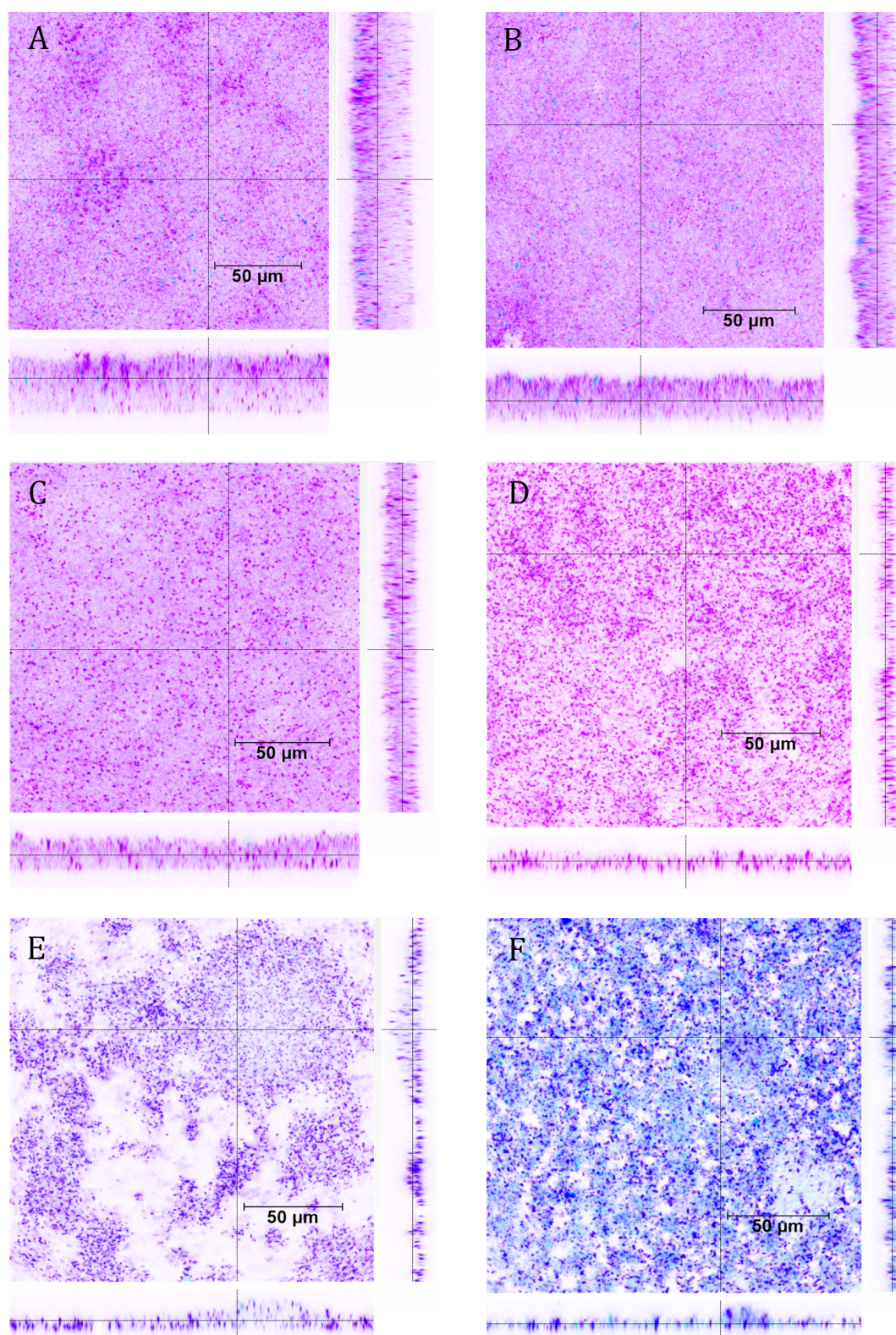


FIGURE 4.19: The compilation shows the LIVE/DEAD™ stained biofilms on coated ITO electrodes. The higher the fraction of blue/violet cells are in an image, the more dead cells are present in the biofilm. A and B are biofilms on PSS- coated electrodes, C and D on CHI+ coating and E and F are images of the biofilms formed when the electrode was coated with the ALG-.

used solely as electrode coating and without compounds to increase the electrode surface. The same is valid for ALG- coated electrodes; Known as biocompatible material and used to form microcapsules and hydrogels [194] ALG impaired biofilm formation in this work. This effect could not be attributed to the surface potential as ALG- coating did not have a drastically altered surface potential compared to the ITO and PSS- surface that produced significantly higher currents. However, ALG- coating led to an increased impedance compared to the non-coated ITO which might have influenced performance adversely. PSS as a negatively charged polymer resulted in a higher surface potential than the bare ITO electrode and still led to similar MFC performance with a thick and viable biofilm. Thus, the negative surface potential did not impair MFC performance at all, in contrast to the hypothesis that it might repel the identically charged bacteria surface. However, also PSS- coating did not improve MFC performance in comparison to non-coated ITO.

It should be emphasised that the analysis of charge and surface potential in this and in cited studies did not include the interaction of medium and the applied potential with the electrode surface. Although the incubation of bare graphite and (PEI-PSS)₂-PEI in anolyte revealed that the surface potential becomes more negative and suggests the adsorption of anions, it is a matter of discussion which surface potential the bacteria actually face upon start of the MFC experiment. As put in [195] an initial coating is highly influenced by its surrounding medium and negatively charged surfaces will naturally attract cations that eventually cover the initial coat. Further, the zeta potential of *G. sulfurreducens* cells was not measured in the actual anolyte (as its osmolarity is too high for the Zeta Sizer®), so the cellular surface might actually be charged differently when in the *G. sulfurreducens* growth medium. Additionally, little is known about the effect of electrode coating on the conditioning film that is formed prior to cellular adhesion and depends highly on microbial community, medium, pH, temperature and salt content. Referring to the results obtained in this work, this might explain why the polyanion PSS as cell facing layer performs just as well in an MFC as the non-coated ITO: both surfaces might attract just the same (positively charged) medium components covering up the initial coating. In contrast, all other coatings triggered effects that significantly impaired the initial cellular adhesion.

These results on MFC performance on LbL-coated ITO electrodes, together with the abiotic characterisation of the electrodes (sections 4.2.2 and 4.2.3), were published in [196].

4.7 Implementation of the electrochemical flow cell for continuous biofilm monitoring

4.7.1 Establishing the fluorescent strain *G. sulfurreducens* mCh

Key to the bioelectrochemical flow cell developed in [149] is real-time biofilm monitoring in order to analyse early phases of biofilm formation. Hence, CLSM imaging during the experiment is a major advantage of the flow cell system in contrast to H-cell experiments which only allow end-point analysis of the biofilms formed. CLSM imaging however requires fluorescence signals of the object of interest, so a fluorescent *G. sulfurreducens* was required to establish the MFC flow cell system with *G. sulfurreducens* as MFC model organism.

A red fluorescent strain, expressing an mCherry encoding gene (*G. sulfurreducens* mCh) was kindly provided by Derek Lovley's group [154] and first tested on graphite electrodes in H-cells. Identical conditions to the WT experiments described in section 4.4 were chosen - but no current was produced by the fluorescent strain. Instead, in order to initiate current production, fumarate as soluble electron acceptor had to be added at the beginning of the experiment. When 10 mM fumarate were added prior to inoculation, current was produced, as displayed in Figure 4.20. Both, current density (solid line) and OD₆₀₀ (crosses) are displayed for WT (in grey) and mCh (in orange). For the WT a current curve similar to those shown in section 4.4 (without fumarate supplement) was obtained, with a maximum current density of 430 $\mu\text{A cm}^{-2}$. Current production was higher with fumarate added but this could be attributed to a higher OD₆₀₀ due to cell growth after inoculation (as seen in Figure 4.20). Current production set in at the point of maximum OD₆₀₀, at which cell growth ceased because soluble electron acceptors were consumed entirely (fumarate and malate analysed with HPLC, data not shown). In contrast to the WT, current density reached with the fluorescent strain only reached a maximum of 26 $\mu\text{A cm}^{-2}$, which is about 6 % of the WT maximum current density. Also, current production did not show the characteristic peak, instead it was produced constantly at low level. Figure 4.21 shows CLSM images of the corresponding biofilms; with the mCherry fluorescence signal (A) and a LIVE/DEAD™ stained *G. sulfurreducens* WT biofilm in B. The *G. sulfurreducens* mCh biofilm is extremely thin with only 3-4 μm and no complete coverage of the electrode, while the WT biofilm is uniform with $25 \pm 6 \mu\text{m}$ thickness.

In summary, the red fluorescent strain produced poor currents due to impaired biofilm formation and also needed a soluble electron acceptor as "kick-starter" for current production.

To test if already a planktonic cell culture of the fluorescent strain behaved differently, a growth curve was monitored over time and compared to *G. sulfurreducens* WT growth. Growth experiments were conducted as described in section 3.3. The WT reached an OD₆₀₀ of 0.43 in 45 h with a generation time of 3.7 h. *G. sulfurreducens* mCh reached an OD₆₀₀ of 0.38 in the same time. The growth curves are shown in the Appendix in A.3. Metabolite concentrations were also monitored for both strains during growth (acetate, fumarate, malate, succinate) but no altered behaviour was observed (data also shown in A.3). The strain also showed bright red fluorescence when observed under the CLSM. Hence, only biofilm formation but not planktonic growth was impaired for *G. sulfurreducens* mCh.

Subsequently, MFC performance of the fluorescent *G. sulfurreducens* strain was tested on ITO electrodes (with fumarate supplement) and at different potentials in case the potential applied for the WT was not optimal for *G. sulfurreducens* mCh. The

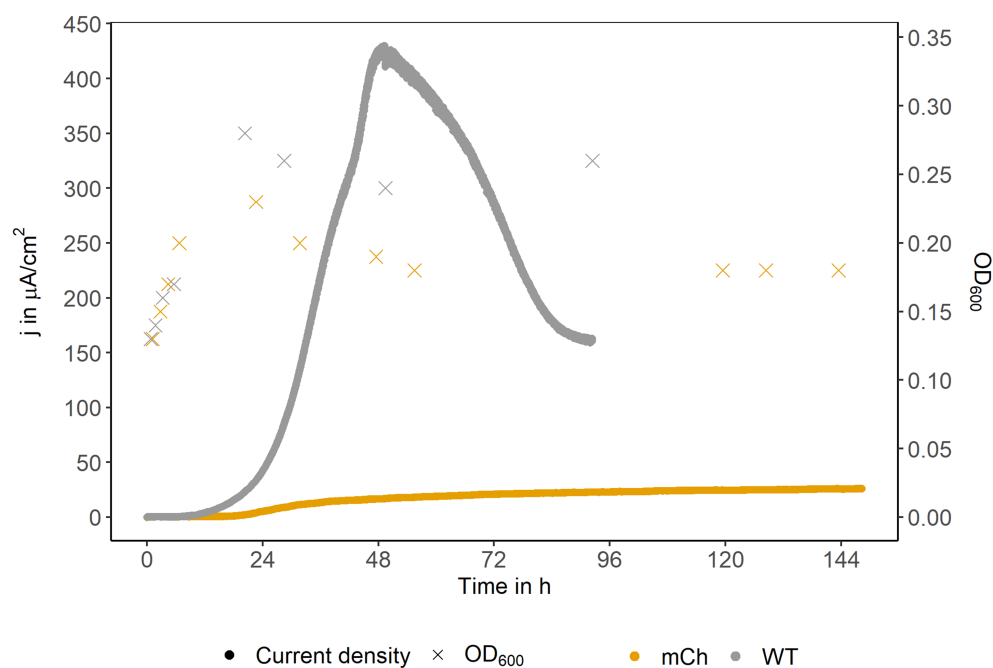


FIGURE 4.20: Current curve and OD_{600} of the MFC experiment with *G. sulfurreducens* mCh (in orange) and *G. sulfurreducens* WT (in grey) with fumarate supplement on graphite electrodes. The solid line shows the current density (left y-axis), the crosses show OD_{600} (right y-axis). The soluble electron acceptor allowed initial cell growth until fumarate was consumed. Current production set in when cell growth ceased (after approximately 24 h).

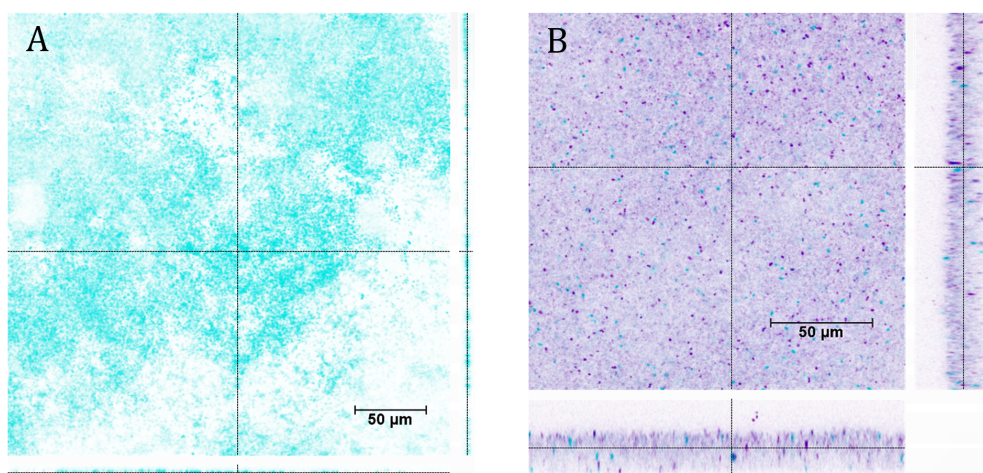


FIGURE 4.21: Biofilms of *G. sulfurreducens* mCh (A) and WT (B) on graphite electrodes at +0.6 V vs. SHE with fumarate supplement are shown (mCherry fluorescence signal, *G. sulfurreducens* WT biofilm LIVE/DEAD™ stained). The *G. sulfurreducens* mCh biofilm was extremely thin with only 3-4 μm and no complete coverage of the electrode, while the WT biofilm was uniformly grown with $25 \pm 6 \mu\text{m}$ thickness.

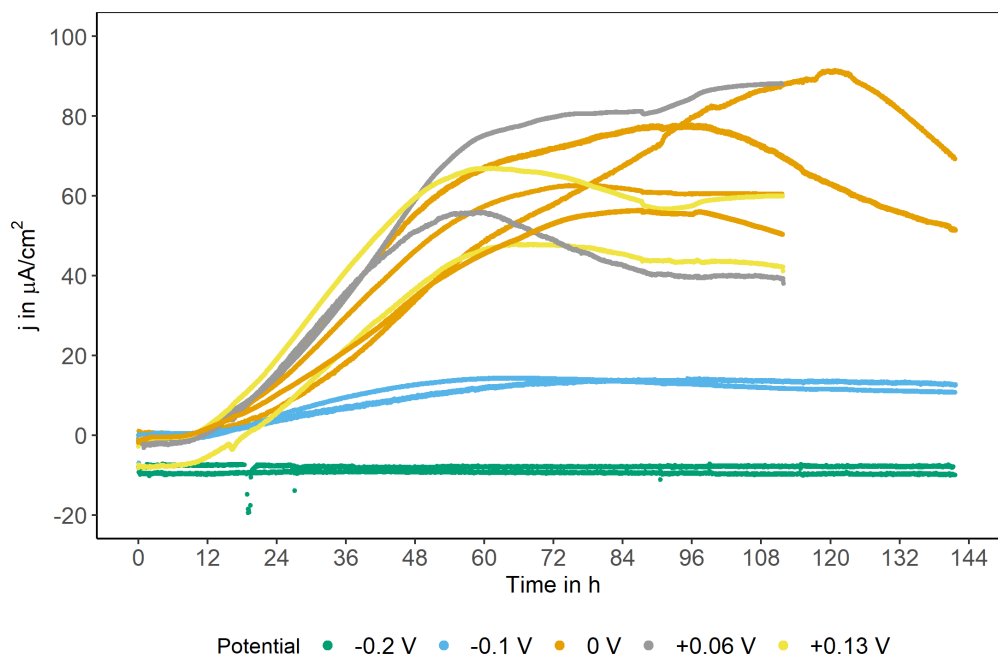


FIGURE 4.22: Current curves of MFC experiments with *G. sulfurreducens* mCh with 10 mM fumarate supplement on ITO electrodes. -0.2 V, -0.1 V, 0 V, +0.06 V and +0.13 V were applied to identify the potential with maximum current output. Potentials are indicated as vs. SHE.

potentials applied were -0.2, -0.1, 0, +0.06 and +0.13 V vs. SHE. Experiments were executed as biological duplicates, respectively quadruplicate for 0 V applied. Current curves are displayed in Figure 4.22. At -0.2 V vs. SHE no current was produced, -0.1 V vs. SHE produced a maximum of $14 \mu\text{A cm}^{-2}$ for both experiments, with current progression similar to the one observed on graphite. Results for the other applied potentials showed higher deviations: 48 and $67 \mu\text{A cm}^{-2}$ at +0.13 V vs. SHE, 56 and $88 \mu\text{A cm}^{-2}$ for +0.06 V vs. SHE and $72 \mu\text{A cm}^{-2} \pm 22\%$ on average for 0 V vs. SHE ($n = 4$). Hence, the optimum potential lied in the range of 0 to +0.13 V vs. SHE, as it did for *G. sulfurreducens* WT. However, as already observed for MFC experiments on graphite, maximum current density was significantly lower for *G. sulfurreducens* mCh, compared to the WT strain. +0.1 V vs. SHE as the optimum potential chosen for the WT strain produced a maximum current of $399 \pm 24\%$ while 0 V vs. SHE on ITO for *G. sulfurreducens* mCh led to only 18% of the maximum current reached for the WT strain. That was most probably caused by impaired biofilm formation as shown in Figure 4.23 with representative images for biofilms on ITO at +0.13 V vs. SHE (A) and 0 V vs. SHE (B). Biofilm structure was patchy and inhomogeneous in comparison to the WT and also not brightly fluorescent across the whole biofilm depth, as seen in the z-section.

An interesting finding of the experiments with *G. sulfurreducens* mCh on ITO, when fumarate was added initially, was a very short start-up time compared to the WT. For the chosen potential of +0.1 V vs. SHE the WT had a start-up time of $19.2 \text{ h} \pm 7\%$ while the time for the fluorescent strain was below 12 h in the potential range of 0 to 0.13 V vs. SHE. Possible explanations for that are the higher OD_{600} due to the addition of fumarate or that the cells were in exponential growth phase during

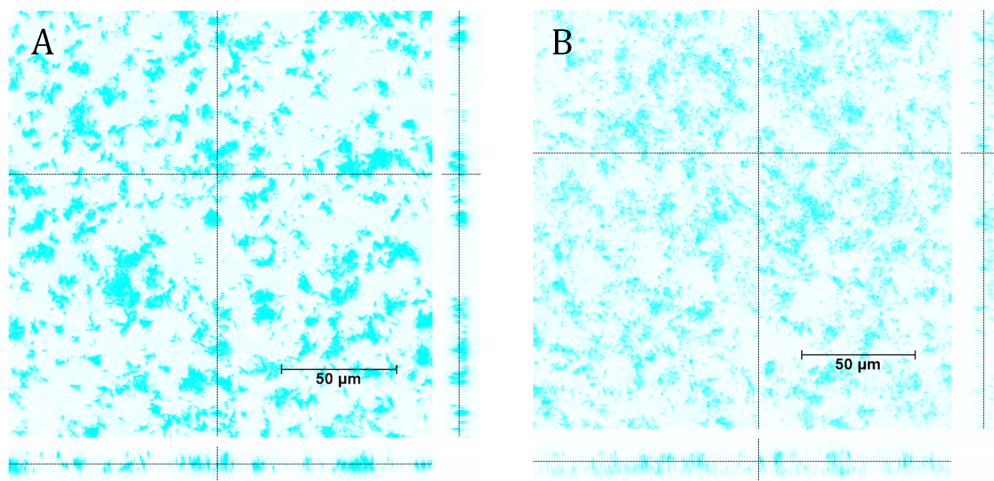


FIGURE 4.23: Biofilms of *G. sulfurreducens* mCh with fumarate supplement on ITO electrodes (mCherry fluorescence displayed). (A) shows the biofilm at +0.13 V vs. SHE, (B) at 0 V vs. SHE.

start-up of the experiment while the usual inoculum contains stationary cells.

Concluding, MFC experiments on ITO at different potentials confirmed the impression from the tests on graphite, that the fluorescent strain *G. sulfurreducens* mCh did not perform as expected in MFC experiments, even at optimum potentials.

G. sulfurreducens mCh was originally constructed for the use with a green fluorescent pH-sensitive dye to analyse the change of pH in a biofilm in real-time [154]. The authors compared the recombinant strain to the WT and found no significant difference in power output under the experimental conditions applied (graphite anode, 560 Ω resistor instead of poised potential). However, under the given setup, they reported a long start-up time of approximately 160 h for the WT and 200 h for *G. sulfurreducens* mCh. While a longer start-up time without poised potential is expected, the longer start-up time of the mCh strain compared to the WT could indicate impaired adhesion (and biofilm formation) already.

It is unclear whether the strain was already impaired in the studies conducted in [154] and the effects did not appear on non-poised electrodes or if the strain was damaged during storage. It was attempted to re-transform the WT strain used in this work with the plasmid pRG5mCh isolated from *G. sulfurreducens* mCh but this was not successful as the laboratory was not properly equipped for the transformation of anaerobic bacteria.

As there was no alternative strain on hand that could be used in MFC, formed good biofilms and did not need fluorescent staining for visualisation with the CLSM, *G. sulfurreducens* mCh was used for proof-of-concept experiments at a potential of 0 V vs. SHE in the bioelectrochemical flow cell, despite its short-comings.

4.7.2 Electrochemical flow cell characterisation

For easier handling and more robust electrical contacting, construction and geometry of the flow cell were further improved, based on the design of Stöckl et al. [149]. Therefore, properties of the abiotic electrochemical system were reassessed via EIS.

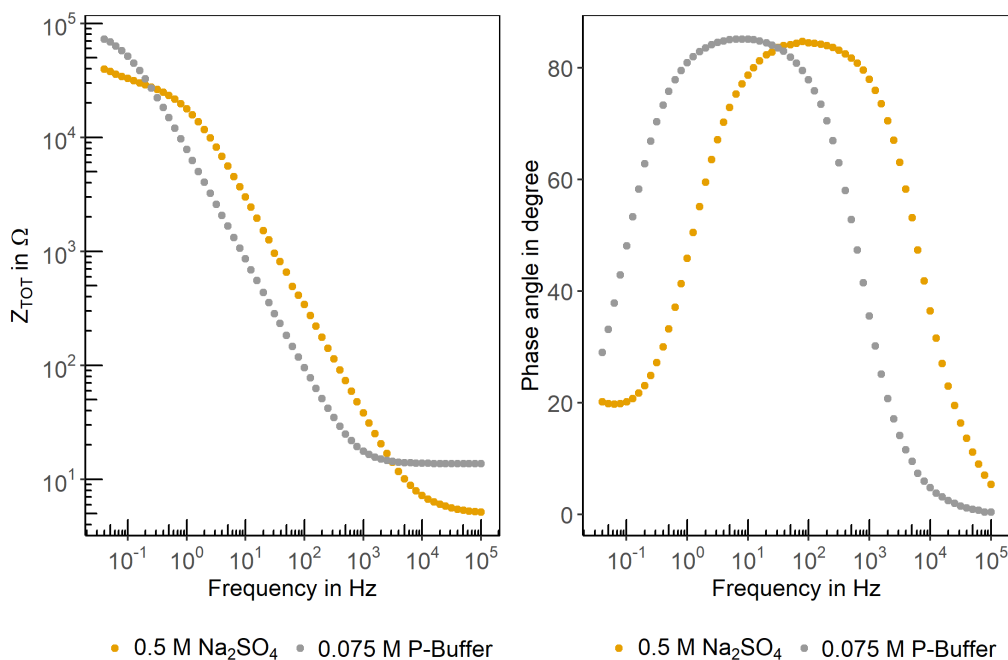


FIGURE 4.24: Bode plot of EIS analysis in the flow cell with 10 mM $\text{K}_4[\text{Fe}(\text{CN})_6]$ in Na_2SO_4 (in orange) and in 0.075 M phosphate buffer (in grey) (at +0.2 V vs. SHE).

Impedance was analysed anoxic with 10 mM $\text{K}_4[\text{Fe}(\text{CN})_6]$ as redox probe at frequencies ranging from 100 kHz to 50 mHz. The electrolytes used were first 0.5 M Na_2SO_4 with a high conductivity, and second 0.075 M phosphate buffer which has a similar conductivity to the medium used in MFC experiments, thereby mimics the system's resistance best. The exact MFC medium could not be used for EIS analysis since the redox probe would precipitate in the carbonate buffer, hence phosphate buffer with the same osmolarity was used as substitute.

Bode plot and Nyquist plot are shown in Figures 4.24 and 4.25, with the result in Na_2SO_4 in orange and in phosphate buffer in grey. Curve characteristics were as expected for the Fe(II)/Fe(III) redox pair and similar to the characteristics of the flow cell described in [149]. In Na_2SO_4 the semicircle in the Nyquist plot shows the beginning of a Warburg diffusion line which indicates a kinetically controlled reaction at high frequencies and diffusion control at low frequencies [197], as expected for the redox couple Fe(II)/Fe(III) [197]. This line is not present in phosphate buffer due to a higher resistance of the electrolyte. R_{CT} was calculated from the fit to a Randles equivalent circuit (see Figure 1.8) with 25.4 k Ω in Na_2SO_4 and as expected a higher resistance with 77.7 k Ω in phosphate buffer.

Concluding, the flow cell with the facilitated electrode mounting and contacting and with slightly altered geometry was electrochemically functional. Sealing the electrode with silicone was still necessary to avoid contact between the Pt frame and the anolyte, which would interfere with EIS measurements and with polarisation of the electrode. This manual sealing should in general be omitted as it makes the available electrode surface less reproducible among experiments.

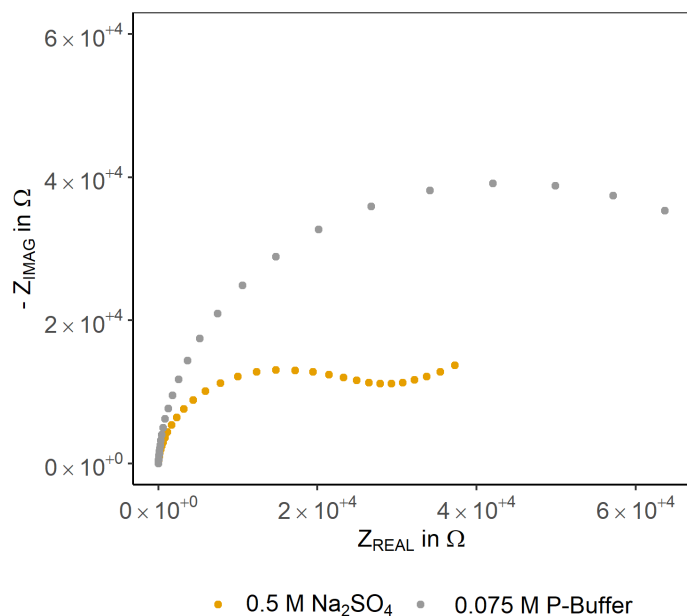


FIGURE 4.25: Nyquist plot of EIS analysis of ITO WE in the flow cell with 10 mM $K_4[Fe(CN)_6]$ in Na_2SO_4 (in orange) and in 0.075 M phosphate buffer (in grey) (at +0.2 V vs. SHE).

4.7.3 MFC in flow cell with *G. sulfurreducens* mCh

After abiotic characterisation of the flow cell, MFC experiments were conducted with the fluorescent strain as described in section 3.9.3. Unfortunately, no current production was observed initially, even though fumarate was added to the WE reservoir and the WE was polarised to the identified optimum potential of 0 V vs. SHE. To exclude that this was solely a problem of the recombinant strain, the WT was inoculated to the identical setup, at a potential of +0.1 V vs. SHE (which was identified as favourable for the WT in section 4.5), but again (almost) no current was produced. The little current recorded (approx. 100 nA) is shown in the Appendix in Figure A.4. This indicated an attachment problem that might be caused by the positioning of the electrode. In H-cells the electrode is positioned vertically in the reactor and also in an area with slightly reduced flow due to the attached flange. In the flow cell the electrode is placed vertically on top of the WE chamber, fully exposed to the flow. In the following, higher, as well as lower flow rates than the usually used 0.5 ml/min were tested, also the flow was stopped after the bacterial solution was distributed throughout the system to allow initial attachment to the electrode. However, still no current production and no change in EIS, that would indicate bacterial attachment, could be detected.

To test if current was produced when the attachment was facilitated, the flow cell was rotated by 180° about the longitudinal axis so the WE was now the lowest point of the system. This WE position is designated as *down-under* in the following. With this positioning current production could be detected at 0 V vs. SHE with *G. sulfurreducens* mCh. Recorded current density over time is shown in Figure 4.26 together with WE charge transfer resistance R_{CT} calculated from the fit to a Randles equivalent circuit. Current density in this experiment was $19 \mu A cm^{-2}$ with a start-up time of 8.5 h and the curve shape characteristic for *G. sulfurreducens* MFC, i.e. with a peak and a linear

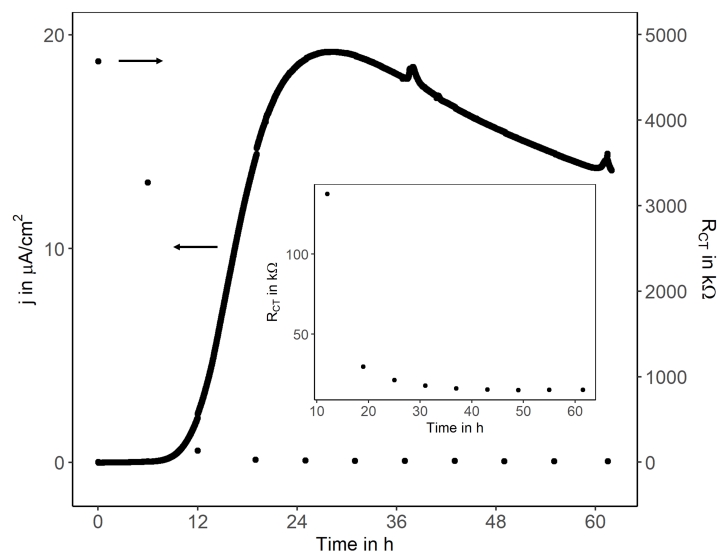


FIGURE 4.26: Current (black line) and fitted R_{CT} (filled dots) over time of *G. sulfurreducens* mCh in the flow cell down-under with a maximum current of $19 \mu\text{A cm}^{-2}$. For better visualisation the insert shows R_{CT} after current production could be detected (12 h).

TABLE 4.8: Maximum current density, start-up time, time until maximum current was reached and biofilm thickness for a biological triplicate of flow cell experiments in *down-under* mode.

Exp	Max j in $\mu\text{A cm}^{-2}$	Start-up time in h	Time max current in h	Biofilm thickness in μm
1	19	8.5	28.5	26 ± 13
2	4	7.7	19.1	27 ± 11
3	9	10.9	31.7	29 ± 14

decrease in produced current afterwards. R_{CT} was initially very high ($4.7 \text{ M}\Omega$) but decreased rapidly within 12 h to $140 \text{ k}\Omega$. No current was detected at this time point. The insert in Figure 4.26 shows R_{CT} after 12 h when current production set in. At maximum current production ($19 \mu\text{A cm}^{-2}$) R_{CT} was $21.3 \text{ k}\Omega$, towards the end of the experiment it was further reduced to $15.2 \text{ k}\Omega$, however the largest reduction in R_{CT} took place in the first 12 h of the experiment. What must be noted is that accuracy of the fit to the electrical equivalent circuit increases with decreasing R_{CT} , hence the first three fitted data points have a high uncertainty. When fitting the equivalent circuit, the half circles (seen in the Nyquist plot in Figure 4.27) are extrapolated towards the x-axis to determine the system's resistance and the larger the half circle the higher the uncertainty of the fit to the circle. Nevertheless, the analysed trend (of decreasing resistance during current production) remains valid, which is supported by the decreasing half circle diameter in Figure 4.27). The insert enlarges the measuring range after 19 h.

To assess the reproducibility of the *down-under* mode two additional experiments were conducted; the results are summarised in Table 4.8. Maximum current densities

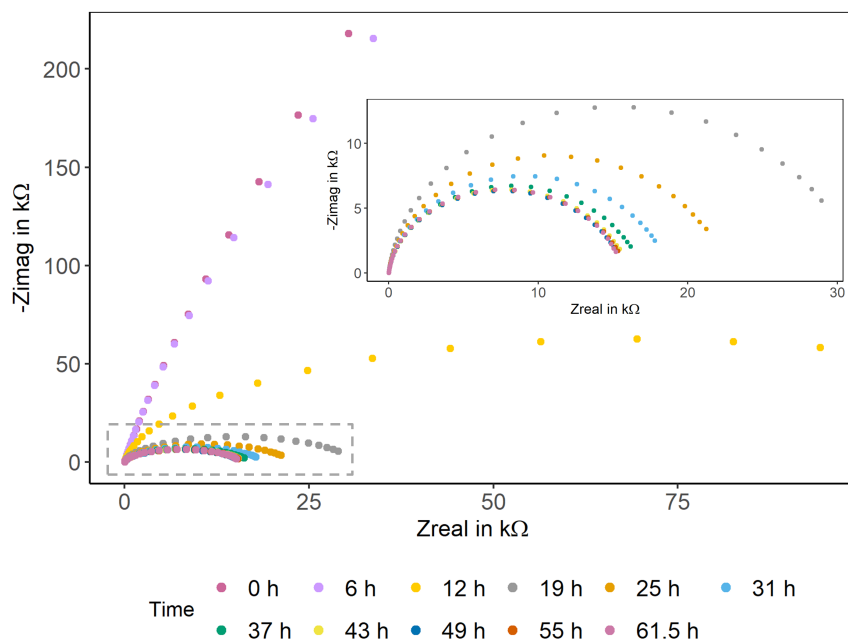


FIGURE 4.27: Nyquist plot of periodic *G. sulfurreducens* mCh EIS analysis in flow cell *down-under*. Insert enlarges the measuring range after 19 h. Note that in the plot that shows the whole measuring range the x- and y-axis have different scaling.

achieved were 19, 4 and $9 \mu\text{A cm}^{-2}$, with start-up times of 8.5, 7.7 and 10.9 h. Also the time until maximum current density was reached varied greatly (from 19.1 to 31.7 h) but was proportional to the length of the start-up time (the experiment with the longest start up time took the longest to reach maximum current). The start-up time was (slightly) shorter than in H-cell experiments on ITO electrodes at 0 V vs. SHE ($12.4 \text{ h} \pm 2.7 \text{ h}$, $n = 4$), most probably since the cells sink to the electrode automatically, which facilitated cellular attachment. Since cells easily settled on the electrode, biofilms grew very heterogeneous in height (within-biofilm heterogeneity). This was reflected in the high SD in biofilm thickness calculation, with close to 50 % for all three experiments. A representative CLSM image of a biofilm grown in the flow-cell in *down-under* mode is shown in Figure 4.28 (A). The z-representation showed a ripply surface with mushroom-like structures on top of a basal cell layer.

In order to test whether this structure was significantly connected to the electrode or only loosely attached, the flow cell was turned upright once current production started, in a consecutive experiment. A CLSM image of the resulting biofilm is displayed in Figure 4.28 (B). The biofilm is significantly thinner compared to the biofilm when the flow cell was operated *down-under* entirely. Biofilm thickness was calculated with $11 \mu\text{m}$, however with an SD of 100 % due to a still uneven biofilm structure. Current and R_{CT} over time for the turned-around flow cell are shown in Figure 4.29 with the insert displaying R_{CT} after 24 h experiment run time. The dashed arrow marks the time the flow cell was turned upright (22 h). Current production reached a steady-state level in this experiment (in contrast to the experiments in which the flow cell was operated in *down-under* mode entirely) with constant current production for approximately 40 h at $4 \mu\text{A cm}^{-2}$. R_{CT} dropped sharply within the first 12 h from $1.5 \text{ M}\Omega$ to $240 \text{ k}\Omega$, as described for the previous experiments, but slightly

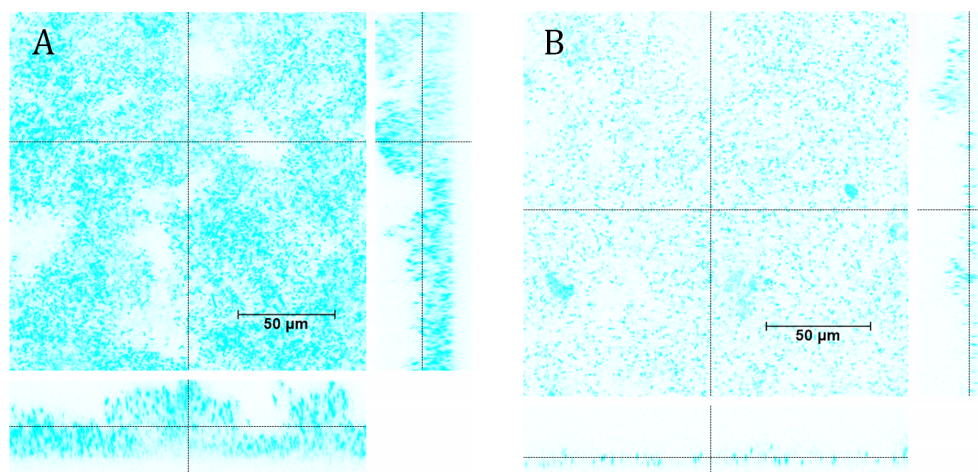


FIGURE 4.28: CLSM images of *G. sulfurreducens* mCh biofilms in the flow cell (mCherry fluorescence displayed). (A) was grown entirely in *down-under* mode and the biofilm in (B) was initially grown in *down-under* mode and turned upright after 22 h (current curves are shown in Figure 4.26, respectively 4.29).

increased again after 60 h incubation time (from 34 to 42 k Ω). This might be caused by biofilm deterioration, which is also resembled in decreasing current.

Regardless of the little current produced, operating the flow cell *down-under* to facilitate cellular attachment, and subsequently turning it upright to allow CLSM analysis, seemed an appropriate operation procedure.

Biofilms of previous experiments were imaged after detaching the electrode from the flow cell as the flow cell was not operated in the CLSM setup but in an incubator hood. In the following, the anode was not detached but the whole flow cell (including the tubing) moved to the CLSM and the biofilm imaged with a 63x-water immersion objective. Figure 4.30 (A) shows the CLSM image of a biofilm that had not been exposed to oxygen prior to imaging, and obviously the appearance is rather different compared to the same biofilm after it was removed from the flow cell and kept under air for about 3 min (shown in (B)). Apparently, fluorescence is considerably brighter and more homogeneous after air exposure. In (A), when no air had entered the flow cell yet, only clusters of biomass emitted a fluorescence signal, thereby preventing any analysis. As the strain was described for application in an anaerobic flow cell [148], even though the chromophores derived from DsRed require two oxidations for maturation [198], fluorescence properties were not questioned before - yet oxygen exposure seemed to be a limiting factor for proper fluorescence.

The flow cell was consecutively tested with *G. sulfurreducens* WT using the described operation procedure. The experiment was started *down-under* and the cell turned over after 17 h, leading to a maximum current density of 196 $\mu\text{A cm}^{-2}$. At the applied potential of +0.1 V vs. SHE this was about half the current density reached in an H-cell but underlines that the low current density in the experiment with *G. sulfurreducens* mCh can be attributed to the strain and not to the flow cell. Current density over time is shown in the Appendix in Figure A.5.

Summarised, the results showed that the modified electrochemical flow cell, based on the system developed in [149] with *Shewanella oneidensis*, could also be applied

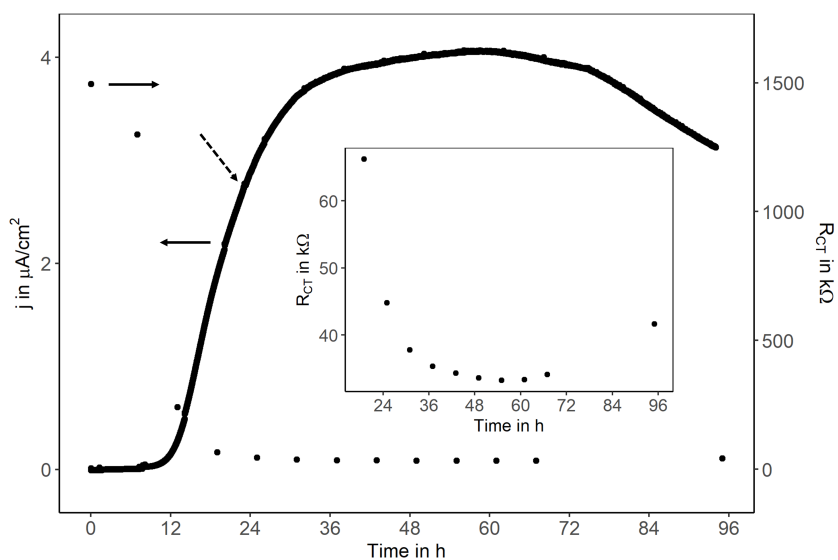


FIGURE 4.29: Current density (solid line) and R_{CT} (black dots) over time of *G. sulfurreducens* mCh in a flow cell that was started *down-under* and turned upright after 22 h operation time (dashed arrow). The insert shows R_{CT} after 24 h for better visibility.

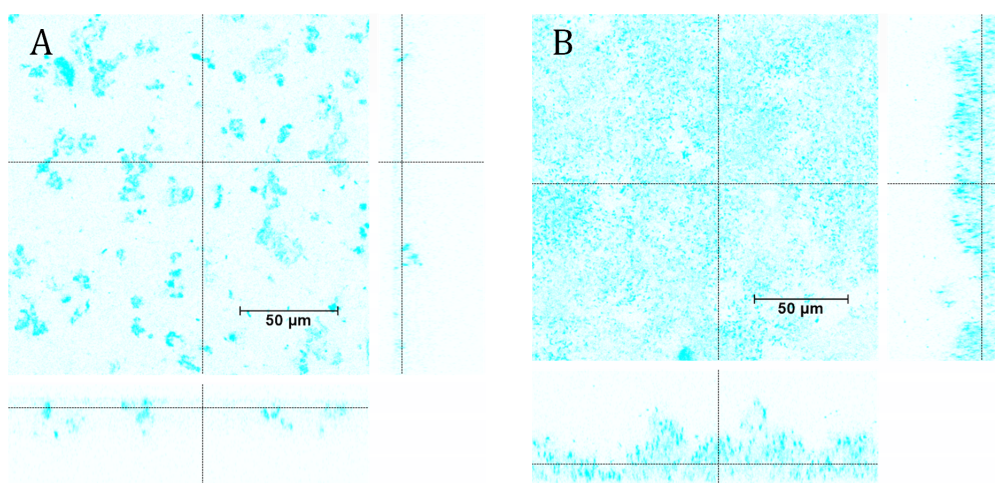


FIGURE 4.30: A *G. sulfurreducens* mCh biofilm grown in a flow cell in *down-under* mode was analysed with the CLSM with a 63x water immersion objective when the WE was still mounted to the flow cell (A) and with a 63x dip-in objective after removal of the WE and air exposure for approximately 3 min (B) (mCherry fluorescence displayed).

with EAB relying on direct electron transfer, such as *G. sulfurreducens*. However, it turned out that in the upright position cells would not interact with the electrode. This was observed independently of the flow rate and might be caused by the very smooth surface of ITO that has almost no 3D structures which would support bacterial adhesion. This is in contrast to *S. oneidensis* which showed current response also in the up-right positioned flow cell and at high flow rates of 5 ml/min. *S. oneidensis* however does not rely on direct contact with the electrode but also secretes mediators that serve as electron shuttles between the cell and the electrode [47].

In most electrochemical reactors, as in H-cells, the electrode is positioned vertical inside the WE chamber [11] which facilitates attachment in comparison to the horizontal positioning on top of the chamber at which flow and gravity counteract cellular adhesion. Continuously operated reactors are often equipped with textile-like carbon materials with high surface that allow attachment against the flow velocity (examples in [11]). In [199] recent advancements on microfluidic MFC were reviewed but none of the described set-ups were designed for *in situ* biofilm analysis. The only comparable example of a microfluidic MFC with *G. sulfurreducens* pure cultures is the one used by Franks et al. [148, 154, 200]. It operates with a graphite WE that is placed in 0.5 mm distance to a coverslip through which the biofilm can be imaged. Unfortunately, no information is available about the positioning of the flow cell during operation, respectively the orientation of the anode or its fastening in the WE chamber. Nevertheless, the advantage of the Franks system is that no transparent electrode material is necessary, respectively any electrode material can be tested, accompanied by *in situ* biofilm analysis.

However, also in this application required a fluorescent strain, which in turn requires genetic modification. Even though only one reporter gene has to be introduced, significant changes in the phenotype that also affect current production, can be the consequence. The need of a fluorescent protein inherits another problem in connection with anaerobic organisms. GFP and DsRed related proteins require oxygen for chromophore maturation [198, 201], actually. It remains unclear how (and why) the group of Franks et al. successfully applied *G. sulfurreducens* mCh in an anaerobic microfluidic MFC and why in turn fluorescence was impaired in the microfluidic system used in this work. From a theoretical point of view, the named fluorescent proteins and their derivatives are not suitable for the application as fluorescence marker in anaerobic microfluidic MFC, which narrows down the possibilities for those systems significantly. Progress has been made on this topic, e.g. with LOV based fluorescent proteins (light, oxygen and voltage sensing proteins) that use flavin as their photoactive cofactor or bilin-binding fluorescent proteins but none of those have been tested with EAB yet [202].

An alternative microscopic method (that does not require fluorescence) is phase contrast microscopy as applied in a microchannel MFC in [203] but that does not allow quantitative analysis. Or CLSM analysis can be used in reflection mode but this method requires a non-biofilm covered reference point on the electrode which is hardly feasible in real-time analysis [94].

Considering this, microscopic *in situ* biofilm analysis on EAB that require an anaerobic environment remains a laborious task.

4.8 *G. sulfurreducens* metabolite analysis

Fumarate is frequently used as soluble TEA in *G. sulfurreducens* growth medium, but is usually omitted in MFC experiments in order to channel electrons exclusively to the electrode. *G. sulfurreducens* mCh however had to be “kick-started” with an initial amount of fumarate in the anolyte in order to produce current at all. Also, fumarate was added to the WE reservoir in flow cell experiments to maintain cell viability until the cells had attached to the electrode as alternative electron acceptor. In the following experiments, acetate/fumarate metabolisation of *G. sulfurreducens* WT was studied by varying donor/acceptor ratios in order to gain insight into the metabolite ratio during growth. The ratio proposed in the DSMZ medium recipe is 1:5 (acetate:fumarate), even though the theoretical ratio is 1:2 as described in 1.2.2. Therefore, growth and metabolism were monitored at combinations 10 mM acetate : 25 mM fumarate and 10 mM acetate : 50 mM fumarate. The results presented here we published in [204].

4.8.1 Donor/acceptor ratio 1:2.5

Growth curves of a biological triplicate with 25 mM fumarate and 10 mM acetate were monitored over 60 h. Growth curve and metabolite concentrations are shown in Figure 4.31. Growth parameters are summarised in Table 4.9.

With a donor/acceptor ratio of 1:2.5 the growth rate was $0.19 \pm 0.05 \text{ h}^{-1}$, with a maximum calculated doubling time of $3.69 \pm 0.06 \text{ h}$. With initiation of the exponential growth phase fumarate was consumed at a linear rate of $-0.87 \pm 0.01 \text{ mM h}^{-1}$. At the same time succinate concentration increased at an exponential rate of $1.09 \pm 0.003 \text{ mM h}^{-1}$. The carbon and electron source acetate was consumed at $-0.36 \pm 0.02 \text{ mM h}^{-1}$. Fumarate was consumed faster than acetate even though acetate was the only electron source for fumarate reduction. Together with succinate as product of fumarate reduction malate was produced as intermediate. Its maximum concentration was reached after approximately 24 h of cultivation; until then the linear production rate was $0.19 \pm 0.003 \text{ mM h}^{-1}$. Afterwards, malate was consumed and metabolised to the final product succinate via the citric cycle. At the end of the cultivation the ratio of fumarate consumed and succinate produced was approximately 1:1.

4.8.2 Donor/acceptor ratio 1:5 and acetate feed

When fumarate was added in excess, malate accumulation was faster with a rate of $0.28 \pm 0.01 \text{ h}^{-1}$ and accumulated to a maximum concentration of 17 mM, in comparison to 5 mM accumulated malate when only 25 mM fumarate were available initially. Also malate accumulated continuously now and not transiently (Figure 4.32). After the culture reached stationary growth phase, 10 mM acetate were added to monitor malate uptake in presence of an electron (and carbon) source. The first growth phase (until 60 h) followed logistic growth as seen in Figure 4.31, the one after fresh acetate was fed seemed to follow a limited growth model. Growth rate for the first growth term was $0.23 \pm 0.01 \text{ h}^{-1}$ with a maximum calculated doubling time of $3.05 \pm 0.09 \text{ h}^{-1}$, which was slightly faster than growth with 25 mM electron acceptor (Table 4.9 for comparison). Acetate and succinate metabolisation were at similar rates compared to growth with a 1:2.5 donor/acceptor ratio, hinting to an enzyme saturation already with 25 mM fumarate available (ac: $-0.37 \pm 0.01 \text{ h}^{-1}$, succ: $1.08 \pm 0.00 \text{ h}^{-1}$). Fumarate was metabolised at a faster rate with $-1.23 \pm 0.03 \text{ h}^{-1}$ which correlated with the faster malate accumulation. When acetate was available again,

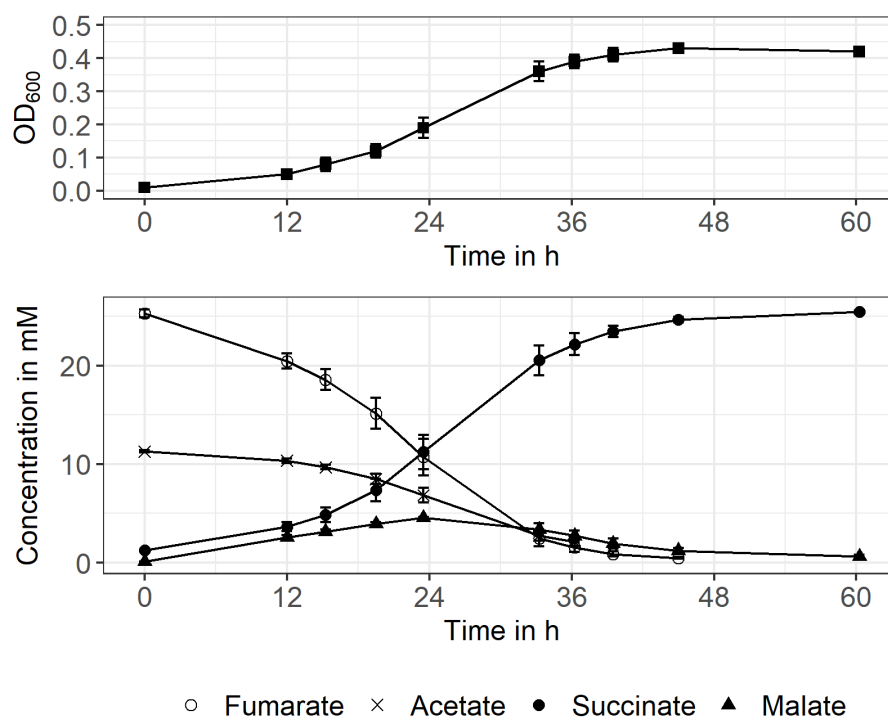


FIGURE 4.31: Mean values for OD₆₀₀ and metabolite concentration are shown over time when cultivating *G. sulfurreducens* with 10 mM acetate and 25 mM fumarate. Error bars show SD for n=3.

TABLE 4.9: Growth parameters for two different electron donor/acceptor ratios. Values are given as mean \pm SD of a biological triplicate.

Donor/acceptor ratio	1 : 2.5	1 : 5
Growth rate in h ⁻¹	0.19 \pm 0.05	0.23 \pm 0.01
Doubling time in h	3.69 \pm 0.06	3.05 \pm 0.09
Fum consumption rate in mM h ⁻¹	-0.87 \pm 0.01	-1.23 \pm 0.03
Succ production rate in mM h ⁻¹	1.09 \pm 0.003	1.08 \pm 0.00
Ac consumption rate in mM h ⁻¹	-0.36 \pm 0.02	-0.37 \pm 0.01
Mal production rate in mM h ⁻¹	0.19 \pm 0.003	0.28 \pm 0.01

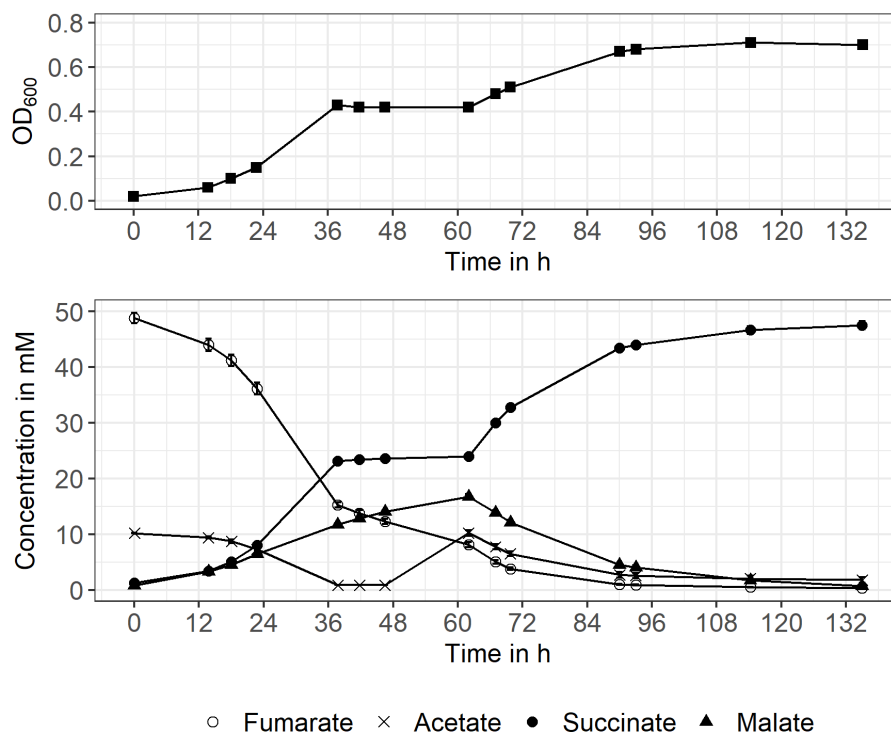


FIGURE 4.32: Mean values for OD₆₀₀ and metabolite concentration are shown over time when cultivating *G. sulfurreducens* with excess fumarate. Error bars show SD for a biological triplicate. SD was below 2% for all measuring points, therefore error bars are not visible for all data points. 10 mM acetate were added to the stationary culture after 60 h of cultivation.

malate concentration decreased immediately and cell growth resumed, but only to 80% of the OD₆₀₀ that was expected possible with 20 mM acetate in total (theoretical OD₆₀₀ circa 0.84, actual OD₆₀₀ 0.7).

4.8.3 Fumarate conversion by stationary cells

In order to test the activity of fumarase and malate transporter of resting cells, 35 mM fumarate were added to a stationary culture (OD₆₀₀ 0.43) and incubated without carbon or electron source. In Figure 4.33 the conversion of fumarate to malate can be seen, following a classical limited conversion model, shown in equation 4.1, with x as time in hours and parameter b positive for fumarate concentration kinetics and negative for malate kinetics. With $0.047 \pm 0.004 \text{ mM h}^{-1}$ the consumption rate of fumarate was approximately equal to malate production ($-0.050 \pm 0.005 \text{ mM h}^{-1}$), as also seen by the symmetry of the graphs in Figure 4.33. In 54 h 25 mM fumarate were converted to 21 mM malate, which equals an 85% conversion, before saturation was reached.

The discrepancy to a full conversion might primarily be caused by deviations in HPLC analysis and additionally by remaining acetate stored inside the cells that served as electron source to metabolise malate further. The continuous depletion of fumarate indicated that fumarase acted independently of the following malate conversion towards the TCA. That makes the malate concentration in the medium

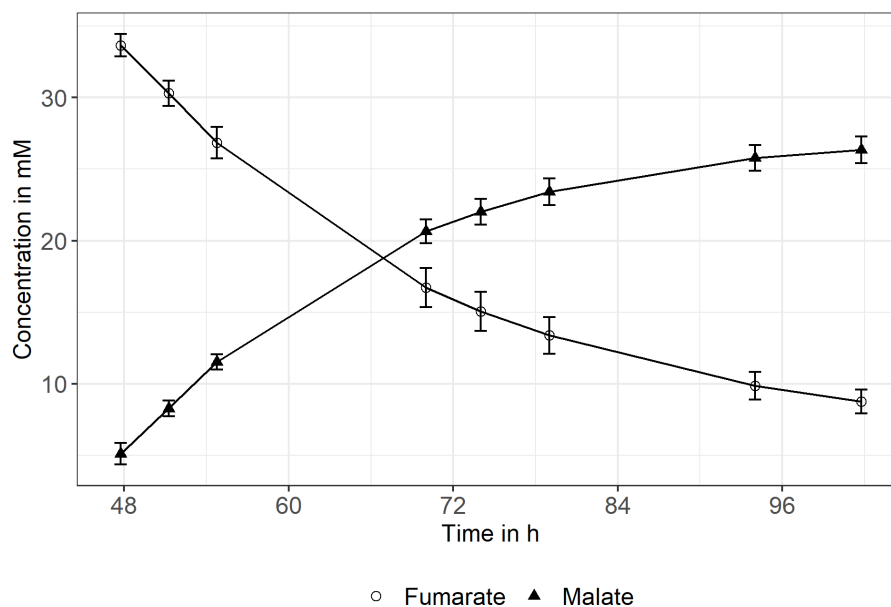


FIGURE 4.33: 35 mM fumarate were added to a culture of stationary *G. sulfurreducens* cells and the conversion to malate analysed. Shown are mean and SD of a biological triplicate.

the primary indicator when assessing whether soluble electron acceptor is available for the organism (and not the remaining fumarate).

$$f(x) = a + b \cdot e^{(-k \cdot x)} \quad (4.1)$$

The transient malate accumulation was also observed in [74] and [73] and explained with the thermodynamically unfavourable oxidation from malate to oxaloacetate in the TCA (see Figure 1.4 A). In order to still shift the equilibrium towards oxaloacetate, malate is accumulated by the faster reaction of fumarase, converting fumarate to malate [73]. This effect is more pronounced the higher the fumarate excess as also seen in this work (malate production rate $0.28 \pm 0.01 \text{ mM h}^{-1}$ with donor/acceptor ratio 1:5 and $0.19 \pm 0.003 \text{ mM h}^{-1}$ with ratio 1:2.5).

While this phenomenon has no major relevance in planktonic growth, it should be kept in mind for MFC experiments. In case fumarate is added at the start of the experiment, e.g. to retain cell viability in the starting phase of a continuous system (as in this work or in the work of Franks et al. [148, 154, 200]), it is not sufficient to only monitor fumarate concentration. To precisely determine the time point at which no soluble electron acceptor is available any more, both fumarate and malate concentrations should be analysed. Otherwise, long start-up times might be mistaken for a bioelectrochemical effect, even though it is caused by remaining malate that is still used as electron acceptor instead of electrons being transferred to the electrode.

Chapter 5

Conclusion and Outlook

A comfort zone is nothing easy to find and so it was when engineering electrode surfaces in MFC with *G. sulfurreducens* as model organism. Conclusions from the conducted work will be discussed in the following.

5.1 Analytical method development

Two new methods were (further) developed in this work: The use of the HR-SKP to determine surface potential of coated electrodes and the measurement of biofilm thickness from CLSM z-scans with an R-script.

The HR-SKP was successfully established to measure the surface potential of coated (and non-coated) graphite and ITO electrodes; in absence of a specialised device for this purpose. The surface potential of the used polymers could be ranked as follows (from highest to lowest potential): PSS > ALG > ITO \approx Graphite \approx CHI \gg PEI. In contrast to XPS [170] or Raman microscopy [171] the HR-SKP does not detect the functional groups of the polymer but the change in surface potential which is the actual factor having influence on electrostatic interaction in the end. Ideally, two methods are combined to gain complementary information on potential electrostatic forces, as well as H-bonds or Van der Waals forces caused by interaction between the cell wall and functional groups of the polymers. What also combined methods cannot cover is a realistic view of the surface composition after incubation in medium, on a poised electrode, and even more difficult, after inoculation with bacteria/any type of wastewater sludge. Not only all sorts of medium components but also molecules secreted by the cells, such as DNA, proteins or humic substances will interact with the surface modifications. This plot makes the story of investigating surface modification far more complex than it is modelled in the lab where it is broken down to single influencing factors.

The thickness of biofilms formed on the anode is an important MFC performance indicator but is mostly only measured qualitatively and without stating the size of the underlying data set. Therefore, a quantitative method was developed that allowed the analysis of any number of regions on the biofilm with little hands-on work. Output is a mean biofilm thickness and a value for SD that indicates the homogeneity of biofilm growth: the more uniform the biofilm thickness across the whole biofilm, the smaller SD of the analysis.

The recently published software package "BiofilmQ" [205] also covers biofilm thickness calculation, among a vast number of other functions, and might be oversized for some applications. For the script developed in this work no image correction has to be performed (if some notes on image acquisition regarding laser intensity are followed). Further "BiofilmQ" is based on Matlab, so if there is an existing R routine the stand-alone script from this work could easily be integrated. Hence, if

only biofilm thickness should be determined, the developed R-script is a valuable alternative to the tool available with "BiofilmQ".

5.2 MFC reactor system

In general, comparison between different MFC systems is only informative to a limited extent due to the variability in reactor construction, electrode material, operating parameters etc., as elaborated in section 1.1. All the more important it is to define an internal standard to which the effect of electrode surface modifications can be compared. PalmSens and MaterialMates multi-potentiostats in combination with graphite electrodes were found to introduce equally high SD in all performance parameters, making it complicated to extract any significant difference potentially caused by the coatings. ITO electrodes in combination with IPS and Gamry potentiostats reduced SD, at least for the start-up time, which was thought to be most impacted by the surface modification. Additionally, it turned out that current response depended significantly on the applied potential, adding a parameter that must be kept constant in order to compare MFC experiments among themselves. Finally, the results at +0.1 V on ITO were defined as benchmark values for comparison with coated electrode surfaces.

Even though it would be beneficial for MFC research, it is impossible to standardise MFC systems due to the diverse applications that require certain electrode geometries, textures, reactor constructions, media compositions and bacterial communities. Therefore, it is essentially important to a) identify the optimum potential for the used bacteria in the given system beforehand and b) to produce a benchmark value in the non-modified system, and determine the corresponding statistical insecurities for all relevant parameters, in order to at least be able to compare any modifications to the system itself, if not to others.

5.3 MFC performance depending on chemical surface properties

Contrary to expectations, a positive surface charge did not imply improved performance indicators for pure culture *G. sulfurreducens* MFC in this work. In contrast, negatively charged PSS as closing layer produced the best results, but also not significantly better than non-coated ITO electrodes. For all coatings except ALG- EIS measurements excluded an electrochemical cause for the results, so the beneficial effect of positive surfaces, that was reported elsewhere, could not be transferred to the system used. It is conceivable that not only the charge influenced the observed results but also the side chains present on the polymers, as already touched upon for tertiary amines present in PEI. Following this, SO_3^- would support *G. sulfurreducens* adhesion preferably over NH_2/OH^- functional groups present in CHI. Referring to the interaction of the coating with medium components (as discussed in section 4.6) it is most important to measure coating properties in a realistic environment. Also here, standardisation between different MFC systems is fairly difficult. The positive effect of surface modifications was seldom analysed decoupled from an increase in available electrode area, which might overestimate the potential of surface modifications. Currently, an increase in electrode surface seems to be the more promising attempt as this approach seems to have a circa proportional effect on current production, and is thus more predictable compared to the effect of surface modifications.

5.4 The bioelectrochemical flow cell and *G. sulfurreducens* mCh

In situ biofilm analysis should be the path to follow in order to gain further insight into bacterial adhesion and possibilities to improve MFC performance from an electrode perspective. CLSM analysis is a powerful method but requires a fluorescent strain, which may provoke complications, especially under anaerobic conditions, as seen in this work. Alternatives that are not based on optical methods are Raman spectroscopy or torsional resonators (an advancement of QCM as described in [206]). The first allows chemical analysis of the biofilm (e.g. cytochrome analysis over time as in [100]), the latter the rigidity/elasticity of the film, of which a conclusion on biofilm thickness and cellular adhesion can be drawn in return (but not about homogeneity of surface coverage for example). None of the methods as a stand-alone is sufficient to characterise biofilm-coating interaction, so a combination of two methods such as CLSM-EIS is promising in principle - if the problem about the fluorescence can be overcome.

5.5 The potential of MFC

Just as other regenerative energy sources MFC can and should contribute to the transformation of the energy sector towards the circular use of resources. It is a multivariate system though, with additional variables to consider, compared to a solar panel or a wind power plant, since it is based on living organisms. Besides the technical points to consider like reactor scale-up, electrode material or electrochemical efficiency also the bacterial community and the interplay of bacteria and material is essential in order to develop an application that can make a net positive contribution to how we generate energy. If surface modifications should be investigated further it might be worth changing the direction of thinking and rather simulate cell-surface interaction mathematically than trying it out in costly wet-lab experiments. Mathematical models that describe bacteria-surface interaction have been increasingly researched and might be a more efficient tool to investigate the interplay of various influencing factors instead of trying to separate those factors artificially in the laboratory [84, 87, 207]. This work scratched on the surface of how complicated it is to address the interplay between bacteria and material and trying to sneak into that blackbox. Instead of proceeding with trial and error approaches and get lost in trifles it might be time to work on a more holistic model and tackle that problem from a new direction.

Appendix A

Appendix

A.1 Fluorescent polyelectrolytes in microplate reader

A serial dilution of Rhodamin-labelled PEI was measured in a microplate reader to determine the lower detection limit of the measurement. According to the manufacturer, the emission maximum of the fluorescently labelled polyelectrolyte is at 582 nm, which corresponds to the data measured in the plate reader (compare top left in Figure A.1). The peak at 580 nm is present for concentrations down to 1 mg l^{-1} until salts from the buffer with emission between 620 and 660 nm become more prominent. The lower detection limit was identified as 1 mg l^{-1} .

Both H-cells were sampled after 22 h, 86 h and 111 h and an emission scan recorded, together with a medium sample as negative control. Mean and SD (shaded area) of technical triplicates for all time points are shown in Figure A.2. It can be seen that the samples from both H-cells do not differ from the negative control.

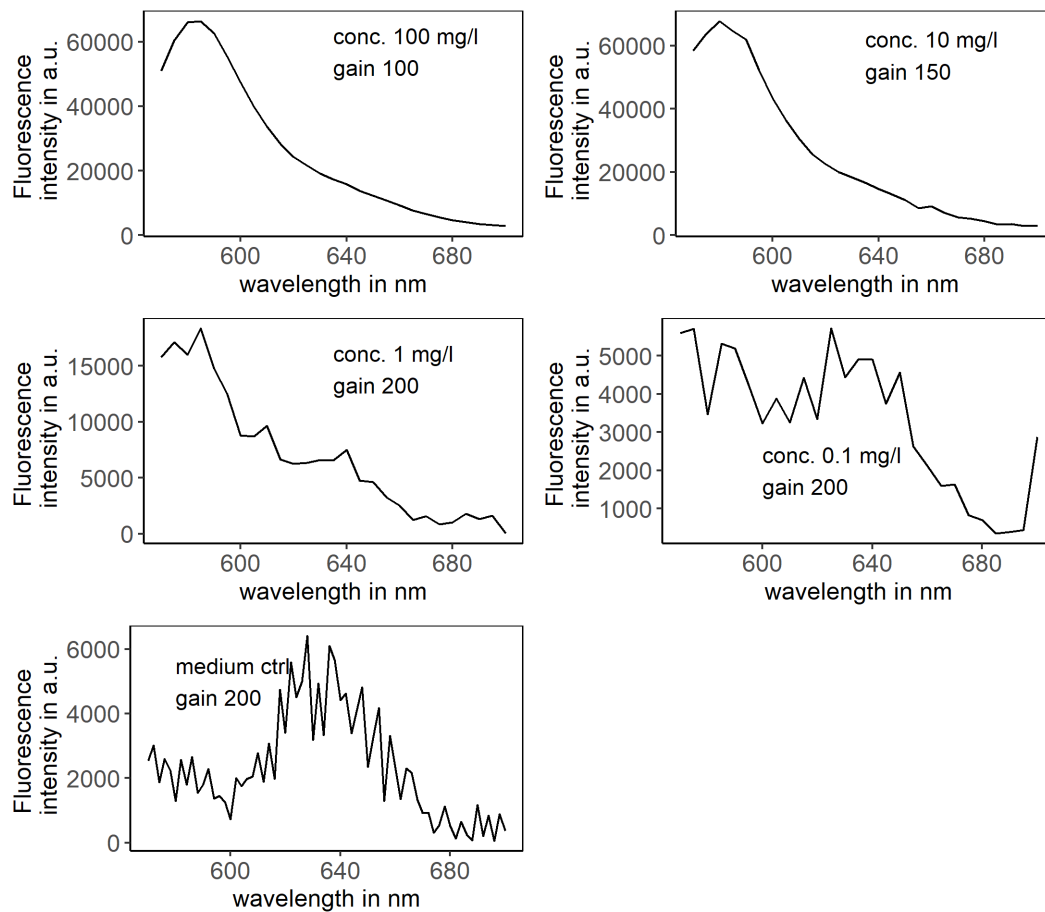


FIGURE A.1: Fluorescence signal of a serial dilution of PEI-Rho was measured in a microplate reader to determine the lower detection limit. The concentrations 100 mg l^{-1} , 10 mg l^{-1} , 1 mg l^{-1} , 0.1 mg l^{-1} and a medium control are shown.

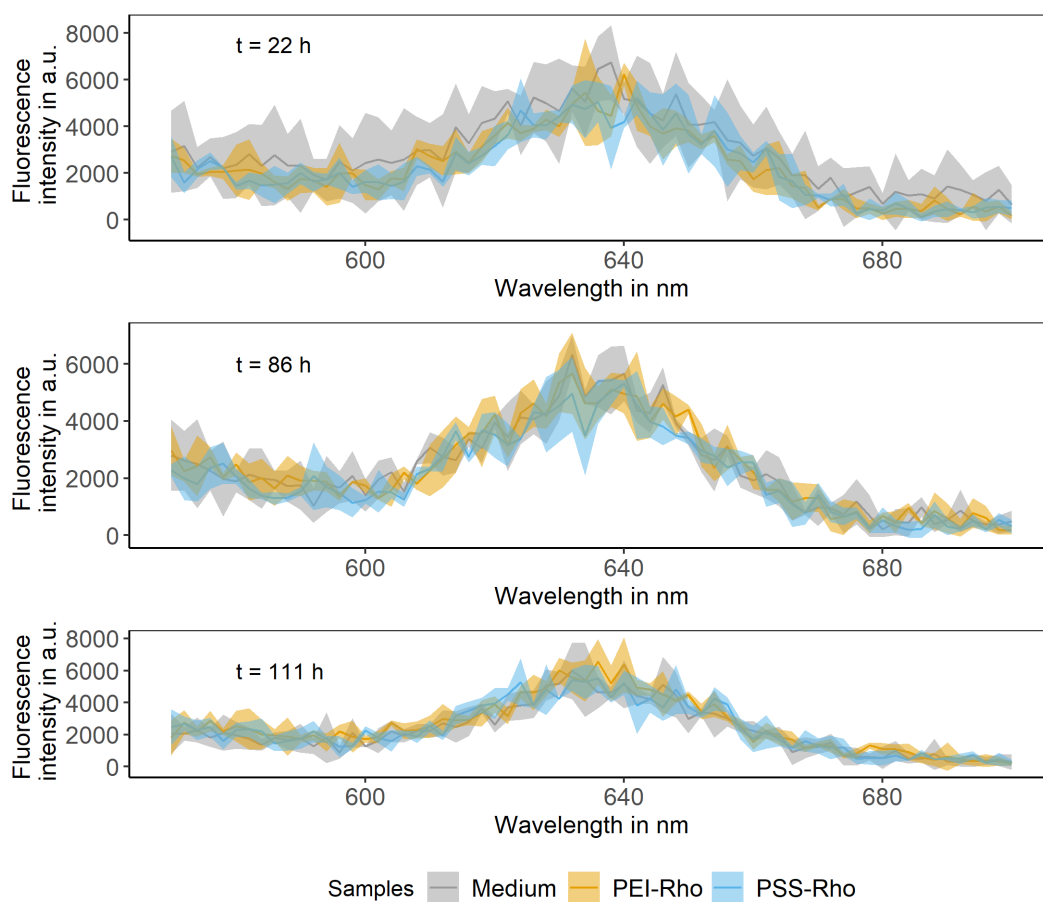


FIGURE A.2: Mean and SD (shaded area) of technical triplicates of microplate reader measurements of WE chamber samples are shown. From top to bottom: sampling after 22 h, 86 h and 111 h. For each timepoint H-cell medium was measured as negative control.

A.2 Correlation of parameters for MFC on ITO

Pearson coefficients were calculated for correlation among performance indicators and applied potential (experiments on ITO). The lower triangle of the correlation matrix is shown in Table A.1. A linear correlation was extracted for current density ~ biofilm thickness ($p < 0.0001$), $\eta_C \sim$ lag phase ($p < 0.001$) and $\eta_C \sim$ biofilm thickness ($p < 0.001$).

TABLE A.1: Pearson correlation coefficients for correlation among MFC performance indicators and applied potential. **** $p < 0.0001$, *** $p < 0.001$, ** $p < 0.01$, * $p < 0.1$

	Applied potential	Maximum current density	Lag phase	Biofilm thickness	η_C
Applied potential					
Maximum current density	0.47*				
Lag phase	0.70**	0.05			
Biofilm thickness	0.19	0.79****	-0.40		
η_C	-0.26	0.55*	-0.72***	0.74***	

A.3 Growth comparison *G. sulfurreducens* WT and mCh

OD₆₀₀ and metabolite concentration over time were compared between *G. sulfurreducens* WT and *G. sulfurreducens* mCh. Results are shown in Figure A.3 with WT in grey and mCh in orange. No major differences in both growth and in the metabolites analysed could be detected that would explain the large differences between both strains in MFC performance.

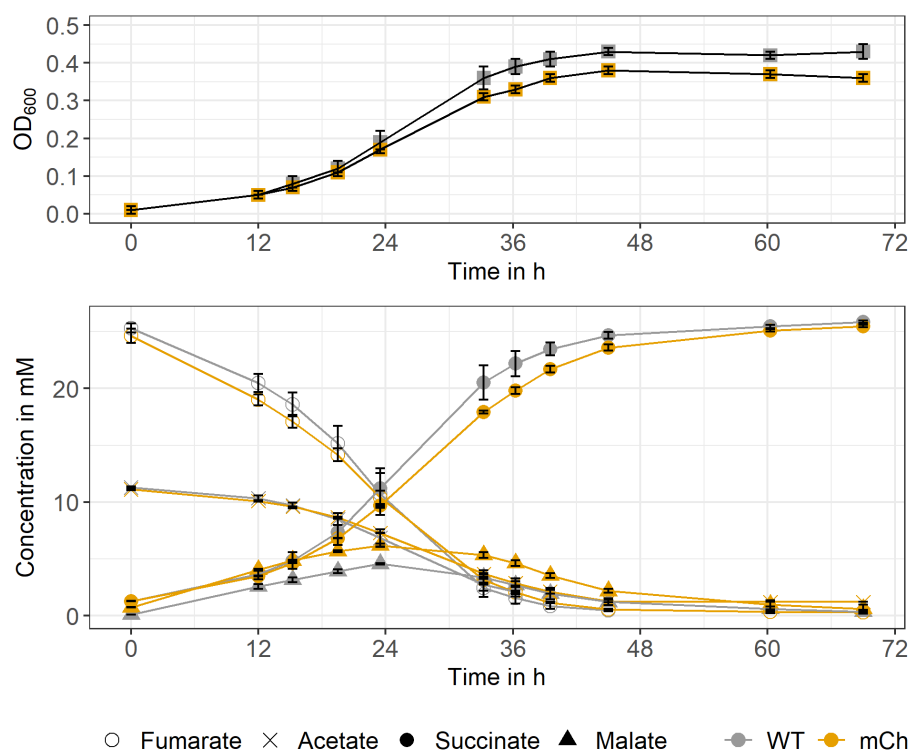


FIGURE A.3: OD₆₀₀ and metabolite concentrations (fumarate, acetate, succinate, malate) were compared between *G. sulfurreducens* WT and *G. sulfurreducens* mCh. Results for WT are shown in grey and mCh in orange. Error bars show SD of the biological triplicates.

A.4 WT current production in the electrochemical flow cell

Initially, no current was produced by *G. sulfurreducens* mCh when the flow cell was in upright position. In order to test whether this was solely a problem of the fluorescent strain or also of the reactor geometry, the WT was applied in the identical flow cell setup. However, current production was marginal still, as seen in Figure A.4.

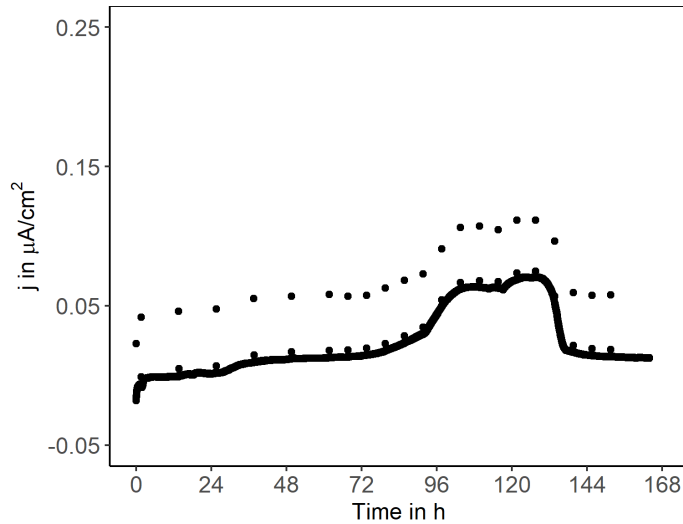


FIGURE A.4: Current density of the WT in the electrochemical flow cell in upright position is shown over time.

The WT produced a maximum of $196 \mu\text{A cm}^{-2}$ in the flow cell, applying the *down-under turn around* procedure. This underlined that the low current density produced in the experiments with *G. sulfurreducens* mCh were caused by the strain and not by the flow cell in general.

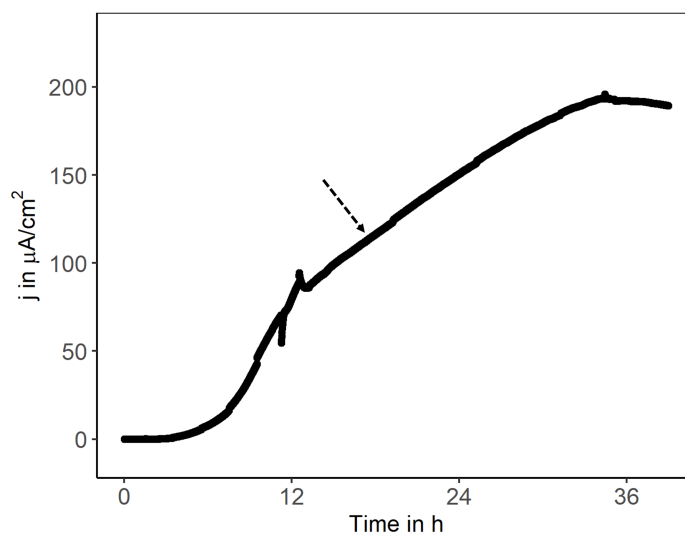


FIGURE A.5: Current density of the WT in the electrochemical flow cell is shown over time. The flow cell was started *down-under* and turned upright after 17h.

Bibliography

- [1] Poul A Østergaard et al. "Sustainable development using renewable energy technology". In: *Renewable Energy* 146 (2020), pp. 2430–2437.
- [2] H Díaz and C Guedes Soares. "Review of the current status, technology and future trends of offshore wind farms". In: *Ocean Engineering* 209 (2020), p. 107381.
- [3] Muhammad Tawalbeh et al. "Environmental impacts of solar photovoltaic systems: A critical review of recent progress and future outlook". In: *Science of The Total Environment* (2020), p. 143528.
- [4] Antonio FO Falcao. "Wave energy utilization: A review of the technologies". In: *Renewable and sustainable energy reviews* 14.3 (2010), pp. 899–918.
- [5] Yuliang Zhang and Gao-Feng Zhao. "A global review of deep geothermal energy exploration: from a view of rock mechanics and engineering". In: *Geomechanics and Geophysics for Geo-Energy and Geo-Resources* 6.1 (2020), pp. 1–26.
- [6] Frank Rosillo-Calle. "A review of biomass energy—shortcomings and concerns". In: *Journal of Chemical Technology & Biotechnology* 91.7 (2016), pp. 1933–1945.
- [7] Ayhan Demirbas. "Waste management, waste resource facilities and waste conversion processes". In: *Energy Conversion and Management* 52.2 (2011), pp. 1280–1287.
- [8] Malek Batayneh, Iqbal Marie, and Ibrahim Asi. "Use of selected waste materials in concrete mixes". In: *Waste management* 27.12 (2007), pp. 1870–1876.
- [9] Sadhan Kumar Ghosh. "Biomass & bio-waste supply chain sustainability for bio-energy and bio-fuel production". In: *Procedia Environmental Sciences* 31 (2016), pp. 31–39.
- [10] Bruce E Logan and Korneel Rabaey. "Conversion of wastes into bioelectricity and chemicals by using microbial electrochemical technologies". In: *Science* 337.6095 (2012), pp. 686–690.
- [11] Bruce E Logan et al. "Microbial fuel cells: methodology and technology". In: *Environmental science & technology* 40.17 (2006), pp. 5181–5192.
- [12] Christopher W Marshall, Edward V LaBelle, and Harold D May. "Production of fuels and chemicals from waste by microbiomes". In: *Current opinion in biotechnology* 24.3 (2013), pp. 391–397.
- [13] Korneel Rabaey, Peter Girguis, and Lars K Nielsen. "Metabolic and practical considerations on microbial electrosynthesis". In: *Current opinion in biotechnology* 22.3 (2011), pp. 371–377.
- [14] Henna M Saeed et al. "Microbial desalination cell technology: a review and a case study". In: *Desalination* 359 (2015), pp. 1–13.

- [15] Loubna Ezziat et al. "Challenges of microbial fuel cell architecture on heavy metal recovery and removal from wastewater". In: *Frontiers in Energy Research* 7 (2019), p. 1.
- [16] Bruce E Logan, Ruggero Rossi, Pascal E Saikaly, et al. "Electroactive microorganisms in bioelectrochemical systems". In: *Nature Reviews Microbiology* 17.5 (2019), pp. 307–319.
- [17] Fanying Kong et al. "Overview of value-added products bioelectrosynthesized from waste materials in microbial electrosynthesis systems". In: *Renewable and Sustainable Energy Reviews* 125 (2020), p. 109816.
- [18] Sungyup Jung et al. "Bioelectrochemical systems for a circular bioeconomy". In: *Bioresource technology* 300 (2020), p. 122748.
- [19] Anthony J Slate et al. "Microbial fuel cells: An overview of current technology". In: *Renewable and sustainable energy reviews* 101 (2019), pp. 60–81.
- [20] Jeffrey J Fornero, Miriam Rosenbaum, and Largus T Angenent. "Electric power generation from municipal, food, and animal wastewaters using microbial fuel cells". In: *Electroanalysis: An International Journal Devoted to Fundamental and Practical Aspects of Electroanalysis* 22.7-8 (2010), pp. 832–843.
- [21] Francesc Hernandez-Sancho, Maria Molinos-Senante, and Ramon Sala-Garrido. "Cost modelling for wastewater treatment processes". In: *Desalination* 268.1-3 (2011), pp. 1–5.
- [22] Kunyu Niu et al. "Construction and operation costs of wastewater treatment and implications for the paper industry in China". In: *Environmental science & technology* 50.22 (2016), pp. 12339–12347.
- [23] Juan R Trapero et al. "Is microbial fuel cell technology ready? An economic answer towards industrial commercialization". In: *Applied energy* 185 (2017), pp. 698–707.
- [24] Dipak A Jadhav et al. "Recent advancement in scaling-up applications of microbial fuel cells: From reality to practicability". In: *Sustainable Energy Technologies and Assessments* (2021), p. 101226.
- [25] Xenia Christodoulou et al. "The use of carbon dioxide in microbial electrosynthesis: advancements, sustainability and economic feasibility". In: *Journal of CO2 Utilization* 18 (2017), pp. 390–399.
- [26] Hanna M Frühauf et al. "Microbial electrosynthesis—an inventory on technology readiness level and performance of different process variants". In: *Biotechnology Journal* 15.10 (2020), p. 2000066.
- [27] Stefano Freguia et al. "Syntrophic processes drive the conversion of glucose in microbial fuel cell anodes". In: *Environmental science & technology* 42.21 (2008), pp. 7937–7943.
- [28] Prashant Pandey et al. "Recent advances in the use of different substrates in microbial fuel cells toward wastewater treatment and simultaneous energy recovery". In: *Applied Energy* 168 (2016), pp. 706–723.
- [29] Hamid Rismani-Yazdi et al. "Cathodic limitations in microbial fuel cells: an overview". In: *Journal of Power Sources* 180.2 (2008), pp. 683–694.
- [30] Feng Zhao et al. "Challenges and constraints of using oxygen cathodes in microbial fuel cells". In: *Environmental science & technology* 40.17 (2006), pp. 5193–5199.

- [31] Anthony Janicek, Yanzen Fan, and Hong Liu. "Design of microbial fuel cells for practical application: a review and analysis of scale-up studies". In: *Biofuels* 5.1 (2014), pp. 79–92.
- [32] Peng Liang et al. "One-year operation of 1000-L modularized microbial fuel cell for municipal wastewater treatment". In: *Water research* 141 (2018), pp. 1–8.
- [33] Xavier Alexis Walter, John Greenman, and Ioannis A Ieropoulos. "Microbial fuel cells directly powering a microcomputer". In: *Journal of power sources* 446 (2020), p. 227328.
- [34] Ioannis Ieropoulos, John Greenman, and Chris Melhuish. "Urine utilisation by microbial fuel cells; energy fuel for the future". In: *Physical Chemistry Chemical Physics* 14.1 (2012), pp. 94–98.
- [35] Christin Koch and Falk Harnisch. "Is there a specific ecological niche for electroactive microorganisms?" In: *ChemElectroChem* 3.9 (2016), pp. 1282–1295.
- [36] Charles R Myers and Kenneth H Nealson. "Bacterial manganese reduction and growth with manganese oxide as the sole electron acceptor". In: *Science* 240.4857 (1988), pp. 1319–1321.
- [37] Frank Caccavo Jr et al. "*Geobacter sulfurreducens* sp. nov., a hydrogen-and acetate-oxidizing dissimilatory metal-reducing microorganism". In: *Applied and environmental microbiology* 60.10 (1994), pp. 3752–3759.
- [38] Hongying Li et al. "Power output of microbial fuel cell emphasizing interaction of anodic binder with bacteria". In: *Journal of Power Sources* 379 (2018), pp. 115–122.
- [39] Uwe Schröder and Falk Harnisch. "Life electric—nature as a blueprint for the development of microbial electrochemical technologies". In: *Joule* 1.2 (2017), pp. 244–252.
- [40] Mackenzie Firer-Sherwood, Gökçe Su Pulcu, and Sean J Elliott. "Electrochemical interrogations of the Mtr cytochromes from *Shewanella*: opening a potential window". In: *JBIC Journal of Biological Inorganic Chemistry* 13.6 (2008), pp. 849–854.
- [41] Mackenzie A Firer-Sherwood et al. "Tools for resolving complexity in the electron transfer networks of multiheme cytochromes c". In: *Metallomics* 3.4 (2011), pp. 344–348.
- [42] Derek R Lovley. "Long-range electron transport to Fe (III) oxide via pili with metallic-like conductivity". In: *Biochemical Society Transactions* 40.6 (2012), pp. 1186–1190.
- [43] Nikhil S Malvankar, Mark T Tuominen, and Derek R Lovley. "Comment on "on electrical conductivity of microbial nanowires and biofilms" by SM Strycharz-Glaven, RM Snider, A. Guiseppi-Elie and LM Tender, energy environ. sci., 2011, 4, 4366". In: *Energy & Environmental Science* 5.3 (2012), pp. 6247–6249.
- [44] Sarah M Strycharz-Glaven and Leonard M Tender. "Reply to the 'Comment on "On electrical conductivity of microbial nanowires and biofilms" by NS Malvankar, MT Tuominen and DR Lovley, Energy Environ. Sci., 2012, 5". In: *Energy & Environmental Science* 5.3 (2012), pp. 6250–6255.
- [45] Sahand Pirbadian and Mohamed Y El-Naggar. "Multistep hopping and extracellular charge transfer in microbial redox chains". In: *Physical Chemistry Chemical Physics* 14.40 (2012), pp. 13802–13808.

- [46] Korneel Rabaey et al. "Microbial phenazine production enhances electron transfer in biofuel cells". In: *Environmental science & technology* 39.9 (2005), pp. 3401–3408.
- [47] Anne Sydow et al. "Electroactive bacteria—molecular mechanisms and genetic tools". In: *Applied microbiology and biotechnology* 98.20 (2014), pp. 8481–8495.
- [48] Ching Leang et al. "Engineering *Geobacter sulfurreducens* to produce a highly cohesive conductive matrix with enhanced capacity for current production". In: *Energy & Environmental Science* 6.6 (2013), pp. 1901–1908.
- [49] Feng Li et al. "Engineering *Shewanella oneidensis* enables xylose-fed microbial fuel cell". In: *Biotechnology for biofuels* 10.1 (2017), pp. 1–10.
- [50] Donggeon Choi et al. "Metabolically engineered glucose-utilizing *Shewanella* strains under anaerobic conditions". In: *Bioresource technology* 154 (2014), pp. 59–66.
- [51] Jeffrey M Flynn et al. "Enabling unbalanced fermentations by using engineered electrode-interfaced bacteria". In: *MBio* 1.5 (2010), e00190–10.
- [52] Daniel R Bond and Derek R Lovley. "Electricity production by *Geobacter sulfurreducens* attached to electrodes". In: *Applied and environmental microbiology* 69.3 (2003), pp. 1548–1555.
- [53] Kelly P Nevin et al. "Power output and columbic efficiencies from biofilms of *Geobacter sulfurreducens* comparable to mixed community microbial fuel cells". In: *Environmental microbiology* 10.10 (2008), pp. 2505–2514.
- [54] Gemma Reguera et al. "Extracellular electron transfer via microbial nanowires". In: *Nature* 435.7045 (2005), pp. 1098–1101.
- [55] Derek R Lovley. "Electrically conductive pili: biological function and potential applications in electronics". In: *Current Opinion in Electrochemistry* 4.1 (2017), pp. 190–198.
- [56] Gemma Reguera et al. "Biofilm and nanowire production leads to increased current in *Geobacter sulfurreducens* fuel cells". In: *Applied and environmental microbiology* 72.11 (2006), pp. 7345–7348.
- [57] Madeline Vargas et al. "Aromatic amino acids required for pili conductivity and long-range extracellular electron transport in *Geobacter sulfurreducens*". In: *MBio* 4.2 (2013), e00105–13.
- [58] Teena Mehta et al. "Outer membrane c-type cytochromes required for Fe (III) and Mn (IV) oxide reduction in *Geobacter sulfurreducens*". In: *Applied and environmental microbiology* 71.12 (2005), pp. 8634–8641.
- [59] Teena Mehta et al. "A putative multicopper protein secreted by an atypical type II secretion system involved in the reduction of insoluble electron acceptors in *Geobacter sulfurreducens*". In: *Microbiology* 152.8 (2006), pp. 2257–2264.
- [60] Kelly P Nevin et al. "Anode biofilm transcriptomics reveals outer surface components essential for high density current production in *Geobacter sulfurreducens* fuel cells". In: *PloS one* 4.5 (2009), e5628.
- [61] Ching Leang, Maddalena V Coppi, and Derek R Lovley. "OmcB, ac-type polyheme cytochrome, involved in Fe (III) reduction in *Geobacter sulfurreducens*". In: *Journal of Bacteriology* 185.7 (2003), pp. 2096–2103.

- [62] Xinlei Qian et al. "Evidence that OmcB and OmpB of *Geobacter sulfurreducens* are outer membrane surface proteins". In: *FEMS Microbiology Letters* 277.1 (2007), pp. 21–27.
- [63] Daniel R Bond et al. "On electron transport through *Geobacter* biofilms". In: *ChemSusChem* 5.6 (2012), p. 1099.
- [64] Ching Leang et al. "Alignment of the c-type cytochrome OmcS along pili of *Geobacter sulfurreducens*". In: *Applied and environmental microbiology* 76.12 (2010), pp. 4080–4084.
- [65] Fengbin Wang et al. "Structure of microbial nanowires reveals stacked hemes that transport electrons over micrometers". In: *Cell* 177.2 (2019), pp. 361–369.
- [66] Sibel Ebru Yalcin et al. "Electric field stimulates production of highly conductive microbial OmcZ nanowires". In: *Nature chemical biology* 16.10 (2020), pp. 1136–1142.
- [67] Xinying Liu et al. "Direct Observation of Electrically Conductive Pili Emanating from *Geobacter sulfurreducens*". In: *Mbio* 12.4 (2021), e02209–21.
- [68] Derek R Lovley et al. "*Geobacter*: the microbe electric's physiology, ecology, and practical applications". In: *Advances in microbial physiology* 59 (2011), pp. 1–100.
- [69] Allison M Speers and Gemma Reguera. "Electron donors supporting growth and electroactivity of *Geobacter sulfurreducens* anode biofilms". In: *Applied and environmental microbiology* 78.2 (2012), pp. 437–444.
- [70] Jeanine S Geelhoed, Anne M Henstra, and Alfons JM Stams. "Carboxydrotrophic growth of *Geobacter sulfurreducens*". In: *Applied microbiology and biotechnology* 100.2 (2016), pp. 997–1007.
- [71] Wen-Chin Lin, Maddalena V Coppi, and Derek R Lovley. "*Geobacter sulfurreducens* can grow with oxygen as a terminal electron acceptor". In: *Applied and environmental microbiology* 70.4 (2004), pp. 2525–2528.
- [72] Christina Elisabeth Anna Engel et al. "Quantification of microaerobic growth of *Geobacter sulfurreducens*". In: *Plos one* 15.1 (2020), e0215341.
- [73] Alexander S Galushko and Bernhard Schink. "Oxidation of acetate through reactions of the citric acid cycle by *Geobacter sulfurreducens* in pure culture and in syntrophic coculture". In: *Archives of microbiology* 174.5 (2000), pp. 314–321.
- [74] Jessica E Butler et al. "Genetic characterization of a single bifunctional enzyme for fumarate reduction and succinate oxidation in *Geobacter sulfurreducens* and engineering of fumarate reduction in *Geobacter metallireducens*". In: *Journal of bacteriology* 188.2 (2006), pp. 450–455.
- [75] Abraham Esteve-Núñez et al. "Growth of *Geobacter sulfurreducens* under nutrient-limiting conditions in continuous culture". In: *Environmental microbiology* 7.5 (2005), pp. 641–648.
- [76] Lydie Ploux, Arnaud Ponche, and Karine Anselme. "Bacteria/material interfaces: role of the material and cell wall properties". In: *Journal of Adhesion Science and Technology* 24.13-14 (2010), pp. 2165–2201.
- [77] J William Costerton et al. "Microbial biofilms". In: *Annual review of microbiology* 49.1 (1995), pp. 711–745.
- [78] Claiborne Fuqua, Stephen C Winans, and Peter Greenberg. "Quorum sensing in bacteria: the LuxR-LuxI family of cell density-responsive transcriptional regulators". In: *Journal of bacteriology* 176.2 (1994), pp. 269–275.

- [79] Gregory G Anderson and George A O'toole. "Innate and induced resistance mechanisms of bacterial biofilms". In: *Bacterial biofilms* (2008), pp. 85–105.
- [80] Jean G Detry et al. "Laminar flow in radial flow cell with small aspect ratios: numerical and experimental study". In: *Chemical Engineering Science* 64.1 (2009), pp. 31–42.
- [81] Hannah H Tuson and Douglas B Weibel. "Bacteria–surface interactions". In: *Soft matter* 9.17 (2013), pp. 4368–4380.
- [82] George A O'Toole and Gerard CL Wong. "Sensational biofilms: surface sensing in bacteria". In: *Current opinion in microbiology* 30 (2016), pp. 139–146.
- [83] Hongyue Dang and Charles R Lovell. "Microbial surface colonization and biofilm development in marine environments". In: *Microbiology and molecular biology reviews* 80.1 (2016), pp. 91–138.
- [84] Vera Carniello et al. "Physico-chemistry from initial bacterial adhesion to surface-programmed biofilm growth". In: *Advances in colloid and interface science* 261 (2018), pp. 1–14.
- [85] Jacob N Israelachvili. *Intermolecular and surface forces*. Academic press, 1991.
- [86] Carel Jan van Oss. "Development and applications of the interfacial tension between water and organic or biological surfaces". In: *Colloids and surfaces B: Biointerfaces* 54.1 (2007), pp. 2–9.
- [87] Christian Spengler et al. "Modeling Bacterial Adhesion to Unconditioned Abiotic Surfaces". In: *Frontiers in Mechanical Engineering* 7 (2021), p. 23.
- [88] Hans-Curt Flemming and Jost Wingender. "The biofilm matrix". In: *Nature reviews microbiology* 8.9 (2010), pp. 623–633.
- [89] Ece Karatan and Paula Watnick. "Signals, regulatory networks, and materials that build and break bacterial biofilms". In: *Microbiology and molecular biology reviews* 73.2 (2009), pp. 310–347.
- [90] Claire Prigent-Combaret et al. "Abiotic surface sensing and biofilm-dependent regulation of gene expression in *Escherichia coli*". In: *Journal of bacteriology* 181.19 (1999), pp. 5993–6002.
- [91] Stefan Wuertz, Satoshi Okabe, and Martina Hausner. "Microbial communities and their interactions in biofilm systems: an overview". In: *Water Science and Technology* 49.11-12 (2004), pp. 327–336.
- [92] Kun Guo et al. "Engineering electrodes for microbial electrocatalysis". In: *Current opinion in biotechnology* 33 (2015), pp. 149–156.
- [93] Minghua Zhou et al. "An overview of electrode materials in microbial fuel cells". In: *Journal of Power Sources* 196.10 (2011), pp. 4427–4435.
- [94] André Baudler et al. "Does it have to be carbon? Metal anodes in microbial fuel cells and related bioelectrochemical systems". In: *Energy & Environmental Science* 8.7 (2015), pp. 2048–2055.
- [95] Akiyoshi Kuzume et al. "An in-situ surface electrochemistry approach toward whole-cell studies: Charge transfer between *Geobacter sulfurreducens* and electrified metal/electrolyte interfaces through linker molecules". In: *Electrochimica acta* 112 (2013), pp. 933–942.
- [96] Diana Pocaznoi et al. "Ultra microelectrodes increase the current density provided by electroactive biofilms by improving their electron transport ability". In: *Energy & Environmental Science* 5.1 (2012), pp. 5287–5296.

- [97] Takahiro Yamashita and Hiroshi Yokoyama. "Molybdenum anode: a novel electrode for enhanced power generation in microbial fuel cells, identified via extensive screening of metal electrodes". In: *Biotechnology for biofuels* 11.1 (2018), pp. 1–13.
- [98] Carlo Santoro et al. "Microbial fuel cells: From fundamentals to applications. A review". In: *Journal of power sources* 356 (2017), pp. 225–244.
- [99] Elena Kipf et al. "Systematic investigation of anode materials for microbial fuel cells with the model organism *G. sulfurreducens*". In: *Bioresource Technology Reports* 2 (2018), pp. 29–37.
- [100] Luciana Robuschi, J Pablo Tomba, and Juan Pablo Busalmen. "Proving *Geobacter* biofilm connectivity with confocal Raman microscopy". In: *Journal of Electroanalytical Chemistry* 793 (2017), pp. 99–103.
- [101] Francesco Scarabotti et al. "The electrode potential determines the yield coefficients of early-stage *Geobacter sulfurreducens* biofilm anodes". In: *Bioelectrochemistry* 140 (2021), p. 107752.
- [102] Jieun Song et al. "Comprehensive metabolomic analyses of anode-respiring *Geobacter sulfurreducens* cells: The impact of anode-respiration activity on intracellular metabolite levels". In: *Process Biochemistry* 51.1 (2016), pp. 34–38.
- [103] Daqian Jiang and Baikun Li. "Granular activated carbon single-chamber microbial fuel cells (GAC-SCMFCs): a design suitable for large-scale wastewater treatment processes". In: *Biochemical Engineering Journal* 47.1-3 (2009), pp. 31–37.
- [104] Pei-Fang Tee et al. "Performance evaluation of a hybrid system for efficient palm oil mill effluent treatment via an air-cathode, tubular upflow microbial fuel cell coupled with a granular activated carbon adsorption". In: *Bioresource technology* 216 (2016), pp. 478–485.
- [105] Jia Liu et al. "Intermittent contact of fluidized anode particles containing exoelectrogenic biofilms for continuous power generation in microbial fuel cells". In: *Journal of Power Sources* 261 (2014), pp. 278–284.
- [106] Lei Zhao et al. "Computational investigation of the flow field contribution to improve electricity generation in granular activated carbon-assisted microbial fuel cells". In: *Journal of Power Sources* 333 (2016), pp. 83–87.
- [107] Markus Stöckl. *Attachment Under Current - Biofilm Formation by Electroactive Bacteria*. Shaker, 2018.
- [108] Markus Stöckl, Jens Schrader, and Klaus-Michael Mangold. "Verfahren zur mikrobiologisch-elektrochemischen Synthese von chemischen Stoffen durch elektroaktive Mikroorganismen". DE Patent DE102014112685A. 2016.
- [109] Kaixuan Zhang et al. "Macroporous carbon foam with high conductivity as an efficient anode for microbial fuel cells". In: *International Journal of Hydrogen Energy* 45.21 (2020), pp. 12121–12129.
- [110] Priyakant Pushkar and Arvind Kumar Mungray. "Exploring the use of 3 dimensional low-cost sugar-urea carbon foam electrode in the benthic microbial fuel cell". In: *Renewable Energy* 147 (2020), pp. 2032–2042.
- [111] Yixuan Wang et al. "High power generation in mixed-culture microbial fuel cells with corncob-derived three-dimensional N-doped bioanodes and the impact of N dopant states". In: *Chemical Engineering Journal* 399 (2020), p. 125848.

- [112] André Baudler, Sebastian Riedl, and Uwe Schröder. "Long-term performance of primary and secondary electroactive biofilms using layered corrugated carbon electrodes". In: *Frontiers in Energy Research* 2 (2014), p. 30.
- [113] Huazhang Zhao et al. "Electrochemical reduction of carbon dioxide in an MFC-MEC system with a layer-by-layer self-assembly carbon nanotube/cobalt phthalocyanine modified electrode". In: *Environmental science & technology* 46.9 (2012), pp. 5198–5204.
- [114] Suna Timur et al. "Development of a microbial biosensor based on carbon nanotube (CNT) modified electrodes". In: *Electrochemistry Communications* 9.7 (2007), pp. 1810–1815.
- [115] In Ho Park et al. "Enhanced electrical contact of microbes using Fe₃O₄/CNT nanocomposite anode in mediator-less microbial fuel cell". In: *Biosensors and Bioelectronics* 58 (2014), pp. 75–80.
- [116] Ziming He et al. "Architecture engineering of hierarchically porous chitosan/vacuum-stripped graphene scaffold as bioanode for high performance microbial fuel cell". In: *Nano letters* 12.9 (2012), pp. 4738–4741.
- [117] Peng Zhang et al. "Nanomaterials for facilitating microbial extracellular electron transfer: Recent progress and challenges". In: *Bioelectrochemistry* 123 (2018), pp. 190–200.
- [118] Asim A Yaqoob, Mohamad NM Ibrahim, and Susana Rodríguez-Couto. "Development and modification of materials to build cost-effective anodes for microbial fuel cells (MFCs): An overview". In: *Biochemical Engineering Journal* (2020), p. 107779.
- [119] Carlo Santoro et al. "Influence of anode surface chemistry on microbial fuel cell operation". In: *Bioelectrochemistry* 106 (2015), pp. 141–149.
- [120] Matthieu Picot et al. "Graphite anode surface modification with controlled reduction of specific aryl diazonium salts for improved microbial fuel cells power output". In: *Biosensors and Bioelectronics* 28.1 (2011), pp. 181–188.
- [121] Baitao Li et al. "Surface modification of microbial fuel cells anodes: approaches to practical design". In: *Electrochimica Acta* 134 (2014), pp. 116–126.
- [122] Minghua Zhou et al. "Anode modification by electrochemical oxidation: A new practical method to improve the performance of microbial fuel cells". In: *Biochemical Engineering Journal* 60 (2012), pp. 151–155.
- [123] Kun Guo et al. "Effects of surface charge and hydrophobicity on anodic biofilm formation, community composition, and current generation in bioelectrochemical systems". In: *Environmental science & technology* 47.13 (2013), pp. 7563–7570.
- [124] Peng Wang, Haoran Li, and Zhuwei Du. "Polyaniline synthesis by cyclic voltammetry for anodic modification in microbial fuel cells". In: *International Journal of Electrochemical Science* 9 (2014), pp. 2038–2046.
- [125] G Gnana Kumar et al. "Synthesis, structural, and morphological characterizations of reduced graphene oxide-supported polypyrrole anode catalysts for improved microbial fuel cell performances". In: *ACS Sustainable Chemistry & Engineering* 2.10 (2014), pp. 2283–2290.
- [126] Sung-Hee Roh and Hee-Gweon Woo. "Carbon nanotube composite electrode coated with polypyrrole for microbial fuel cell application". In: *Journal of nanoscience and nanotechnology* 15.1 (2015), pp. 484–487.

- [127] Yee Li Kang, Shaliza Ibrahim, and Saravanan Pichiah. "Synergetic effect of conductive polymer poly (3, 4-ethylenedioxythiophene) with different structural configuration of anode for microbial fuel cell application". In: *Bioresource technology* 189 (2015), pp. 364–369.
- [128] Daniel A Lowy et al. "Harvesting energy from the marine sediment–water interface II: kinetic activity of anode materials". In: *Biosensors and Bioelectronics* 21.11 (2006), pp. 2058–2063.
- [129] Gero Decher. "Fuzzy nanoassemblies: toward layered polymeric multicomposites". In: *Science* 277.5330 (1997), pp. 1232–1237.
- [130] Joseph J Richardson et al. "Innovation in layer-by-layer assembly". In: *Chemical Reviews* 116.23 (2016), pp. 14828–14867.
- [131] Shanshan Guo, Xiaoying Zhu, and Xian Jun Loh. "Controlling cell adhesion using layer-by-layer approaches for biomedical applications". In: *Materials Science and Engineering: C* 70 (2017), pp. 1163–1175.
- [132] Fangchao Song, Hyun Koo, and Dacheng Ren. "Effects of material properties on bacterial adhesion and biofilm formation". In: *Journal of dental research* 94.8 (2015), pp. 1027–1034.
- [133] Rana M Jisr, Hassan H Rmaile, and Joseph B Schlenoff. "Hydrophobic and ultrahydrophobic multilayer thin films from perfluorinated polyelectrolytes". In: *Angewandte Chemie International Edition* 44.5 (2005), pp. 782–785.
- [134] Hyejoong Jeong et al. "Intrinsic hydrophobic cairnlike multilayer films for antibacterial effect with enhanced durability". In: *ACS applied materials & interfaces* 7.47 (2015), pp. 26117–26123.
- [135] F Boulmedais et al. "Polyelectrolyte multilayer films with pegylated polypeptides as a new type of anti-microbial protection for biomaterials". In: *Biomaterials* 25.11 (2004), pp. 2003–2011.
- [136] Wei-Bor Tsai, Ying-Hao Chen, and Hsiu-Wen Chien. "Collaborative cell-resistant properties of polyelectrolyte multilayer films and surface PEGylation on reducing cell adhesion to cytophilic surfaces". In: *Journal of Biomaterials Science, Polymer Edition* 20.11 (2009), pp. 1611–1628.
- [137] Michael T Thompson et al. "Tuning compliance of nanoscale polyelectrolyte multilayers to modulate cell adhesion". In: *Biomaterials* 26.34 (2005), pp. 6836–6845.
- [138] Patrick Bertrand et al. "Ultrathin polymer coatings by complexation of polyelectrolytes at interfaces: suitable materials, structure and properties". In: *Macromolecular rapid communications* 21.7 (2000), pp. 319–348.
- [139] Gero Decher and J Schmitt. "Fine-tuning of the film thickness of ultrathin multilayer films composed of consecutively alternating layers of anionic and cationic polyelectrolytes". In: *Trends in Colloid and Interface Science VI* (1992), pp. 160–164.
- [140] Yuri Lvov, Gero Decher, and Helmuth Moehwald. "Assembly, structural characterization, and thermal behavior of layer-by-layer deposited ultrathin films of poly (vinyl sulfate) and poly (allylamine)". In: *Langmuir* 9.2 (1993), pp. 481–486.
- [141] Richard A McAloney et al. "Atomic force microscopy studies of salt effects on polyelectrolyte multilayer film morphology". In: *Langmuir* 17.21 (2001), pp. 6655–6663.

- [142] Joana Azeredo et al. "Critical review on biofilm methods". In: *Critical reviews in microbiology* 43.3 (2017), pp. 313–351.
- [143] Stephen W Paddock. "Confocal laser scanning microscopy". In: *Biotechniques* 27.5 (1999), pp. 992–1004.
- [144] Nuno F Azevedo, MJ Vieira, and William Keevil. "Establishment of a continuous model system to study *Helicobacter pylori* survival in potable water biofilms". In: *Water Science and Technology* 47.5 (2003), pp. 155–160.
- [145] Thomas R Neu and John R Lawrence. "Advanced techniques for in situ analysis of the biofilm matrix (structure, composition, dynamics) by means of laser scanning microscopy". In: *Microbial Biofilms*. Springer, 2014, pp. 43–64.
- [146] CK Hope, D Clements, and M Wilson. "Determining the spatial distribution of viable and nonviable bacteria in hydrated microcosm dental plaques by viability profiling". In: *Journal of applied microbiology* 93.3 (2002), pp. 448–455.
- [147] Pilar Sanchez-Vizueté et al. "Identification of ypqP as a new *Bacillus subtilis* biofilm determinant that mediates the protection of *Staphylococcus aureus* against antimicrobial agents in mixed-species communities". In: *Applied and environmental microbiology* 81.1 (2015), pp. 109–118.
- [148] Ashley E Franks et al. "Microtoming coupled to microarray analysis to evaluate the spatial metabolic status of *Geobacter sulfurreducens* biofilms". In: *The ISME journal* 4.4 (2010), pp. 509–519.
- [149] Markus Stöckl et al. "Membrane separated flow cell for parallelized electrochemical impedance spectroscopy and confocal laser scanning microscopy to characterize electro-active microorganisms". In: *Electrochimica Acta* 220 (2016), pp. 444–452.
- [150] Ramaraja P Ramasamy et al. "Impact of initial biofilm growth on the anode impedance of microbial fuel cells". In: *Biotechnology and bioengineering* 101.1 (2008), pp. 101–108.
- [151] Dietmar Ende and Klaus-Michael Mangold. "Impedanzspektroskopie". In: *Chemie in unserer Zeit* 27.3 (1993), pp. 134–140.
- [152] Christopher J Marx and Mary E Lidstrom. "Development of improved versatile broad-host-range vectors for use in methylotrophs and other Gram-negative bacteria". In: *Microbiology* 147.8 (2001), pp. 2065–2075.
- [153] Byoung-Chan Kim et al. "OmcF, a putative c-type monoheme outer membrane cytochrome required for the expression of other outer membrane cytochromes in *Geobacter sulfurreducens*". In: *Journal of Bacteriology* 187.13 (2005), pp. 4505–4513.
- [154] Ashley E Franks et al. "Novel strategy for three-dimensional real-time imaging of microbial fuel cell communities: monitoring the inhibitory effects of proton accumulation within the anode biofilm". In: *Energy & Environmental Science* 2.1 (2009), pp. 113–119.
- [155] Kathleen Sprouffske. *growthcurver: Simple Metrics to Summarize Growth Curves*. R package version 0.3.1. 2020. URL: <https://CRAN.R-project.org/package=growthcurver>.
- [156] Markus Stöckl et al. "Extracellular polymeric substances from *Geobacter sulfurreducens* biofilms in microbial fuel cells". In: *ACS applied materials & interfaces* 11.9 (2019), pp. 8961–8968.

- [157] Peter Clauwaert et al. "Minimizing losses in bio-electrochemical systems: the road to applications". In: *Applied microbiology and biotechnology* 79.6 (2008), pp. 901–913.
- [158] Franziska Enzmann et al. "Transferring bioelectrochemical processes from H-cells to a scalable bubble column reactor". In: *Chemical Engineering Science* 193 (2019), pp. 133–143.
- [159] R Core Team. *R: A Language and Environment for Statistical Computing*. R Foundation for Statistical Computing, Vienna, Austria, 2018. URL: <https://www.R-project.org/>.
- [160] Hanna M Frühauf, Markus Stöckl, and Dirk Holtmann. "R-based method for quantitative analysis of biofilm thickness by using confocal laser scanning microscopy". In: *Engineering in Life Sciences* 22 (2022), pp. 464–470.
- [161] Jeffrey D. Clogston and Anil K. Patri. "Zeta Potential Measurement". In: *Characterization of Nanoparticles Intended for Drug Delivery*. Ed. by Scott E. McNeil. Oxford: Humana Press, 2011. Chap. 6, pp. 63–70.
- [162] Martin Stratmann and Heinz Streckel. "On the atmospheric corrosion of metals which are covered with thin electrolyte layers—I. Verification of the experimental technique". In: *Corrosion Science* 30.6-7 (1990), pp. 681–696.
- [163] Martin Stratmann and Heinz Streckel. "On the atmospheric corrosion of metals which are covered with thin electrolyte layers—II. Experimental results". In: *Corrosion Science* 30.6-7 (1990), pp. 697–714.
- [164] K Wapner et al. "Height-regulating scanning Kelvin probe for simultaneous measurement of surface topology and electrode potentials at buried polymer/metal interfaces". In: *Journal of the Electrochemical Society* 152.3 (2005), E114.
- [165] Zhen He and Florian Mansfeld. "Exploring the use of electrochemical impedance spectroscopy (EIS) in microbial fuel cell studies". In: *Energy & Environmental Science* 2.2 (2009), pp. 215–219.
- [166] Ramaraja P Ramasamy et al. "Impact of initial biofilm growth on the anode impedance of microbial fuel cells". In: *Biotechnology and bioengineering* 101.1 (2008), pp. 101–108.
- [167] RStudio Team. *RStudio: Integrated Development Environment for R*. RStudio, PBC, Boston, MA, 2021. URL: <http://www.rstudio.com/>.
- [168] Hadley Wickham. *Ggplot2: Elegant graphics for data analysis*. en. 2nd ed. Use R! Cham, Switzerland: Springer International Publishing, June 2016. ISBN: 9783319242774.
- [169] Minguang Dai. "The effect of zeta potential of activated carbon on the adsorption of dyes from aqueous solution: I. The adsorption of cationic dyes: methyl green and methyl violet". In: *Journal of Colloid and Interface Science* 164.1 (1994), pp. 223–228.
- [170] Haeshin Lee et al. "Substrate-independent layer-by-layer assembly by using mussel-adhesive-inspired polymers". In: *Advanced materials* 20.9 (2008), pp. 1619–1623.
- [171] Thi Thi Nge et al. "Synthesis and characterization of chitosan/poly (acrylic acid) polyelectrolyte complex". In: *Journal of applied polymer science* 83.5 (2002), pp. 1025–1035.

- [172] Quankui Lin et al. "Hydrated polysaccharide multilayer as an intraocular lens surface coating for biocompatibility improvements". In: *Journal of Materials Chemistry B* 3.18 (2015), pp. 3695–3703.
- [173] Sara Ferraris et al. "Zeta potential measurements on solid surfaces for in vitro biomaterials testing: surface charge, reactivity upon contact with fluids and protein adsorption". In: *Frontiers in bioengineering and biotechnology* 6 (2018), p. 60.
- [174] Bassim H Hameed, Abdulbari A Ahmad, and Norashid Aziz. "Isotherms, kinetics and thermodynamics of acid dye adsorption on activated palm ash". In: *Chemical Engineering Journal* 133.1-3 (2007), pp. 195–203.
- [175] P Vinke et al. "Modification of the surfaces of a gasactivated carbon and a chemically activated carbon with nitric acid, hypochlorite, and ammonia". In: *Carbon* 32.4 (1994), pp. 675–686.
- [176] Mohammad S Shafeeyan et al. "Ammonia modification of activated carbon to enhance carbon dioxide adsorption: effect of pre-oxidation". In: *Applied Surface Science* 257.9 (2011), pp. 3936–3942.
- [177] Florian Mayer et al. "Adsorption of *Shewanella oneidensis* MR-1 to the electrode material activated carbon fabric". In: *Journal of Chemical Technology & Biotechnology* 93.10 (2018), pp. 3000–3010.
- [178] Jose Rivera-Utrilla et al. "Bioadsorption of Pb (II), Cd (II), and Cr (VI) on activated carbon from aqueous solutions". In: *Carbon* 41.2 (2003), pp. 323–330.
- [179] Jose Rivera-Utrilla et al. "Activated carbon surface modifications by adsorption of bacteria and their effect on aqueous lead adsorption". In: *Journal of Chemical Technology & Biotechnology* 76.12 (2001), pp. 1209–1215.
- [180] Silvana Velten et al. "Rapid and direct estimation of active biomass on granular activated carbon through adenosine tri-phosphate (ATP) determination". In: *Water Research* 41.9 (2007), pp. 1973–1983.
- [181] Myles Hollander and Douglas A Wolfe. "Nonparametric statistical methods". In: *Wiley; New York* (1973).
- [182] William H Press et al. "Numerical recipes in C". In: (1988).
- [183] Benjamin Korth et al. "Determining incremental coulombic efficiency and physiological parameters of early stage *Geobacter* spp. enrichment biofilms". In: *PloS one* 15.6 (2020), e0234077.
- [184] Dong-Feng Liu and Wen-Wei Li. "Potential-dependent extracellular electron transfer pathways of exoelectrogens". In: *Current Opinion in Chemical Biology* 59 (2020), pp. 140–146.
- [185] Lori Zacharoff, Chi Ho Chan, and Daniel R Bond. "Reduction of low potential electron acceptors requires the CbcL inner membrane cytochrome of *Geobacter sulfurreducens*". In: *Bioelectrochemistry* 107 (2016), pp. 7–13.
- [186] Xiaojia He et al. "Spatially Resolved Electron Transport through Anode-Respiring *Geobacter sulfurreducens* Biofilms: Controls and Constraints". In: *ChemElectroChem* (2021).
- [187] Dao-Bo Li et al. "Potential regulates metabolism and extracellular respiration of electroactive *Geobacter* biofilm". In: *Biotechnology and bioengineering* 116.5 (2019), pp. 961–971.

- [188] Shoichi Matsuda et al. "Negative faradaic resistance in extracellular electron transfer by anode-respiring *Geobacter sulfurreducens* cells". In: *Environmental science & technology* 45.23 (2011), pp. 10163–10169.
- [189] Guiqin Yang et al. "Anode potentials regulate *Geobacter* biofilms: new insights from the composition and spatial structure of extracellular polymeric substances". In: *Water research* 159 (2019), pp. 294–301.
- [190] Nurit Beyth et al. "Antibacterial activity of dental composites containing quaternary ammonium polyethylenimine nanoparticles against *Streptococcus mutans*". In: *Biomaterials* 27.21 (2006), pp. 3995–4002.
- [191] Juan-Juan Sun et al. "A novel layer-by-layer self-assembled carbon nanotube-based anode: Preparation, characterization, and application in microbial fuel cell". In: *Electrochimica Acta* 55.9 (2010), pp. 3041–3047.
- [192] Xian-Wei Liu et al. "Conductive carbon nanotube hydrogel as a bioanode for enhanced microbial electrocatalysis". In: *ACS applied materials & interfaces* 6.11 (2014), pp. 8158–8164.
- [193] Jia Ma and Yogeshwar Sahai. "Chitosan biopolymer for fuel cell applications". In: *Carbohydrate Polymers* 92.2 (2013), pp. 955–975.
- [194] Yingdan Zhang et al. "Cell growth and protein expression of *Shewanella oneidensis* in biofilms and hydrogel-entrapped cultures". In: *Molecular BioSystems* 10.5 (2014), pp. 1035–1042.
- [195] Liad Badihi Hauslich et al. "The adhesion of oral bacteria to modified titanium surfaces: role of plasma proteins and electrostatic forces". In: *Clinical oral implants research* 24 (2013), pp. 49–56.
- [196] Hanna M Frühauf, Markus Stöckl, and Dirk Holtmann. "Influence of electrode surface charge on current production by *Geobacter sulfurreducens* microbial anodes". In: *Bioelectrochemistry* 147 (2022), p. 108213.
- [197] F Sundfors et al. "Kinetics of electron transfer between Fe(CN)₆^{3-/4-} and poly(3, 4-ethylenedioxythiophene) studied by electrochemical impedance spectroscopy". In: *Electrochimica acta* 47.13-14 (2002), pp. 2245–2251.
- [198] Larry A Gross et al. "The structure of the chromophore within DsRed, a red fluorescent protein from coral". In: *Proceedings of the National Academy of Sciences* 97.22 (2000), pp. 11990–11995.
- [199] Piyush Parkhey and Reecha Sahu. "Microfluidic microbial fuel cells: Recent advancements and future prospects". In: *International Journal of Hydrogen Energy* 46.4 (2021), pp. 3105–3123.
- [200] Ashley E Franks, Richard H Glaven, and Derek R Lovley. "Real-Time Spatial Gene Expression Analysis within Current-Producing Biofilms". In: *ChemSusChem* 5.6 (2012), pp. 1092–1098.
- [201] Roger Heim, Douglas C Prasher, and Roger Y Tsien. "Wavelength mutations and posttranslational autoxidation of green fluorescent protein". In: *Proceedings of the National Academy of Sciences* 91.26 (1994), pp. 12501–12504.
- [202] Harun F Ozbakir et al. "Beyond the green fluorescent protein: biomolecular reporters for anaerobic and deep-tissue imaging". In: *Bioconjugate chemistry* 31.2 (2019), pp. 293–302.
- [203] Dingding Ye et al. "In situ visualization of biofilm formation in a microchannel for a microfluidic microbial fuel cell anode". In: *International Journal of Hydrogen Energy* 46.27 (2021), pp. 14651–14658.

-
- [204] Hanna Marianne Frühauf-Wyllie and Dirk Holtmann. "Geobacter sulfurreducens metabolism at different donor/acceptor ratios". In: *MicrobiologyOpen* 11 (2022), e1322.
- [205] Raimo Hartmann et al. "Quantitative image analysis of microbial communities with BiofilmQ". In: *Nature microbiology* 6.2 (2021), pp. 151–156.
- [206] Phillipp Sievers et al. "Use of torsional resonators to monitor electroactive biofilms". In: *Biosensors and Bioelectronics* 110 (2018), pp. 225–232.
- [207] Christian Spengler et al. "Modeling Bacterial Adhesion to Unconditioned Abiotic Surfaces". In: *Frontiers in Mechanical Engineering* 7 (2021), p. 23.